High-fidelity Stability Analysis for Parafoil Descent on Titan

Sowndariya Dhiyaneeswaran

Faculty of Aerospace Engineering

TU Delft

HIGH-FIDELITY STABILITY ANALYSIS FOR PARAFOIL DESCENT ON TITAN

by

SOWNDARIYA DHIYANEESWARAN

in fulfilment of the requirements for the degree of,
Master of Science
in Aerospace Engineering at the Delft University of Technology.

Student Number:	4816277
Supervisor:	Dr. ir. E. Mooij
Committee members:	ir. M. Naeije
	ir. W. Simons

An electronic version of this dissertation is available at
http://repository.tudelft.nl/.

The cover image was designed and created by the author using Microsoft PowerPoint and Photoshop tools.

Contents

Nomenclature

List of Symbols

Roman

a	Speed of sound [m/s]
A	Added mass coefficient [kg/m]
B	Added mass coefficient [kg/m]
b	Span of the parafoil [m]
C_L	Lift coefficient [–]
C_D	Drag coefficient [–]
C_{D0}	Zero-lift drag coefficient [–]
C_m	Pitching moment coefficient [–]
C_n	Yawing moment coefficient [–]
C_Y	Side force coefficient [–]
c	Parafoil chord length [m]
D	Drag force [N]
F_x, F_y, F_z	Translational forces in the body frame [N]
$\boldsymbol{g}$	Gravitational acceleration [m/s^2]
h	Altitude [m]
I_x, I_y, I_z	Moments of inertia about principal axes [kg·m^2]
$\boldsymbol{I_p}, \boldsymbol{I_r}$	Inertia matrices for the parafoil and capsule [kg·m^2]
L	Lift force [N]
$\boldsymbol{L_p}, \boldsymbol{L_r}$	Position vector components for parafoil and capsule [m]
$\boldsymbol{M_x}, \boldsymbol{M_y}, \boldsymbol{M_z}$	Aerodynamic moments about principal axes [N·m]
$\boldsymbol{M_p}, \boldsymbol{M_r}$	Mass matrices for parafoil and payload [kg]
m	Total mass [kg]
m_c	Mass of the canopy [kg]
m_l	Mass of suspension lines [kg]
$m_{payload}$	Mass of payload/capsule [kg]
p, q, r	Rotational rates around the body axes [rad/s]
$\boldsymbol{R_p}, \boldsymbol{R_r}$	Distance from hinge to parafoil and capsule [m]
S	Parafoil reference area [m^2]
S_{ref_p}	Parachute reference area [m^2]
S_{ref_r}	Capsule reference area [m^2]
t	Time [s]
V	Speed [m/s]
v_x, v_y, v_z	Velocity components in the body frame [m/s]
$\boldsymbol{V_p}, \boldsymbol{V_r}$	Airspeed of parafoil and capsule [m/s]
x_p, y_p, z_p	Position components of parafoil in body frame [m]
x_r, y_r, z_r	Position components of capsule in body frame [m]

Greek

α	Angle of attack [rad]
β	Sideslip angle [rad]
δ	Planetocentric latitude [rad]
ϵ	Anhedral angle [rad]
γ	Flight path angle [rad]

μ	Rigging angle [rad]
ϕ	Roll angle [rad]
θ	Pitch angle [rad]
ψ	Yaw angle [rad]
ρ	Air density [kg/m^3]
$\omega_x, \omega_y, \omega_z$	Angular velocities about body axes [rad/s]
ω_n	Natural frequency [rad/s]
ζ	Damping ratio [–]

Vectors and Matrices

$\mathbf{r}_{p,B}$	Position vector of parafoil relative to hinge in body frame [m]
$\mathbf{r}_{r,B}$	Position vector of capsule relative to hinge in body frame [m]
$\mathbf{S}_{r_p}, \mathbf{S}_{r_r}$	Skew-symmetric matrices for parafoil and capsule positions [–]
Ω_p, Ω_r	Skew-symmetric matrices for parafoil and capsule angular rates [–]
$\mathbf{M}_H$	Hinge moment matrix [N·m]
$\mathbf{F}_{\mathbf{total}}$	Total force vector [N]
$\mathbf{M}_{\mathbf{total}}$	Total moment vector [N·m]

List of Abbreviations

6DOF	Six Degrees of Freedom
9DOF	Nine Degrees of Freedom
AOA	Angle Of Attack
ANOVA	Analysis Of Variance
CFD	Computational Fluid Dynamics
COM	Centre Of Mass
GCM	General Circulation Model
GNC	Guidance, Navigation, and Control
TRN	Terrain Relative Navigation
EDL	Entry, Descent, and Landing

ABSTRACT

This study investigates the complex dynamics of parafoil systems for Titan's challenging atmospheric conditions. A dual-framework approach was employed, where the 6-degree-of-freedom (6DOF) parafoil-capsule model served as an essential foundation for verification, enabling the subsequent development and testing of the 9-degree-of-freedom (9DOF) model. While the 6DOF model simplifies the system as a single rigid body, the 9DOF model provides insights into the flexible rotational coupling effects to capture the dynamic interactions between the two separate rigid bodies; the parafoil and capsule, connected by a hinge with a spring-damper system.

The research encompasses extensive model verification through energy conservation, angular momentum tests, and sensitivity analyses, ensuring robust fidelity across both linearised and nonlinear numerical simulations. A novel quasi-linearised eigenvalue analysis highlights the rotational stability characteristics of the system, including natural frequencies and damping ratios, while demonstrating the limitations of linearisation for capturing non-linear dynamic coupling effects.

Sensitivity analyses reveal critical dependencies on aerodynamic parameters alongside structural and mass properties. Wind studies examine the combined longitudinal and lateral stability under steady and gust wind scenarios across multiple angles and altitudes, simulating Titan's zonal wind patterns. Distinct differences between the 6DOF and 9DOF models highlight the impact of flexible coupling, with the parafoil demonstrating moderated oscillations and the capsule exhibiting amplified responses due to dynamic interactions. These insights underscore the importance of modelling both components independently for high-fidelity stability analysis.

Parafoil systems exhibit potential for improved stability and precision, reducing reliance on fuel-intensive propulsion-based corrections for future planetary descent missions. This work establishes a comprehensive framework for parafoil modelling, combining high-fidelity dynamics, linear and non-linear stability analyses, and environmental adaptability. By systematically comparing 6DOF and 9DOF approaches, the study highlights the importance of flexible coupling dynamics and detailed environmental modelling in designing robust guidance and control systems for planetary exploration.

ACKNOWLEDGEMENTS

I would like to express my deepest gratitude to my thesis supervisor, Dr. ir. Erwin Mooij, for his invaluable guidance and unwavering support throughout the course of this thesis. His expertise, patience, and encouragement have been instrumental in shaping my understanding and helping me overcome the many challenges I faced during this journey. The lessons I have learned from him, both academically and personally, will remain with me throughout my career.

I would also like to extend my heartfelt thanks to my parents, whose constant support and belief in my dreams have been the cornerstone of my academic and personal growth. Their encouragement fuelled my lifelong fascination with space exploration, which began as far back as I can remember. This fascination grew into a specific passion for recovery systems, particularly parachute dynamics, which I first explored during a high school project—a passion that ultimately led to this thesis.

A special mention goes to Diego for his exceptional support, including proofreading sessions and invaluable advise. His help and encouragement made this process far more manageable, and I am deeply grateful for his efforts.

To my peers and colleagues at TU Delft, thank you for enriching my academic journey with your camaraderie and collaboration. Whether through brainstorming sessions, shared struggles, or moments of celebration, your presence has made this experience unforgettable.

Completing this thesis has been the most challenging yet rewarding experience of my life. The process has pushed me to grow in ways I never imagined, and I am incredibly proud of the lessons I have learned and the resilience I have built along the way.

Sowndariya Dhiyaneeswaran
Delft, 14^{th} *January, 2025*

1

INTRODUCTION

Titan, Saturn's largest moon, presents a unique opportunity to advance our understanding of planetary atmospheres and surface environments. With its dense nitrogen-rich atmosphere, low gravity, and hydrological cycle of liquid hydrocarbons, Titan closely resembles early Earth. These attributes make it a prime candidate for studying planetary evolution and prebiotic chemistry while offering significant challenges for precision landing technologies. Targeted exploration of Titan's scientifically rich regions, such as hydrocarbon lakes, dunes, and craters, requires advanced descent systems capable of navigating its dynamic atmosphere and achieving high landing accuracy. This thesis focuses on addressing key challenges associated with parafoil descent systems, including stability under Titan-like conditions, aerodynamic sensitivities, and environmental disturbances such as winds. This chapter begins by setting the context and motivation for studying Titan, highlighting the challenges posed by its atmospheric and surface conditions, and emphasizing the importance of parafoil systems as a solution for precision landings. It then identifies key challenges specific to parafoil systems on Titan, such as aerodynamic performance in varied gravity and atmospheric density, and the effects of wind variability on stability. These challenges lead to the identification of research gaps, including limited studies on lateral stability and insufficient validation of high-fidelity parafoil models under Titan-like conditions. The overarching research question and objectives of this study are presented, which focus on enhancing the understanding of parafoil stability, dynamic coupling, and environmental effects on performance. Finally, the scope and structure of the thesis are outlined, providing an overview of the research approach, the development and verification of 6DOF and 9DOF models, and the methods used to analyse parafoil dynamics in Titan's atmosphere.

1.1. CONTEXT AND MOTIVATION

Featuring a thick nitrogen-rich atmosphere, Titan has a hydrological cycle driven by liquid hydrocarbons, and a surface rich in organic materials [1]. These unique features make Titan an ideal target for studying prebiotic chemistry and planetary evolution (Hörst, 2017). Missions like Cassini-Huygens have provided invaluable insights into Titan's atmosphere and surface (Coustenis and Raulin, 2023), but significant challenges remain, particularly in achieving precision landing.

The 2005 Huygens probe revealed large dispersions in descent trajectories, driven by high winds and extended descent phases (Quadrelli et al., 2019). These challenges limit the ability to land in scientifically rich areas (Schutte et al., 2020), such as hydrocarbon lakes or shorelines, that could provide insights into Titan's chemistry and habitability. Future missions require advanced landing systems capable of mitigating environmental disturbances, particularly wind, and ensuring stability during descent.

Parafoil systems have emerged as a promising solution for precision landings on Titan. However, significant gaps remain in understanding parafoil dynamics under Titan-like conditions, especially

[1] see APL, 2017

concerning lateral stability and high-fidelity modelling of aerodynamic and inertial interactions. This research aims to address these gaps, providing actionable insights for designing robust parafoil systems that can operate in Titan's extreme environment.

1.2. The Role of Parafoil Systems in Precision Landing

Parafoils are a promising solution to the precision landing challenge. Unlike traditional parachutes, which provide stability but limited control, parafoil systems offer greater manoeuvrability and allow precise terminal descents (Leeman et al., 2022). On Earth, parafoils have demonstrated their ability to deliver payloads with high accuracy, and their potential for planetary exploration is increasingly recognized (Quadrelli et al., 2019). For Titan, where the dense atmosphere provides significant aerodynamic lift and control potential, parafoils could enable controlled descents with minimal fuel consumption.

However, the design and implementation of parafoil systems for Titan face unique challenges. Titan's dense atmosphere, low gravity, and predominantly zonal wind patterns significantly alter the aerodynamic forces acting on parafoil systems. Additionally, the inherent flexibility of parafoils and their coupling with a payload introduce complex dynamics that must be understood to ensure stability during descent.

1.3. Challenges of Parafoil Systems on Titan

Titan presents a unique set of challenges for precision landing, particularly when employing parafoil systems. These challenges, intricately woven into the it's distinctive atmosphere and surface conditions, demand innovative solutions for successful descent and controlled landing. A summary of these challenges highlighted by the work done in a study about precision landing for Titan (Quadrelli et al., 2019) includes:

- ***Aerodynamic Performance in Varied Gravity and Atmospheric Density***: The dissimilar gravity and atmospheric density on Titan give rise to unprecedented aerodynamic challenges for parafoil systems. Remarkably, the distinct aerodynamic performance under these conditions has yet to be comprehensively modelled.

- ***Optimal Deployment of Drogue and Parafoil in High Winds***: Precision landing demands a meticulous strategy for deploying both the drogue and parafoil. Initial drogue deployment at approximately 140 km Above Ground Level (AGL) is critical. High-altitude winds pose a formidable challenge, causing significant dispersion during the extended parachute descents. The optimal descent rates and deployment altitudes to mitigate dispersion remain elusive and are contingent on complex variables such as wind profiles and touchdown velocity constraints.

- ***Variable and Zonal Winds***: Titan's winds, characterized by high variability, exhibit a predominantly zonal direction. This peculiar wind profile, particularly below 50 km AGL, offers both challenges and simplifications for designing algorithms for guidance and onboard wind estimation.

- ***Landing in Liquid Bodies and Entrapment Avoidance***: The prospect of landing in Titan's lakes or seas necessitates a nuanced terminal descent strategy. Preventing parafoil entrapment and making decisions on turning over liquid bodies or following shorelines add layers of complexity. The guidance algorithm must navigate the parafoil through this intricate dance while maintaining visibility of the landing site.

- ***Camera-Based Navigation Stability***: Successful navigation relying on cameras demands a stable imaging platform. Drawing from the experience of the Huygens probe and prior studies of parachute dynamics, camera-based navigation stability is anticipated not to be a significant impediment, but it remains a critical consideration.

1.4. Research Gap and Objectives

While parachute dynamics are relatively well understood, the behaviour of parafoil systems in extraterrestrial environments remains underexplored. Existing studies primarily focus on Earth-based applications or Mars exploration, leaving significant gaps in understanding how parafoils perform under Titan-like conditions. This study aims to address several critical research gaps that are essential for advancing parafoil-based precision landing systems:

Lateral Stability: Most prior research emphasizes longitudinal stability, with limited consideration of lateral stability and sideslip dynamics. Titan's zonal winds and varying wind conditions pose unique challenges that can induce significant lateral disturbances during descent. This study addresses this gap by conducting extensive wind-induced stability tests on both 6DOF and 9DOF parafoil models, including the impact of lateral wind disturbances on sideslip angle (β), which is generally not sufficiently investigated.

Verification and Validation of 9DOF Models: Few studies have systematically verified and validated complex 9DOF parafoil models by first establishing confidence in simpler, well-understood 6DOF models. This step is crucial for ensuring that the added degrees of freedom in 9DOF models accurately capture the dynamics of flexible parafoil-payload systems. This research rigorously verifies the 6DOF model and then extends it to a 9DOF model, providing a reliable framework for analysing parafoil dynamics under Titan-like conditions.

Analysis of Rotational Behaviour Differences: The distinct rotational behaviour of the flexible parafoil and its coupled payload (capsule) has not been extensively studied. Most existing research treats the parafoil-payload system as a single rigid body, overlooking the dynamic coupling effects and the redistribution of sensitivities between the two components. This study fills this gap by separately analysing the rotational dynamics of the parafoil and the capsule in the 9DOF model, identifying how aerodynamic parameter variations affect each component differently.

Comprehensive Environmental Testing: Environmental variability, particularly wind disturbances, plays a crucial role in parafoil descent performance. However, many studies do not incorporate detailed wind models or assess the impact of dynamic wind fields on stability. This research includes wind sensitivity analyses with both steady-state and turbulent wind profiles, providing insights into how Titan's atmospheric conditions influence the parafoil's descent and stability.
By addressing these gaps, this study aims to enhance the understanding of parafoil stability, dynamic coupling, and environmental influences, laying the groundwork for future precision landing missions on Titan.
The main research question driving this study is:

To what extent can high-fidelity dynamic modelling enhance the understanding of parafoil stability and performance for planetary landings?

To address this question, the following sub-questions are investigated:

1. **Stability in Dynamics**: What are the key factors influencing the rotational stability of parafoil systems during descent on Titan?

   Identifying these factors provides a foundation for understanding how the parafoil behaves under open-loop conditions and helps determine the inherent stability characteristics of the system.

2. **Dynamic Coupling Effects**: How do flexibility and coupling between the parafoil and capsule impact the overall dynamics of the system?

These interactions are crucial for capturing the nuances of parafoil behavior, especially when dealing with multi-body dynamics influenced by aerodynamic forces.

3. **Environmental Influence**: How do Titan's wind profiles and atmospheric variability affect the stability of parafoil landings?

   Titan's dense atmosphere and varying wind conditions introduce additional challenges that need to be quantified to ensure accurate modeling and mission success.

4. **Aerodynamic parameters**: How do variations in key aerodynamic parameters influence the stability characteristics of the parafoil during descent?

   This investigation helps assess the sensitivity of the system to aerodynamic changes, ensuring robustness across different descent scenarios.

Each of these sub-questions builds on the previous one, collectively enhancing our understanding of parafoil stability and performance in extraterrestrial environments.

1.5. Scope of the Study

This thesis focuses on high-fidelity modelling and analysis of parafoil systems to investigate their stability and dynamic behaviour in Titan-like conditions. The scope of the study is limited to open-loop stability analysis, where the system's inherent response to perturbations is evaluated without active control inputs. Key aspects of the study include:

- Developing 6DOF and 9DOF models to simulate the dynamics of parafoil systems and their coupling with a payload.
- Verification and validation of 6DOF and 9DOF models to ensure physical and computational accuracy.
- Performing sensitivity analyses to identify the parameters most critical to stability and descent performance.
- Testing the models under Titan-like wind conditions, including steady-state winds and turbulence, with a focus on longitudinal stability.
- Comparing the stability and performance of parafoil systems with known traditional parachutes to evaluate their relative advantages.

The study progresses from simpler parachute models, used for initial verification and validation, to more complex parafoil models, culminating in a detailed analysis of the 9DOF parafoil-capsule system.

1.6. Thesis Structure

The remainder of this thesis is organized as follows. chapter 2 presents a review of mission heritage and requirements, focusing on Titan exploration and relevant landing technologies. chapter 3 provides an overview of Titan's environment, including atmospheric models and wind profiles, which are critical for understanding the descent dynamics. chapter 4 introduces the flight mechanics used in this study, covering reference frames, state variables, and equations of motion of a 6DOF system. chapter 5 details the development of the 9DOF parafoil model, including its aerodynamic properties and dynamics. chapter 6 outlines the software architecture, verification, and validation approach used to implement and assess the models. chapter 7 presents the results of sensitivity analysis and wind tests, focusing on the stability of both the 6DOF and 9DOF parafoil systems. Finally, chapter 8 concludes the thesis by summarizing key findings and providing recommendations for future work.

2

Mission Heritage and Requirements

Understanding the heritage of Titan exploration and the requirements for future missions provides critical context for the development of advanced landing systems. This chapter reviews key past and planned missions to Titan, highlighting their scientific contributions and the challenges faced during Entry, Descent, and Landing (EDL). These insights inform the design and verification of parafoil-based systems that aim to achieve precise and controlled landings on Titan's diverse and challenging terrain.

2.1. Exploration of Titan

Since its discovery in 1655, Titan has intrigued scientists due to its dense and hazy atmosphere. Early observations using telescopes hinted at a dynamic environment, but it wasn't until the space age that close explorations were possible. In 1979, Pioneer 11's flyby confirmed Titan's temperature and mass measurements. Subsequent flybys by Voyager 1 and 2 provided more detailed information about Titan's atmosphere, surface temperature, and air pressure [1].

The most significant exploration came with the European Space Agency's Huygens probe, which landed on Titan in 2005. This mission marked the first landing in the outer solar system and remains the only landing on Titan to date. Huygens provided detailed images and atmospheric data during its descent and from the surface, revealing clouds, subsurface oceans, and a landscape shaped by both liquid and solid hydrocarbons (Barnes, 2021). These discoveries highlighted Titan's potential for studying prebiotic chemistry and its dynamic surface processes.

Building on Huygens' success, NASA's Dragonfly mission, planned for arrival in 2034, will explore Titan's habitability and prebiotic chemistry. Dragonfly, a rotorcraft with a nominal mass of 400-450 kg, will perform multiple flights between sites of interest after its initial landing (R. Lorenz et al., 2018). The mission's Entry, Descent, and Landing (EDL) sequence involves an aeroshell, drogue parachutes, and a powered descent by the rotorcraft [2]. Dragonfly's primary landing site is the dune fields of the northwestern Shangri-La sand sea, near the Selk crater (R. D. Lorenz et al., 2021).

The Selk crater, approximately 90 kilometres wide, offers a scientifically compelling target due to its shallow slopes and potential water-rich materials (R. D. Lorenz et al., 2021). This region, where molten ice may have interacted with organic materials, provides a unique opportunity to study prebiotic chemistry (Soderblom et al., 2010). Furthermore, the crater's relatively smooth topography makes it suitable for autonomous landing, addressing the critical need for safe EDL sites on Titan. The thick atmosphere and dynamic wind conditions that influenced Huygens' descent will also affect Dragonfly, underscoring the importance of robust and precise landing technologies.

[1] see "Titan Exploration", 2023

[2] see ("Dragonfly Mission Overview", 2022)

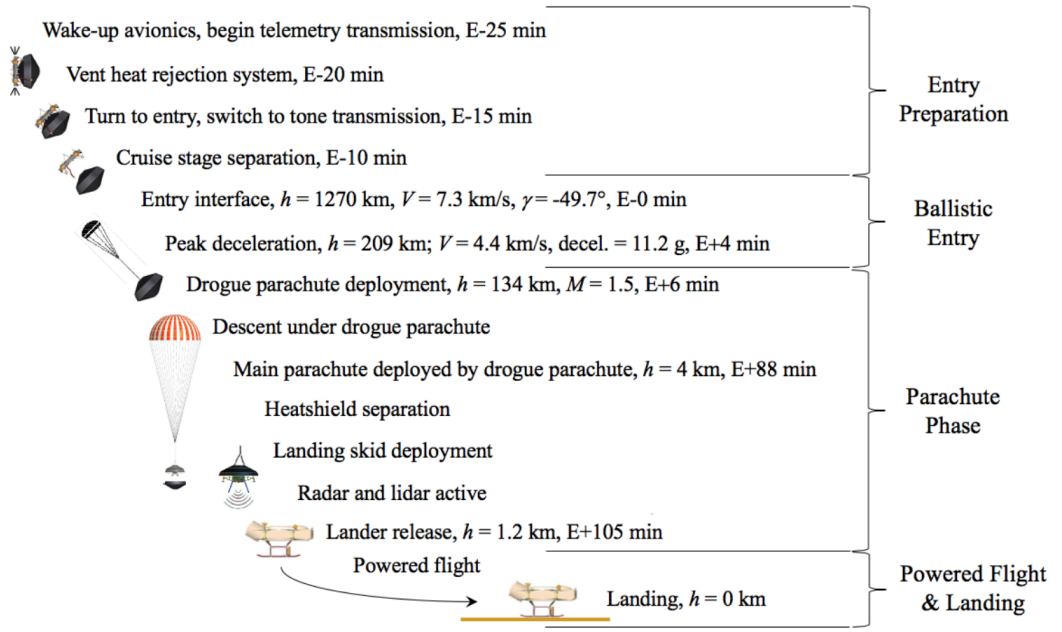

Figure 2.1: Entry, Descent, and Landing order of operations for the Dragonfly mission (Wright, 2019)

The insights gained from past and upcoming missions to Titan highlight the need for advanced EDL systems capable of handling its unique atmospheric dynamics. Parafoil-based systems, with their potential for controlled descent and landing precision, are a promising approach for future missions seeking to expand our understanding of Titan's complex environment.

2.2. Entry, Descent, and Landing Technologies

Presently, EDL systems utilize advanced aerodynamics, thermal protection, and guidance algorithms. Steerable parachutes, like parafoils, offer improved control during descent compared to traditional parachutes, making them suitable for missions like Dragonfly. Among the various steerable parachute systems—such as parasails, cloverleaf designs, and parawings—the parafoil stands out due to its superior glide ratio, manoeuvrability, compact stowability, and extensive history of testing and successful use (Jann, 2006).

The illustration provided in Figure 2.2 showcases a spectrum of steerable parachute concepts; out of which parafoils provide extended lateral control during descent, which is particularly advantageous in Titan's dense atmosphere, allowing the vehicle to navigate to a precise landing site from a considerable distance. This precision landing capability reduces the reliance on fuel-consuming propulsion systems, leading to lighter payloads and lower launch costs. The passive glide characteristics of parafoils also contribute to sustainability by minimizing the environmental impact associated with fuel production and consumption.

Compared to traditional EDL systems, such as ballistic entry capsules or powered descent vehicles, parafoils offer significant advantages. Ballistic capsules follow predetermined trajectories with limited control, while powered descent systems require substantial fuel reserves to achieve controlled landing. In contrast, parafoils provide manoeuvrability and precision without the need for extensive propulsion, making them a fuel-efficient and sustainable option for planetary exploration missions.

Also, parafoils can be deployed at higher altitudes, enabling longer controlled descent phases. This extended descent time allows for avoidance of hazardous terrain and selection of optimal landing sites, enhancing mission safety and scientific return. However, the complexity of parafoils also re-

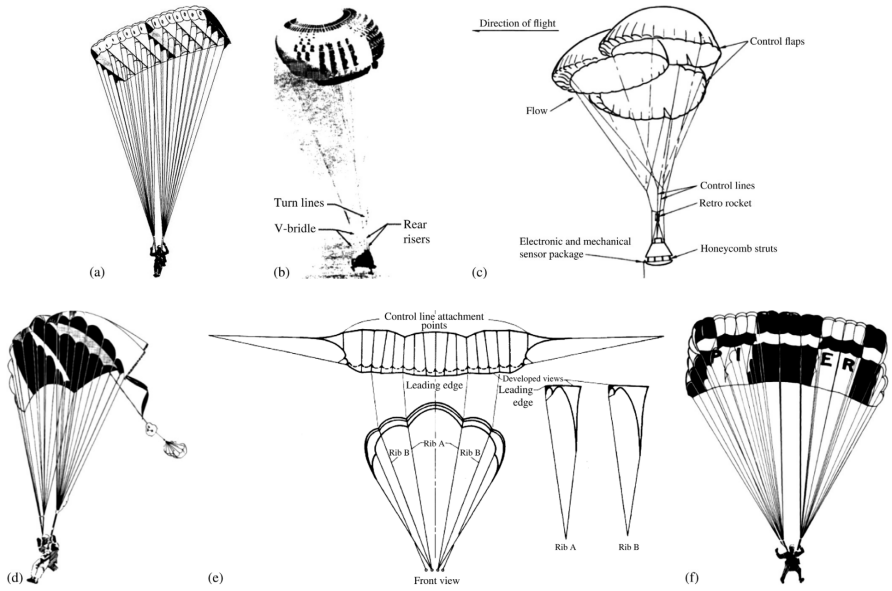

Figure 2.2: Steerable parachute concepts. (a) Parafoil. (b) Parasail. (c) Cloverleaf. (d) Parawing. (e) Sailwing. (f) Volplane. (Leeman et al., 2022).

quires advanced guidance algorithms and accurate aerodynamic models to ensure stable and controlled descent. Continued advancements in autonomous navigation and real-time trajectory optimization are essential to fully harness the benefits of parafoil-based EDL systems for future missions to bodies like Titan.

2.3. Parafoil Model Complexity

Parafoil systems can be modelled with varying levels of fidelity to capture the interactions and dynamics between the canopy and payload. These models, ranging from simple rigid-body approximations to high-fidelity multi-body systems, differ in their ability to simulate translational and rotational motions, canopy flexibility, and payload dynamics. Table 2.1 provides a comparison of parafoil models with different degrees of freedom (DOF), highlighting the trade-offs between model complexity and computational feasibility. This study adopts the 9DOF model as it strikes a balance between capturing critical dynamics and ensuring computational efficiency, particularly for the descent and stability analyses relevant to Titan's atmospheric conditions.

The choice of a 9DOF model for this study is motivated by the need to accurately capture the complex interactions between the parafoil and payload during descent in Titan's atmosphere. The 9DOF model allows for independent motion between the parafoil and payload, enabling the simulation of relative dynamics and flexibility effects that are critical for stability and control analysis. Additionally, it offers a balance between model fidelity and computational feasibility, making it suitable for iterative simulations and control strategy development.

Furthermore, comparing the 9DOF model with the well-established 6DOF model provides a framework for validating the enhanced capabilities of the higher-fidelity model. This comparative analysis forms a significant part of this research, contributing to the development of more reliable parafoil systems for planetary exploration missions.

2.4. Mission and System Requirements

Systems engineering is a critical aspect of modern aerospace projects, providing a structured approach to development, verification, and validation. Mission requirements outline the overarching

Table 2.1: Comparison of Parafoil Models with Different Degrees of Freedom

Model	Description of Dynamics and Coupling	Reference
4DOF	Single rigid body with restricted pitch and roll; captures only translational motion and yaw dynamics. Simplified model for basic trajectory studies.	Yang et al., 2014
6DOF	Single rigid body model capturing full 3D translational and rotational motion (pitch, roll, yaw). Parafoil and payload are treated as one coupled system.	Mooij, 1992
7DOF	A 6DOF model enhanced with an additional degree of freedom to capture payload swing about a single rotational axis (yaw). The connection is modelled with four riser attachment points allowing for payload yaw motion while restricting pitch and roll, closely approximating the relative parafoil-payload twist.	Gorman and Slegers, 2011, Gorman and Slegers, 2012
8DOF	Incorporates limited canopy flexibility or independent payload swing in two rotational planes (yaw and pitch). Two riser connections allow yaw and pitch dynamics but restrict roll, providing additional fidelity for complex aerodynamic and payload interactions.	Yakimenko, 2005a, Gorman and Slegers, 2011
9DOF	Two 6DOF models coupled through a hinge, allowing independent translational and rotational motion of the parafoil and payload. The hinge removes 3 degrees of freedom, introducing flexibility-induced oscillations.	Mooij et al., 2012, Prakash and Ananthkrishnan, 2006, Mooij et al., 2003

objectives of a mission, while system requirements specify the functionalities needed to achieve those objectives. In this work, defining both mission and system requirements ensures that the parafoil models meet their intended purpose effectively, particularly in the challenging conditions of Titan. This dual-level approach helps maintain clarity in development and ensures that all components are aligned with the overall mission goals.

2.4.1. Mission Requirements (MR)

- **MR-01: Parafoil Descent Stability** The parafoil system shall achieve a stable descent under Titan-like atmospheric conditions, with the peak angle of attack (α) oscillations converging to within 0.1 deg of the nominal value within 150 seconds.
- **MR-02: Environmental Adaptability** The system shall demonstrate stable performance under a range of Titan-like atmospheric conditions, including steady-state winds up to 10 m/s, turbulence, and gusts up to 5 m/s.
- **MR-03: Sensitivity Analysis** The system shall identify critical parameters influencing stability, such as aerodynamic coefficients, payload mass, and suspension line length, and quantify their impact through sensitivity analyses.
- **MR-04: Model Validation** The parafoil models (6DOF and 9DOF) shall be verified through energy conservation tests, angular momentum checks, and comparison with experimental or

historical data to ensure accuracy within 2%.

2.4.2. System Requirements (SR)

- **SR-01: Model Detail and Configurations** The simulation shall include 6DOF and 9DOF models. The 9DOF model shall represent the parafoil and payload as two distinct rigid bodies connected by a flexible joint, capturing relative motion dynamics.
- **SR-02: Environmental Modelling** The simulation shall incorporate wind, pressure, and temperature profiles of Titan's atmosphere, with sufficient resolution to model fluctuations in 10-meter altitude intervals.
- **SR-03: Stability Assessment** The system shall evaluate peak angle of attack (α) and descent dynamics under various environmental conditions, ensuring stable behaviour within 300 seconds of deployment.
- **SR-04: Computational Feasibility** The models shall run multiple sensitivity analyses and verification tests within a runtime of 1 hour per simulation on a standard computational workstation.
- **SR-05: Model Configurability** The simulation framework shall support interchangeable configurations, allowing testing with both parachute and parafoil systems.
- **SR-06: Energy and Momentum Conservation Tests** The system shall demonstrate conservation of total energy (kinetic and potential) and angular momentum, with minimal deviations during periods of significant dynamic changes.

3

TITAN'S ENVIRONMENT

This chapter explores Titan's dynamic atmosphere, highlighting the understanding gained from early space missions, up to the detailed measurements provided by the Cassini-Huygens mission. Titan's dense atmosphere, complex wind dynamics, and unique environmental conditions present significant challenges for spacecraft, especially during descent and landing phases. The selection of appropriate atmospheric and wind models is crucial to the design and operation of the parafoil descent system proposed in this study. This chapter presents the atmospheric model chosen to represent Titan's conditions, followed by an analysis of wind models used to simulate descent dynamics.

3.1. ATMOSPHERE MODEL

Titan's dense atmosphere is unique among solar system moons, consisting mainly of nitrogen, with significant amounts of methane and other hydrocarbons. This composition contributes to the moon's thick, hazy environment, which is heavily influenced by complex photochemical processes and methane cycles. Accurately modelling this atmosphere is critical for parafoil simulations, as it directly governs the aerodynamic forces, stability, and descent trajectory of the system. Understanding the nuances of Titan's atmospheric conditions provides the foundation for designing robust descent systems capable of achieving precision landings.

3.1.1. OVERVIEW OF AVAILABLE ATMOSPHERIC DATA

Numerous missions and studies have contributed to our understanding of Titan's atmosphere, offering valuable datasets that capture various aspects of its unique environment. These datasets are summarized below, with detailed descriptions of their contributions to atmospheric modelling.

Voyager Missions (Yelle et al., 1998): The Voyager 1 and 2 flybys provided the first detailed atmospheric profiles of Titan, serving as the foundation for early models. Utilizing instruments such as the Radio Science Subsystem (RSS), Infrared Spectrometer (IRIS), and Ultraviolet Spectrometer (UVS), the missions yielded measurements of temperature, pressure, and density across various altitudes. Although the data were groundbreaking at the time, their resolution and accuracy are limited compared to more recent missions. These early profiles highlighted the layered structure of Titan's atmosphere and its unique chemical composition, but the lack of direct in-situ measurements restricts their utility for high-fidelity modelling in modern studies.

Huygens Probe Data: The Huygens probe, as part of the Cassini-Huygens mission, remains the most significant source of direct in-situ atmospheric data for Titan. Three key instruments onboard the probe provided comprehensive insights:

- The **Huygens Atmospheric Structure Instrument (HASI)** recorded detailed vertical profiles of temperature, pressure, and density up to an altitude of 1380 km during its descent. HASI's data

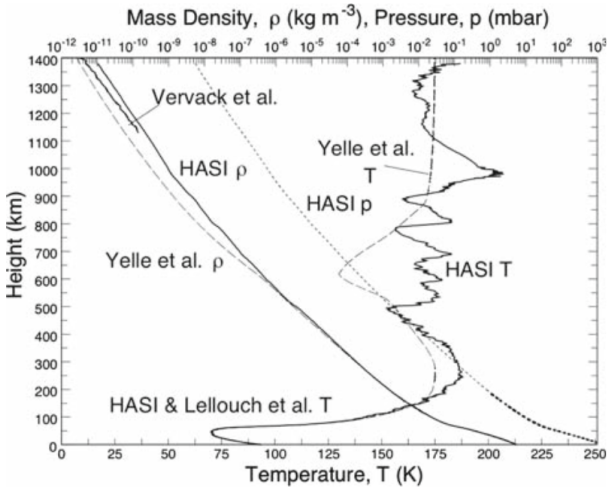

Figure 3.1: Comparison of density, pressure, and temperature profiles from HASI, Voyager, and Yelle et al. models. Adapted from Lebreton et al. (2009).

are particularly valuable due to their high resolution and precision, capturing fine-scale atmospheric variations critical for simulating parafoil dynamics. These measurements established a baseline for understanding Titan's thick atmospheric layers and dynamic behaviour.

- The **Gas Chromatograph Mass Spectrometer (GCMS)** analysed the atmospheric composition, revealing the relative abundance of nitrogen, methane, and other trace gases. This information provides essential inputs for modelling the thermodynamic and aerodynamic properties of the atmosphere, such as drag and lift forces on the parafoil system.
- The **Descent Imager/Spectral Radiometer (DISR)** contributed to understanding the interaction between Titan's atmosphere and surface. By observing haze properties, light scattering effects, and spectral variations, DISR added a crucial layer of detail to the atmospheric model, particularly in the lower altitudes where descent manoeuvrers are most critical.

Cassini Orbiter Data: The Cassini spacecraft provided extensive atmospheric data through instruments like the Composite Infrared Spectrometer (CIRS). CIRS measured thermal infrared emissions across Titan's atmosphere, producing temperature profiles and identifying the distribution of key gases. These data complement the Huygens measurements by extending the understanding of atmospheric dynamics at higher altitudes and over different regions of Titan. The ability to capture seasonal and spatial variations makes the Cassini dataset a valuable resource for refining atmospheric models used in parafoil simulations.

General Circulation Models (GCMs): GCMs represent a computational approach to simulating Titan's atmospheric behaviour, incorporating physical processes such as heat transfer, wind circulation, and methane condensation. These models are capable of predicting seasonal changes, global wind patterns, and temperature variations across altitudes and latitudes. While GCMs offer unparalleled insights into Titan's atmospheric dynamics, their complexity and high computational demand make them less practical for iterative stability analysis in the context of parafoil descent. Nevertheless, they remain a critical tool for understanding broader atmospheric trends and informing the design of simplified models.

3.1.2. Rationale for the Atmospheric Model Selection

The **Huygens Atmospheric Structure Instrument (HASI)** model, shown in **??**, was selected as the primary atmospheric model for this study due to its precision and relevance to simulating Titan's at-

mospheric conditions. The HASI data, obtained during the Huygens probe descent, provide vertical profiles of temperature, pressure, and density up to an altitude of 1380 km. These measurements are critical for simulating the aerodynamic forces and stability of the parafoil descent system.
Compared to earlier datasets, such as the Voyager missions (Yelle et al., 1998), and subsequent reanalysis models, HASI offers improved resolution and updated data reflective of Titan's atmospheric conditions during the probe's descent. Voyager data provided valuable insights into Titan's atmospheric structure but lacked the spatial resolution and accuracy needed for high-fidelity simulations. Meanwhile, models derived from the Voyager era and the Cassini Composite Infrared Spectrometer (CIRS) dataset (Lebreton et al., 2009), while valuable for studying broader atmospheric trends, do not capture the localized atmospheric variations needed for descent simulations.
Figure 3.1 illustrates the differences in density, pressure, and temperature profiles between the HASI, Yelle, and Voyager models. The HASI data closely align with recent measurements, capturing fine-scale variations that are particularly relevant for predicting aerodynamic behaviour during descent. This makes HASI the most appropriate model for the parafoil system design.
To account for variability in Titan's atmospheric conditions, a sensitivity analysis was conducted by applying a -20% to +20% variation in atmospheric density. This approach allows the simulation to assess the parafoil's performance under a range of plausible descent environments, focusing on the influence of density on aerodynamic forces and stability. While no specific variations were applied to temperature or pressure, the density sensitivity captures the primary atmospheric uncertainties relevant to the parafoil system's behaviour. This streamlined approach ensures robustness without overcomplicating the analysis.
The following key reasons justify the choice of the HASI model:

- **Precision and In-situ Nature:** HASI provides direct in-situ measurements, minimizing uncertainties compared to remote sensing methods. This is crucial for accurately capturing subtle variations in atmospheric parameters that influence parafoil dynamics.
- **Updated Dataset:** Derived from the Cassini-Huygens mission, HASI data reflect Titan's atmospheric conditions during the descent. In contrast, the Yelle and Voyager models represent earlier interpretations, which may not fully account for modern insights into Titan's atmosphere.
- **Density Profiles:** The density data provided by HASI are critical for simulating aerodynamic forces. Figure 3.1 highlights how the HASI density profile compares to the Voyager-based models, showcasing its higher resolution and coverage.
- **Relevance to Parafoil Dynamics:** Accurate data on temperature, pressure, and density are vital for predicting aerodynamic coefficients, lift, drag, and stability during the descent phase.
- **Scenario Flexibility:** By implementing hot, nominal, and cold scenarios, the model accommodates variability in atmospheric conditions, enhancing the robustness of the design.

The choice of the HASI model, combined with density and temperature variations, ensures a realistic and reliable framework for simulating Titan's atmospheric descent. This approach balances precision with computational efficiency, leveraging HASI's comprehensive dataset while incorporating broader atmospheric insights from other models.
Titan's atmospheric properties play a crucial role in understanding its descent environment and aerodynamic behaviour. The thick atmosphere, dominated by nitrogen, has a surface pressure 1.5 times that of Earth and a low surface temperature of 94 K. The combination of low gravity (1.352 m/s^2) and dense atmosphere significantly influences the behaviour of parachute and parafoil systems during descent. These parameters summarized in Table 3.1, provide the foundational context for the wind models used in the stability analysis, which capture the key interactions between the atmosphere and the descent systems.

3.1.3. Speed of Sound Model for Titan's Atmosphere

The speed of sound model implemented for Titan's atmosphere is based on thermodynamic properties of the atmospheric composition, following the methodology outlined in Mooij (1992). The model

Table 3.1: Physical Properties of Titan

Physical Properties	**Values**
Equatorial radius	$2575 \pm 2\,\text{km}$
Mass	$1.34553 \times 10^{20}\,\text{kg}$
Surface temperature	94 K
Surface pressure	1496 hPa (1.5 bar)
Surface gravity	$1.352\,\text{m/s}^2$ ($0.14\,g_{\text{Earth}}$)
Surface density	$1.880\,\text{g/cm}^2$
Geometric albedo	0.21
Gravitational parameter (μ)	$8978.13 \pm 0.06\,\text{km}^3/\text{s}^2$

considers the primary constituents of Titan's atmosphere—nitrogen (N_2), argon (Ar), and methane (CH_4)—to compute the speed of sound as follows:

1. The average molar mass (M) is calculated using the volume fraction (x_i) and molar mass (m_i) of each species:
$$M = \sum_{i=1}^{n} x_i m_i \tag{3.1}$$
2. The gas constant (R) is determined using the universal gas constant (R^*) and the computed molar mass:
$$R = \frac{R^*}{M} \tag{3.2}$$
3. The specific heat capacity at constant pressure (C_p) is calculated as a weighted sum of the specific heat capacities of each species ($c_{p,i}$):
$$C_p = 10^3 \frac{R}{R^*} \sum_{i=1}^{n} x_i c_{p,i} \tag{3.3}$$
4. The ratio of specific heats (γ) is determined as:
$$\gamma = \frac{C_p}{C_p - R} \tag{3.4}$$
5. Finally, the speed of sound (a) is computed as:
$$a = \sqrt{\gamma R T} \tag{3.5}$$

The table below summarizes the major constituents of Titan's atmosphere and the associated thermodynamic properties:

Table 3.2: Major constituents and thermodynamic properties of Titan's atmosphere (Mooij, 1992).

Species	**Molar Mass (kg/kmol)**	**Nominal Volume Fraction (%)**	**Specific Heat, C_p (J/mol K)**
N_2	28.0134	90.0	See Table 3.3
Ar	39.9480	7.0	See Table 3.3
CH_4	16.0426	3.0	See Table 3.3

The specific heat capacity values (C_p) at different temperatures are shown in Table 3.3:
To account for variations in Titan's atmospheric composition, three cases were modeled:

- **Minimum Atmosphere:** 100% N_2.

Table 3.3: Specific heat at constant pressure (C_p) for major constituents (Mooij, 1992).

Temperature (K)	C_p for N_2 (J/mol K)	C_p for Ar (J/mol K)	C_p for CH_4 (J/mol K)
100	29.104	20.786	33.275
200	29.107	20.786	33.507
298.15	29.124	20.786	35.695
300	29.125	20.786	35.765
400	29.249	20.786	40.631
500	29.580	20.786	46.627
600	30.109	20.786	52.742
700	30.754	20.786	58.603
800	31.433	20.786	64.084
900	32.090	20.786	69.137
1000	32.696	20.786	73.746

- **Nominal Atmosphere:** 90% N_2, 7% Ar, and 3% CH_4.
- **Maximum Atmosphere:** 80% N_2, 20% Ar, and 0% CH_4.

While all three cases were evaluated, the nominal atmospheric composition was ultimately used for all simulations and sensitivity analyses. Later, the sensitivity analysis (in chapter 7) focused solely on varying the atmospheric density (ρ) to assess its impact on aerodynamic stability.

3.2. Titan's Wind Environment

Titan's wind dynamics are critical to understanding the stability and control of parafoil systems during descent. Choosing an appropriate wind model is essential to capture the wind speed variations and disturbances that influence the descent trajectory.

3.2.1. Overview of Wind Data and Models

Titan's winds are influenced by factors such as its thick atmosphere, seasonal cycles, and methane-based weather systems. Available wind models for Titan include:

- **General Circulation Model (GCM)**: This detailed model provides global wind patterns and captures seasonal variations. GCMs are particularly useful for trajectory simulations that require accurate meridional and zonal wind profiles. However, the available GCM data from previous studies typically cover lower altitudes, such as 10 km and below, which makes them impractical for the higher-altitude descent phases analysed in this study.
- **Flasar Wind Model**: This simplified model focuses on steady-state zonal winds and is computationally efficient, making it suitable for stability simulations. It provides a good approximation of wind conditions at the descent altitudes relevant to this study.

3.2.2. Selected Wind Models

For this study, the **Flasar wind model** and a **6-*t* gust model** were chosen to represent Titan's wind environment. These models provide a balance between accuracy and computational efficiency, making them suitable for extensive simulation runs.

Flasar Wind Model Adjustments

The Flasar wind model was adapted from Mooij (1992) where it was used to simulate the descent of the Huygens probe and parachute, starting from much higher altitudes (around 120 km) where wind speeds can reach up to 200 m/s. However, since this study focuses on lower altitudes, beginning at 40 km, the wind speeds are significantly lower.

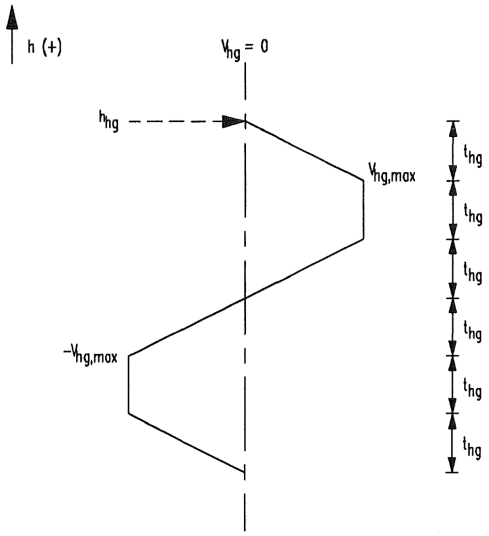

Figure 3.2: Horizontal wind gust profile for the 6-t gust model

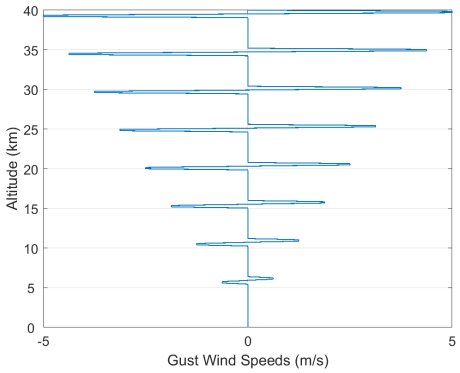

Figure 3.3: 6-t gust model applied at various altitude points throughout the trajectory

Based on data from Lebonnois et al. (2012), the maximum steady-state wind speed used in this study was reduced to **20 m/s**. The wind velocity V_{ss} in the Flasar model is expressed as:

$$|V_{ss} - V_{ss,s}| \leq V_{ss,\max} \left[1 + \frac{1}{8} \ln\left(\frac{p_{\text{ref}}}{p}\right)\right] \cos\delta \tag{3.6}$$

where:

- V_{ss} is the steady-state wind velocity (m/s),
- $V_{ss,s}$ is the surface wind velocity ($|V_{ss,s}| < 2\,\text{m/s}$),
- $V_{ss,\max}$ is the adjusted maximum wind velocity (20 m/s),
- p_{ref} is the reference pressure (50 N/m^2),
- p is the atmospheric pressure,
- δ is the moon-centric latitude.

This adjusted model captures the steady-state wind profile at lower altitudes while remaining computationally efficient for iterative stability testing.

6-t Gust Model

In addition to steady-state winds, the 6-t gust model was applied to simulate transient wind disturbances during descent. This model seen in Figure 3.2 introduces sudden changes in wind velocity, providing a realistic test for the parafoil's robustness against gusts. Consulting the maximum occurring winds in the equatorial region of Titan and knowing that at the surface it eventually drops down to 0 m/s (R. D. Lorenz, 2017), the 6-t) gust model was applied at several points throughout the trajectory from the 40 km to the surface at 5 km intervals. This was a choice based on studying maximum wind shears and a uniform decrease in the magnitude of the total gust was created just to be able to have a good design space to test potential gusts of Titan without having access to direct gust data on Titan.

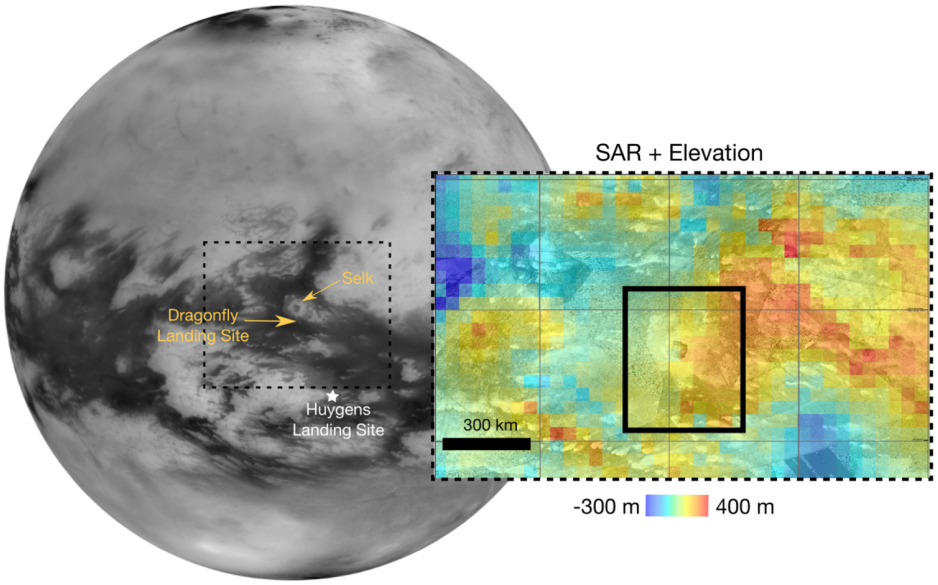

Figure 3.4: The Selk crater imaged on Titan

3.2.3. Rationale for Using the Flasar and 6-t Gust Models

Initially, the General Circulation Model (GCM) was considered due to its extensive use in previous studies for simulating Titan's atmospheric dynamics. For instance, a previous study utilized a GCM tailored to a balloon trajectory at altitudes around 10 km and below. However, applying this model to the higher altitudes relevant to this study (starting at 40 km) would have required regenerating wind data for the entire altitude range, which was computationally impractical within the scope of this research. It was determined that for the purpose of this stability study, focusing on the interaction dynamics of the parafoil, a combination of the Flasar wind model and a simple 6-t gust model was sufficient. This approach provided an effective representation of both steady-state winds and transient gust disturbances without the computational burden of the GCM.

The selection of the Flasar and 6-t gust models over the GCM was thus driven by the following factors:

- **Computational Feasibility**: The GCM's detailed simulations are computationally intensive. The Flasar model allows for efficient stability analyses without excessive runtime.
- **Altitude Coverage**: The GCM data available only extend up to 10 km, while the descent phase in this study begins at 40 km. The Flasar model provides a suitable wind profile for these altitudes.
- **Study Objectives**: This research focuses on stability and control of parafoils under representative Titan conditions. The Flasar model, combined with dynamic gusts, captures the essential wind dynamics required for this analysis.

3.3. Potential Landing Sites on Titan

Titan's unique environment, comprising methane lakes, expansive dune fields, icy plains, and cryovolcanoes, presents diverse opportunities for scientific exploration. Selecting a suitable landing site for a precision landing mission on Titan depends on multiple factors: scientific value, accessibility, and safety of descent. Insights gained from the atmospheric conditions and wind models are instrumental in understanding which locations are suitable for deploying the parafoil descent system. This section combines the environmental context established earlier with the mission heritage discussion to evaluate potential landing sites of interest for a parafoil-based descent on Titan.

3.3.1. Scientific Motivation and Environmental Considerations

The mission heritage discussed in Chapter 2 highlighted Titan's importance as a scientific target due to its similarities to prebiotic Earth, rich atmospheric composition, and unique surface features. The Huygens mission and upcoming Dragonfly mission have provided invaluable insights, but many regions remain unexplored. The diverse environments on Titan—from dune fields to methane seas—provide opportunities to further understand organic chemistry, surface-atmosphere interactions, and geological activity.

The atmospheric and wind conditions on Titan, particularly as characterized by the selected models, play a key role in determining the feasibility of landing a parafoil-based system at various potential sites. Factors like atmospheric density, wind variability, and surface conditions are all critical to ensuring a controlled descent. The following landing sites have been selected based on their scientific interest and their compatibility with the parafoil's capabilities.

3.3.2. Landing Site Selection: Suitability for Parafoil Descent

Using insights from Titan's atmospheric and wind models, potential landing sites were evaluated to align with the mission's scientific objectives and support a parafoil-based precision descent system. These sites were selected based on factors such as surface composition, atmospheric conditions, and accessibility to scientifically interesting features. The mission design prioritizes equatorial regions due to their relatively steady eastward zonal winds, which are less chaotic compared to the highly variable wind patterns at higher latitudes. This focus on equatorial entry enhances the predictability of wind profiles, simplifies trajectory planning, and minimizes landing hazards, making these zones particularly suitable for controlled descent.

- **Selk Crater:** Situated at approximately $7^\circ N$, $199^\circ W$, Selk Crater is a scientifically significant site characterized by evidence of organic compounds and past liquid water activity. Measuring about 90 km in diameter, it offers an excellent opportunity for astrobiological studies. This location has been targeted for the upcoming Dragonfly mission, highlighting its relevance for Titan exploration. The relatively smooth terrain near the crater and manageable equatorial wind conditions make it ideal for a parafoil-assisted landing.
- **Dune Fields:** Titan's equatorial dune fields, such as those in the Shangri-La or Belet regions, are vast expanses of linear dunes composed of hydrocarbon-rich sediments. These regions, spanning $10^\circ S$ to $10^\circ N$, are ideal for studying aeolian processes and Titan's organic chemistry. The relatively smooth and expansive terrain, coupled with steady wind profiles, allows for safer landing operations. The parafoil descent system is particularly effective in these areas, enabling precise trajectory adjustments to avoid hazardous features like steep dunes or irregular surfaces.
- **Huygens Landing Site:** The European Space Agency's Huygens probe successfully landed at $10.3^\circ S$, $192.3^\circ W$ in 2005, providing invaluable data for future mission designs. This location, near the boundary between the bright region Adiri and the dark region Shangri-La, remains a point of interest for its geologically diverse features. By revisiting this site with a parafoil system, further insights could be gained into Titan's surface processes and atmospheric interactions.
- **Cryovolcanoes and Impact Craters:** Cryovolcanoes such as Sotra Patera ($15^\circ S$, $40^\circ W$) and impact craters like Sinlap provide unique opportunities to study Titan's subsurface and internal processes. These locations are scientifically valuable for investigating cryovolcanic activity and the dynamics of impacts in a dense atmosphere. Although the rugged terrain near these features poses landing challenges, the parafoil's high glide ratio and ability to navigate steep or uneven regions ensure a controlled descent trajectory. Gust simulations and wind variability studies enhance the robustness of the system for these complex sites.
- **Methane Lakes and Seas:** Landing near large methane seas like Kraken Mare ($68^\circ N$, $310^\circ W$) or Ligeia Mare offers opportunities to study Titan's methane and ethane cycles and their interaction with the atmosphere. Despite the more variable wind conditions at higher latitudes,

these regions remain attractive for their scientific significance. The parafoil's manoeuvrability minimizes lateral drift, ensuring precise landings near these liquid bodies for in-depth exploration.

- **Icy Plains and Tectonic Features:** Extensive icy plains and tectonic regions, such as those in Xanadu, provide relatively flat surfaces suitable for safe landings. These regions offer opportunities to study surface weathering, tectonic activity, and atmospheric interactions. The parafoil system's ability to navigate and adapt to the wind conditions prevalent in these areas enhances the viability of these sites for exploration while reducing landing risks.

By targeting these carefully selected sites, particularly those in equatorial regions like Selk Crater and the Shangri-La dune fields, the mission can take advantage of more predictable atmospheric conditions. These choices enable safer, more controlled landings and ensure the scientific objectives of exploring Titan's geology, organic chemistry, and atmospheric dynamics are met with maximum efficiency and reliability.

3.3.3. Integration of Atmospheric Insights and Landing Strategy

The selection of a landing site on Titan is heavily influenced by the dynamics of Titan's atmosphere and wind environment. The in-situ atmospheric data provides an accurate understanding of temperature, pressure, and density variations, forming the foundation for modelling the descent. The combination of steady-state winds and randomly distributed gusts ensures that descent simulations capture both steady and transient effects, providing confidence in the parafoil system's adaptability throughout the descent.

The chosen landing sites align with the practical capabilities of the parafoil system. Sites near methane lakes require careful navigation to minimize lateral drift, but the reduced wind magnitudes at lower altitudes provide favourable conditions for landing. For dune fields, steady-state winds enable a gradual descent, while the gusts are used to simulate potential disturbances. Similarly, landing near cryovolcanoes or impact craters is supported by the parafoil's manoeuvrability, particularly when considering the need to avoid steep or irregular terrain.

Titan's environmental diversity, from lakes and dunes to tectonic features, provides numerous scientifically compelling landing sites. Leveraging insights from the atmospheric and wind models, this study demonstrates that precision landings at these sites are feasible with the use of a steerable parafoil system. The understanding of atmospheric density, pressure, and wind profiles directly informs not only the selection of landing sites but also the design and execution of a safe and controlled descent. The parafoil's ability to adapt to wind variability across different altitudes is a key factor in ensuring successful landings, making it an ideal candidate for future Titan missions.

4

FLIGHT MECHANICS

Understanding flight dynamics is crucial for precision landings on Titan. The intricate dynamics involve the interaction of aerodynamic forces, gravitational influences, and propulsion components. Efficient navigation through Titan's distinct atmospheric conditions requires a meticulous understanding of spacecraft motion and control in three-dimensional space. This chapter delves into fundamental aspects such as reference frames, equations of motion, and the specific dynamics of parafoils in Titan's environment. This knowledge is essential for precise spacecraft manoeuvring, ensuring mission success despite the complexities posed by Titan's atmosphere and wind dynamics.

4.1. REFERENCE FRAMES

A reference frame is a system of coordinates or a set of axes used to define the position and orientation and can be used as a fundamental framework to describe the motion of a body. Different reference frames may be employed for specific purposes, such as the inertial reference frames, which are non-accelerating and non-inertial frames which are accelerating or rotating. In order to derive the necessary equations of motion for precision landing dynamics, the following reference frames elaborated by Mooij (1994) can be considered.

4.1.1. INERTIAL MOON-CENTRIC REFERENCE FRAME (I)

The origin of this frame coincides with the COM of the central body and the $X_I Y_I$ -plane with its equatorial plane. The Z_I-axis corresponds to the rotational axis of the central body and points north while the X_I-axis the points the position of the reference meridian at time t_0. The Y_I-axis completes the right-handed system. For re-entry systems applications, the motion of the rotational axis of the planet due to the gravitational influences of other bodies of the Solar System can be neglected.

4.1.2. ROTATING MOON-CENTRIC REFERENCE FRAME (R)

This frame corresponds to the I frame at time t_0 and after any complete rotation of the central body around its axis. Indeed, assuming no nutation and precession, the Z_R-axis frame always coincides with the Z_I-axis but the X_R-axis constantly points to the reference meridian of the body and rotates with it. The Y_R-axis completes the right-handed system and also rotates with the central body. This frame is represented in Figure 4.1.

4.1.3. BODY REFERENCE FRAME (B)

The origin of this frame is fixed to the COM of the vehicle that is assumed to have a symmetry plane in the longitudinal direction. This plane is the $X_B Z_B$-plane where the X_B-axis points in the forward direction and the Z_B-axis points downwards. The Y_B-axis completes the right-handed system. This local reference is observable in Figure 4.2. Body frames can also be defined separately for different bodies such as for the chosen 9-DOF parafoil, which can have B_p for the body of the parafoil and B_r

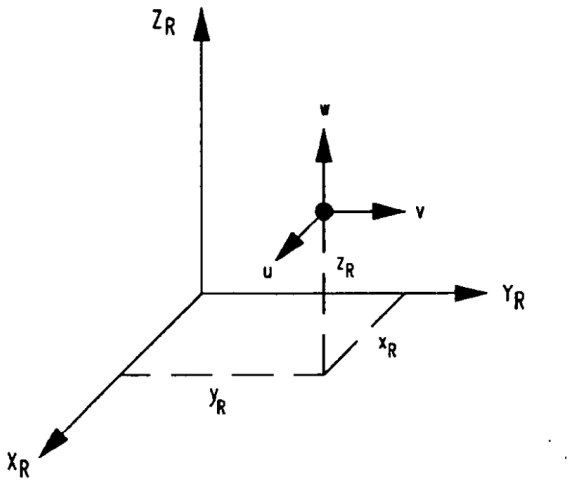

Figure 4.1: Definition of the Cartesian position and velocity components w.r.t. the rotating (R) frame (Mooij, 1994).

for the body of the store. Throughout the rest of this literature review, the equations of motion and mathematical models will use the aforementioned notations of the body frame interchangeable and use the specific subscripts as and when necessary to go into more detail.

4.1.4. Vertical reference frame (V)

The origin of this frame corresponds to the COM of the vehicle. The Z_V-axis points in the radial direction towards the COM of the central body, and the X_V-plane is perpendicular to it and points to the northern hemisphere. The Y_V -axis completes the right-handed system. The $X_V Y_V$-plane perfectly coincides with the local horizontal plane when the central body is a sphere.

4.1.5. Trajectory reference frame, airspeed based (TA)

The origin of this frame corresponds to the COM of the vehicle. The X_{TA}-axis points in the same direction as the velocity vector with respect to the atmosphere while the Z_{TA}-axis is perpendicular to X_{TA} and points downwards. The Y_{TA}-axis completes the right-handed system.

4.1.6. Aerodynamic Reference Frame (A)

The origin of the A frame corresponds to COM of the vehicle. The X_A-axis points in the direction of the velocity vector, which can be defined relative to the rotating moon-centric frame (ground-speed) or the atmosphere (airspeed), depending on the scenario. The Z_A-axis, perpendicular to X_A, is collinear with the aerodynamic lift force vector but oriented in the opposite direction. The Y_A-axis completes the right-handed coordinate system.
In the absence of banking, the A frame coincides with the TA frame, as depicted in Figure 4.3. This frame is used to define aerodynamic attitude angles (α_A, β_A, and σ_A) in conjunction with the body (B) and trajectory (TA) frames.

4.1.7. Wind Reference Frame (W)

The X_W-axis is aligned with the wind velocity vector and points in the direction the wind is blowing to. For a northern wind, this means the X_W-axis points south. The Z_W-axis is perpendicular to the horizontal plane and points downward for winds in this plane. The Y_W-axis completes the right-handed coordinate system. For cases involving non-horizontal winds, the W-frame can be derived from the vertical frame (V-frame) by applying right-handed rotations using the wind angles, as illustrated in Figure 4.4.

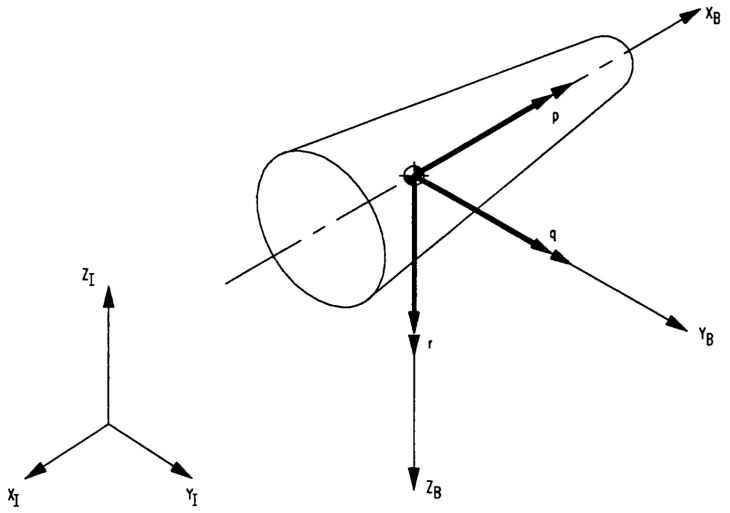

Figure 4.2: Figure showing that the origin of both the body (B) frame as well as the inertial (I) frame are located in the CoM of the body, with the body frame fixed to the body. Also derivable from this is the angular rate of the body: $\boldsymbol{\omega} = (\dot{\phi}, \dot{\theta}, \dot{\psi})^T$ (Mooij, 1994).

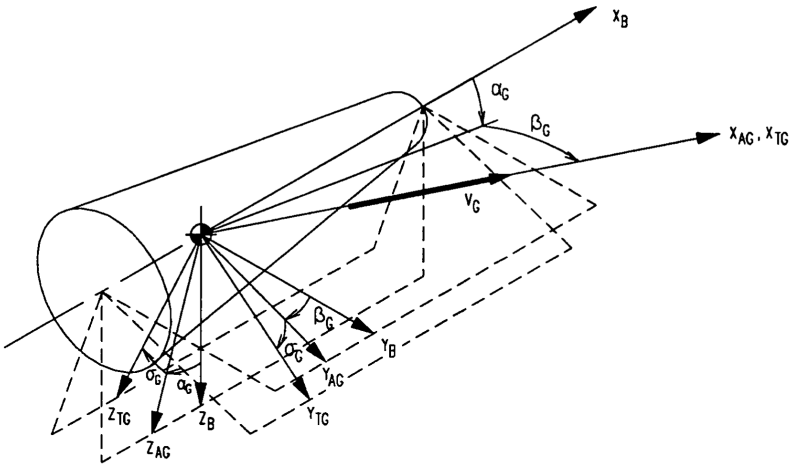

Figure 4.3: Definition of the aerodynamic attitude angles α_G, β_G and σ_G relating them to the body (B), aerodynamic (AG) and the trajectory (TG) frames, with the angles all defined positive. For this work, the A frame replaces the AG frame shown here, combining both groundspeed and airspeed reference definitions; similarly, the TG frame is replaced by the airspeed-based trajectory reference frame (TA). Image from Mooij (1994).

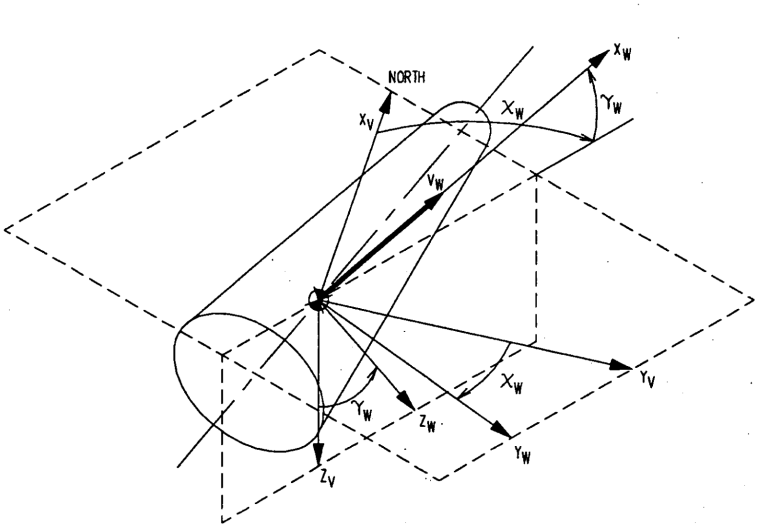

Figure 4.4: The relation between the wind reference frame (W) and the vertical reference frame (V). Taken from Mooij (1994).

4.2. State variables

In order to describe the mathematical state of a dynamic system to characterize the motion of a body at any point in time, a collection of state variables can be defined. These variables can be further classified as the position and velocity and the attitude and angular rates; all the necessary elements needed from initial time so that the defining functions can then allow one to be able to characterize the motion of the body at any given time.

4.2.1. Position and Velocity

To define the parafoil system's position and velocity, both the cartesian and spherical coordinates can be considered.

- **Cartesian coordinates:** The position components can be defined by x, y, z while the velocity components are $\dot{x}, \dot{y}, \dot{z}$. They are relatively simple to use and describe the position and velocity with respect to the I or R frames.
- **Spherical components:** With respect to the R frame, the position and velocity components can be described using spherical coordinates. The position is defined by three parameters: r, the radial distance from the CoM of the parafoil system to the origin of the reference frame; τ, the longitude measured positively eastward from the prime meridian, with values ranging from $0° \leq \tau < 360°$; and δ, the latitude measured from the equator, with positive values toward the north ($0° \leq \delta \leq 90°$) and negative values toward the south .

  The velocity components consist of the groundspeed magnitude V_G, which represents the total velocity relative to the planet's surface; the flight-path angle γ_G, defined as the angle between the velocity vector and the local horizontal plane, where positive values indicate the velocity vector pointing above the horizontal and negative values indicate the opposite; and the heading angle χ_G, which describes the direction of the projection of the velocity vector onto the local horizontal plane, measured positively eastward from the local north, with a range of $-180°$ to $180°$. The definitions of these positional and velocity components are illustrated in Figure 4.5, while their combination with cartesian velocity components is depicted in Figure 4.6.

In this work, as only the parafoil terminal descent phase is considered, the movement of the parafoil on a grid-like Cartesian system is sufficient for the majority of the calculations when it comes to

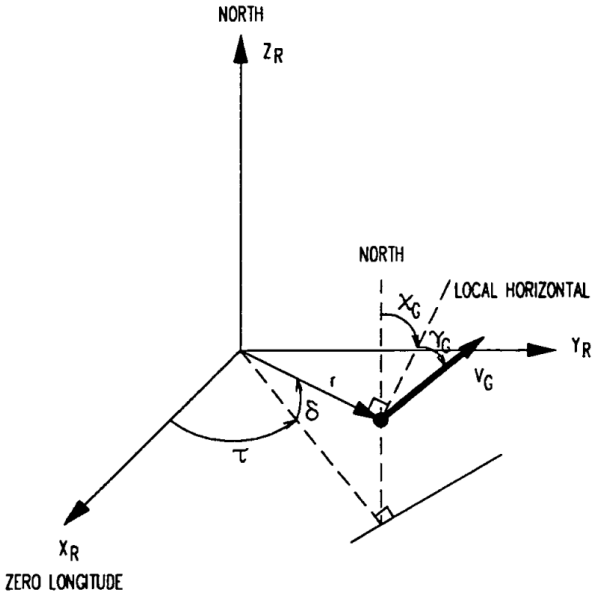

Figure 4.5: Definition of the six spherical flight parameters (Mooij, 1994)

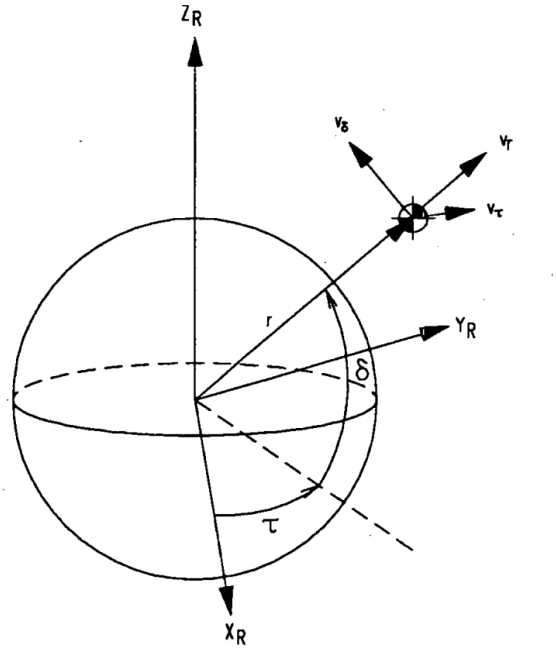

Figure 4.6: Definition of spherical position components and Cartesian velocity components (Mooij, 1994).

precision landing. It is also assumed that due to the problem being more localised than the global picture, although it is important to consider the spherical coordinates, the rotation effects of the planetary body itself can be ignored and the inertial frame of reference can be assumed. It is still important to consider the groundspeed velocity (V_G) vector defined in the spherical coordinate system to understand the airpseed (V_A) effects which will be discussed further and can be related to wind speed (V_W) as:

$$V_A = V_G + V_W \tag{4.1}$$

4.2.2. Attitude and angular rates

When it comes to the attitude of a spacecraft in general, it is defined as the orientation of a body-fixed frame relative to an external frame to analyse the motion characteristics of said spacecraft and design GNC systems. Different attitude sets such as Euler angles and quaternions can be considered. Although quaternions offer singularity-free orientation description and are thus beneficial for certain aspects of motion parametrization, Euler angles are easier to visualise and interpret which can be useful for understanding the motion. Both definitions are useful for various aspects of this study when it comes to body frame transformations (Euler angles) and representation of the rotational motion (quaternions).

- **Quaternions:** Quaternions, comprised of four elements $Q = (Q_1, Q_2, Q_3, Q_4)^T$, serve to define the orientation of a body frame in relation to the inertial geocentric frame. However, they are challenging to interpret because the individual components (Q_1, Q_2, Q_3, Q_4) do not directly correspond to intuitive physical quantities like angles or axes. Instead, quaternions represent orientation mathematically as a combination of a scalar and a vector in four-dimensional space, which is abstract and lacks immediate visual or physical meaning. This abstraction contrasts with Euler angles, for example, where each angle can be linked to a specific rotation about an axis, making them more intuitive but susceptible to singularities (e.g., gimbal lock).

- **Classical attitude angles:** The roll ϕ, the pitch angle θ, and the yaw angle ψ make up a set of Euler angles and are characterised by means of an Euler transformation starting from the inertial frame. The order of rotation transformation also makes a crucial impact on the application. The commonly accepted aerospace sequence of rotations is the 3-2-1 order (this visualization can be seen in Figure 4.7, involving a yaw rotation around the Z-axis, followed by a pitch rotation around the Y-axis, and concluding with a roll rotation around the X-axis which defines the attitude of the body frame w.r.t. inertial space but they may also define the attitude of the body w.r.t. the local horizontal plane. In this case, they can be used to define the orientation of the parafoil (body frame: B_p) w.r.t. the store (payload body frame: B_r).

- **Aerodynamic angles:** The aerodynamic angles are composed of the angle of attack α, the sideslip angle β, and the bank angle σ, which together form a set of Euler angles in the sequence 2-3-1. These angles define the orientation of the vehicle relative to the groundspeed (subscript G) when used in the equations of motion or relative to the airspeed (subscript A) in other contexts.

  The angle of attack α_G is defined in the range $-180° \leq \alpha_G < 180°$, where a positive α_G indicates a nose-up attitude. The sideslip angle β_G ranges from $-180° \leq \beta_G \leq 180°$, with a positive β_G signifying a nose-left attitude. Lastly, the bank angle σ_G is in the range $-180° \leq \sigma_G < 180°$, with a positive σ_G representing a right bank orientation. These aerodynamic angles are essential for describing the vehicle's attitude and are depicted in Figure 4.3.

4.3. Frame transformations

4.3.1. Unit axis rotations

Unit-axis transformations are the expressions of the transformations from one frame (right-handed Cartesian) to another, using unit-axis rotations: Directional cosine matrices or quaternions. The unit rotation matrices for any rotation, about an arbitrary angle α, are as follows:

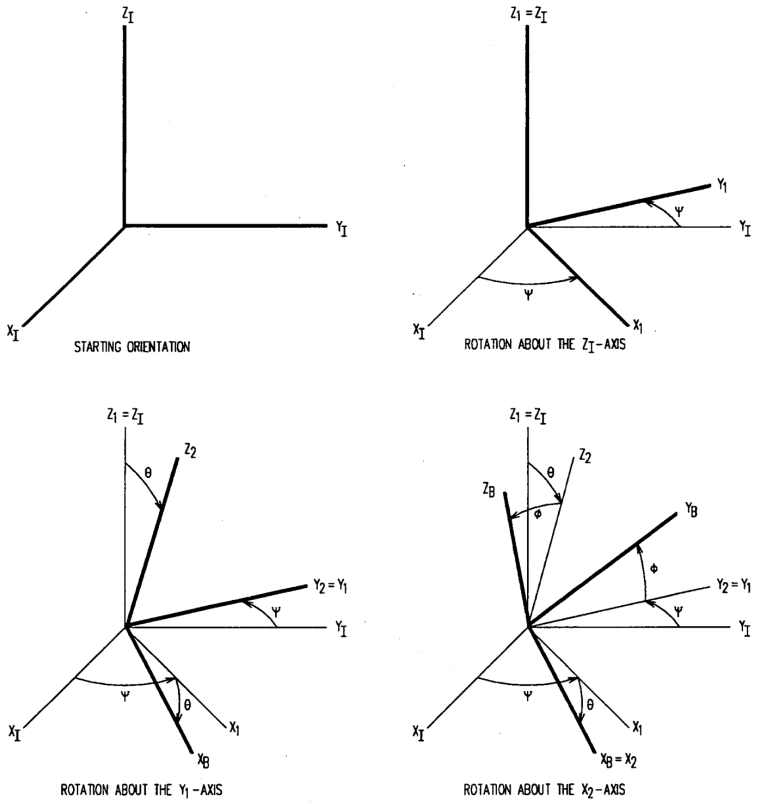

Figure 4.7: The Euler angle transformation about the Z, Y and the X axis to go from the inertial (I to body (B) frame (Mooij, 1994).

Table 4.1: Standard frame transformations used in aerospace dynamics (Mooij, 1994).

From	To	Transformation Matrix	Involved Variables
R	I	$\mathbf{C_{I,R}} = C_3(-\omega_{cb}t)$	ω_{cb} = central body rotation rate, t = time from epoch
I	Bp	$\mathbf{C_{I,Bp}}$	Parafoil Quaternions
V	R	$\mathbf{C_{R,V}} = C_3(-\tau)C_2\left(\frac{\pi}{2}+\delta\right)$	τ = moon-centric longitude, δ = moon-centric latitude
W	V	$\mathbf{C_{V,W}} = C_3(-\chi_W)C_2(-\gamma_W)$	γ_W = flight path angle w.r.t. wind vector, χ_W = heading angle w.r.t. wind vector
TA	V	$\mathbf{C_{V,TA}} = C_3(-\chi_A)C_2(-\gamma_A)$	γ_A = flight path angle w.r.t. airspeed vector, χ_A = heading angle w.r.t. airspeed vector
A	TA	$\mathbf{C_{TA,A}} = C_1(\sigma_A)$	σ_A = bank angle w.r.t. airspeed vector
B	A	$\mathbf{C_{A,B}} = C_3(\beta_A)C_2(-\alpha_A)$	β_A = sideslip angle w.r.t. airspeed vector, α_A = angle of attack w.r.t. airspeed vector

$$\mathbf{C_x}(\alpha) = \begin{bmatrix} 1 & 0 & 0 \\ 0 & \cos\alpha & \sin\alpha \\ 0 & -\sin\alpha & \cos\alpha \end{bmatrix} \tag{4.2}$$

$$\mathbf{C_y}(\alpha) = \begin{bmatrix} \cos\alpha & 0 & -\sin\alpha \\ 0 & 1 & 0 \\ \sin\alpha & 0 & \cos\alpha \end{bmatrix} \tag{4.3}$$

$$\mathbf{C_z}(\alpha) = \begin{bmatrix} \cos\alpha & \sin\alpha & 0 \\ -\sin\alpha & \cos\alpha & 0 \\ 0 & 0 & 1 \end{bmatrix} \tag{4.4}$$

The subscripts x, y, and z represent rotations around the X, Y, and Z axes respectively. A complete transformation can be expressed as the product of these orthonormal unit rotation matrices $\mathbf{C_x}$, $\mathbf{C_y}$, and $\mathbf{C_z}$. The resulting matrix is also orthonormal, and its inverse is simply its transpose.
When considering two reference frames, A and B, the rotation from frame A to frame B can be broken down into sequential unit axis transformations. The transformation, composed of three successive rotations about the negative X-axis, Z-axis, and positive Y-axis, is represented by the matrix $\mathbf{C_{B,A}}$:

$$\mathbf{C_{B,A}} = \mathbf{C_y}(\alpha_y)\mathbf{C_z}(-\alpha_z)\mathbf{C_x}(-\alpha_x) \tag{4.5}$$

This implies that the transformation is defined from frame A to frame B. The inverse of this matrix is obtained by reversing the order of the rotations and negating the angles:

$$\mathbf{C_{A,B}} = \mathbf{C_{B,A}}^{-1} = \mathbf{C_{B,A}}^{T} = \mathbf{C_x}(\alpha_x)\mathbf{C_z}(\alpha_z)\mathbf{C_y}(-\alpha_y) \tag{4.6}$$

The representation of Euler angles is minimal in that it involves the least number of parameters necessary to describe the orientation of a rigid body. However, singularities might occur during the inversion process of the transformation matrix (i.e., when computing Euler angles from a given rotation matrix), which can lead to a loss of kinematic resolution. This phenomenon, known as gimbal lock, occurs when two of the three rotational axes become aligned, effectively reducing the degrees of freedom for rotational motion. In the commonly used 2-3-1 sequence of Euler angles, gimbal lock occurs specifically at a $\pm 90°$ rotation of the second angle (pitch). At this configuration, the system loses the ability to distinguish between rotations about the first and third axes, making certain manoeuvres kinematically unresolved.

4.3.2. Spherical to Cartesian state conversion

Relating position elements of spherical and Cartesian coordinates is relatively straightforward. However, the derivations are omitted here, and only the final results are presented.

Position elements

The fundamental equations that link spherical coordinates to Cartesian coordinates within the R-frame are given by:

$$r = \sqrt{x_R^2 + y_R^2 + z_R^2} \tag{4.7}$$

$$\tau = \arctan\left(\frac{y_R}{x_R}\right) \tag{4.8}$$

$$\delta = \arcsin\left(\frac{z_R}{\sqrt{x_R^2 + y_R^2 + z_R^2}}\right) \tag{4.9}$$

The inverse transformations are also valid:

$$x_R = r\cos\delta\cos\tau \tag{4.10}$$

$$y_R = r\cos\delta\sin\tau \tag{4.11}$$

$$z_R = r\sin\delta \tag{4.12}$$

Velocity elements

The Cartesian velocity components are related to spherical velocity components as follows:

$$v_x = V_G\cos\gamma\cos\chi_G \tag{4.13}$$

$$v_y = V_G\cos\gamma\sin\chi_G \tag{4.14}$$

$$v_z = -V_G\sin\gamma \tag{4.15}$$

These expressions determine the Cartesian velocity components in the vertical frame. When considering a planet-centred rotating frame, the components can be deduced by applying the appropriate transformations. Excluding wind effects, the groundspeed is computed by:

$$V_G = \sqrt{v_u^2 + v_v^2 + v_w^2} \tag{4.16}$$

The two relevant spherical velocity elements are then found by:

$$\chi_G = \arctan\left(\frac{v_y}{v_x}\right), \quad \gamma_G = \arcsin\left(\frac{v_z}{\sqrt{v_x^2 + v_y^2}}\right) \tag{4.17}$$

The governing wind equations will be based on Cartesian components in the research to maintain logical overlap with previously defined external forces. The final section of this chapter outlines wind considerations. The scheme for computing airspeed-based velocity components is as follows (Mooij, 1994 and Mazouz et al., 2021):

1. Obtain the available wind parameters.
2. Apply a transformation to these parameters if they are not provided in Cartesian components w.r.t. the V-frame.
3. Compute the airspeed based velocity V_A including velocity angles.
4. Compute the airspeed based angle of attack α_A and sideslip angle β_A and bank angle w.r.t. the airspeed for both the store and the parafoil.
5. If aerodynamic coefficients are not defined with respect to a point coinciding with the CoM of the vehicle, a linear velocity is added to account for rotation.
6. Compute the airspeed based aerodynamic force coefficients C_D, C_S and C_L.
7. Compute the airspeed based aerodynamic forces and moments.
8. Evaluate the equations of motion.
9. Update the state vector.

The groundspeed is defined as the sum of the airspeed and the atmospheric velocity relative to the ground:

$$\mathbf{V_{B,G}} = \mathbf{V_{B,A}} + \mathbf{V_{A,G}} \tag{4.18}$$

The wind velocity vector is expressed in the rotating frame as:

$$\mathbf{V_{W,R}} = \begin{pmatrix} \mathbf{u_W} \\ \mathbf{v_W} \\ \mathbf{w_W} \end{pmatrix}^T \tag{4.19}$$

Combining the expressions of Eq. (3.29) and (3.30) yields the decomposition of the groundspeed such that:

$$\mathbf{V_{B,R}} = \mathbf{V_{B,W}} + \mathbf{V_{W,R}} \tag{4.20}$$

Indicating the velocity relative to the atmosphere with subscript A and rewriting the above equation provides the following set of equations:

$$\mathbf{V_{B,W}} = \mathbf{V_{B,R}} - \mathbf{V_{W,R}} = \begin{pmatrix} u_A \\ v_A \\ w_A \end{pmatrix}^T \quad \text{and} \quad \mathbf{V_A} = \sqrt{\mathbf{u_A}^2 + \mathbf{v_A}^2 + \mathbf{w_A}^2} \tag{4.21}$$

The airspeed based angle of attack and sideslip angle follow from the body-frame velocity components:

$$\alpha_A = \arctan\left(\frac{w_A}{u_A}\right) \tag{4.22}$$

$$\beta_A = \arctan\left(\frac{v_A}{\sqrt{u_A^2 + w_A^2}}\right) \tag{4.23}$$

4.3.3. Conversion Between Euler Angles and Quaternions

Conversion between the classical Euler angles and quaternions, which are also referred to as Euler parameters, is detailed herein. Final forms of transformation are presented, devoid of the derivational process.

From Euler Angles to Quaternions

When converting from Euler angles to quaternions, the sequence of rotations is crucial. Here, the 3-2-1 sequence is utilized, while alternative sequences would reverse the order. The quaternion q is derived as follows:

$$\begin{pmatrix} q_1 \\ q_2 \\ q_3 \\ q_4 \end{pmatrix} = \begin{bmatrix} \cos\frac{\phi}{2}\cos\frac{\theta}{2}\cos\frac{\psi}{2} + \sin\frac{\phi}{2}\sin\frac{\theta}{2}\sin\frac{\psi}{2} \\ \sin\frac{\phi}{2}\cos\frac{\theta}{2}\cos\frac{\psi}{2} - \cos\frac{\phi}{2}\sin\frac{\theta}{2}\sin\frac{\psi}{2} \\ \cos\frac{\phi}{2}\sin\frac{\theta}{2}\cos\frac{\psi}{2} + \sin\frac{\phi}{2}\cos\frac{\theta}{2}\sin\frac{\psi}{2} \\ \cos\frac{\phi}{2}\cos\frac{\theta}{2}\sin\frac{\psi}{2} - \sin\frac{\phi}{2}\sin\frac{\theta}{2}\cos\frac{\psi}{2} \end{bmatrix}$$

From Quaternions to Euler Angles

Conversely, the Euler angles can be extracted from the quaternions by applying the inverse transformation (derived based on equations from Mooij (1992)):

$$\begin{pmatrix} \phi \\ \theta \\ \psi \end{pmatrix} = \begin{bmatrix} \text{atan2}\left(2\left(q_0 q_1 + q_2 q_3\right), 1 - 2\left(q_1^2 + q_2^2\right)\right) \\ \text{asin}\left(2\left(q_0 q_2 - q_1 q_3\right)\right) \\ \text{atan2}\left(2\left(q_0 q_3 + q_1 q_2\right), 1 - 2\left(q_2^2 + q_3^2\right)\right) \end{bmatrix}$$

4.4. 6DOF Equations of Motion

The 6DOF model represents parachute-capsule system dynamics, providing a baseline for examining aerodynamic and gravitational interactions in a simpler system before progressing to the 9DOF parafoil model. Thus, only the 6DOF equations of motion are introduced in this section. Using Newton-Euler methods, the equations account for both translational and rotational dynamics. Translational dynamics stem from aerodynamic and gravitational forces, while rotational dynamics are due to moments acting on the CoM.

4.4.1. The Equations of Translational Motion

The equations of translational motion describe the accelerations of the system's centre of mass as a result of external forces acting on the system. The translational accelerations are derived from the total forces divided by the total mass of the system, resulting in three components of translational acceleration:

$$\ddot{\mathbf{r}} = \frac{\mathbf{F}_{\text{total}}}{m} \tag{4.24}$$

where

- $\mathbf{F}_{\text{total}} = \begin{bmatrix} F_x & F_y & F_z \end{bmatrix}^T$ represents the sum of all external forces acting on the system, expressed in components along the body axes.
- m is the total mass of the parachute/payload system.
- $\ddot{\mathbf{r}} = \begin{pmatrix} \ddot{x} & \ddot{y} & \ddot{z} \end{pmatrix}^T$ represents the translational accelerations along the body axes.

The components of translational acceleration can therefore be expressed as:

$$\ddot{x} = \frac{F_x}{m} \tag{4.25}$$

$$\ddot{y} = \frac{F_y}{m} \tag{4.26}$$

$$\ddot{z} = \frac{F_z}{m} \tag{4.27}$$

Total force on the system is:

$$\mathbf{F} = \mathbf{F}_{\text{aero}} + \mathbf{F}_{\text{grav}} + \mathbf{F}_{\text{added mass}} \tag{4.28}$$

Where:

- $\mathbf{F}_{\text{aero}}$: Aerodynamic forces,
- $\mathbf{F}_{\text{grav}}$: Gravitational forces,
- $\mathbf{F}_{\text{added mass}}$: Added mass from parachute.

4.4.2. The Equations of Rotational Motion

The dynamic equations of rotational motion, known as the Euler equations, provide insights into the angular accelerations of the system. The full set of non-linear equations is represented as:

$$\dot{\omega} = \mathbf{I}^{-1} \left(\mathbf{M}_B - \omega \times \mathbf{I}\omega \right) \tag{4.29}$$

where

- $\mathbf{M}_B = \begin{bmatrix} M_x & M_y & M_z \end{bmatrix}^T$ represents the sum of external moments about the global centre of mass (CoM), expressed in components along the body axes.

- $\mathbf{I} = \begin{bmatrix} I_{xx} & -I_{xy} & -I_{xz} \\ -I_{xy} & I_{yy} & -I_{yz} \\ -I_{xz} & -I_{yz} & I_{zz} \end{bmatrix}$ is the inertia tensor of the parachute/payload system, referenced to the body frame.
- $\omega = \begin{bmatrix} p & q & r \end{bmatrix}^T$ is the rotation vector of the body frame with respect to the inertial frame, expressed in components along the body axes.

Simplified expressions for the equations of motion can be obtained under the assumption of rotational symmetry, i.e., with two planes of symmetry. In this case, all products of inertia are zero, and Equation (4.29) simplifies to:

$$\dot{p} = \frac{M_x}{I_{xx}} + \frac{I_{yy} - I_{zz}}{I_{xx}} qr \tag{4.30}$$

$$\dot{q} = \frac{M_y}{I_{yy}} + \frac{I_{zz} - I_{xx}}{I_{yy}} pr \tag{4.31}$$

$$\dot{r} = \frac{M_z}{I_{zz}} + \frac{I_{xx} - I_{yy}}{I_{zz}} pq \tag{4.32}$$

Moments on the system include aerodynamic, gravitational, added mass, and swivel effects:

$$\mathbf{M} = \mathbf{M}_{\text{aero}} + \mathbf{M}_{\text{grav}} + \mathbf{M}_{\text{added mass}} \tag{4.33}$$

Where:

- $\mathbf{M}_{\text{aero}}$: Aerodynamic moment,
- $\mathbf{M}_{\text{grav}}$: Gravitational moment,
- $\mathbf{M}_{\text{added mass}}$: Moment due to added mass inertial effects, which arise from the resistance of the fluid surrounding the parafoil as it undergoes angular motion

4.4.3. Frame Simplification for the Actual Parafoil System

While the frame definitions and transformations presented in Table 4.1 provide a comprehensive theoretical basis, not all these frames are necessary for the final parafoil analysis. Under the specific conditions and reference states examined in this work, the trajectory-based frames (TG, AG, and AA) effectively overlap to form a single simplified reference frame, hereafter referred to as the **A-frame**. This consolidation streamlines the analysis by allowing aerodynamic angles to be expressed using a unified set of variables α, β, and σ, without the additional complexity of multiple, nearly identical frames.

It is important to recognize that while the simplified A-frame is conceptually cleaner, the underlying methods are fully capable of handling different frame definitions and orientations. In fact, an earlier stage of this project involved a parachute model whose body and aerodynamic frames were oriented differently from those of the parafoil. Specifically, the parachute's body and aerodynamic frames were defined such that the x-axis pointed downwards and the z-axis pointed to the left, making the angle of attack α effectively the angular difference between two downward axes. In contrast, the parafoil's frames place the x-axis pointing forward (to the right) and the z-axis pointing downward, resulting in a 90-degree rotational difference in how α is measured. For the parafoil, α remains an angle between the x-axis of the body frame and the corresponding x-axis of the aerodynamic frame, but its interpretation shifts due to the reoriented axes.

These differences in frame orientation do not compromise the consistency or accuracy of the analysis. The geometry parameters (e.g., position vectors) and the frame transformation matrices are defined precisely to handle such configuration changes. Whether the main aerodynamic axis points down or forward, the core mathematics of frame transformations remains valid. As a result, the multi-frame framework provides a robust and flexible foundation: it easily accommodates differing

reference frame conventions and ensures that all forces, moments, and derived aerodynamic angles are correctly represented.
In summary, the decision to collapse TG, AG, and AA into a single A-frame is a practical measure that simplifies the notation and reduces overhead without losing any physical insight. The underlying principles and transformation methods remain general enough to accommodate varying frame orientations—such as those used for the earlier parachute model—and continue to deliver consistent, meaningful results for the parafoil configuration in this thesis.

4.5. Geometry and Mass

Since the 6DOF system is initial created with a simpler parachute model (rather than parafoil) to understand and very it better, Mooij (1992) is consulted and used for the geometry and flight dynamics for the 6DOF parachute-capsule system (modelled for the Huygens mission). The general geometrical layout of the parachute system is depicted in Figure 4.8. The system is assumed to be an axisymmetric body (also called a rotational symmetric body), with the centre of mass (CoM) of the parachute and the payload located on the axis of symmetry. As a result, both the parachute and the payload (from now on called the re-entry vehicle) must be axisymmetric.
The parachute has a fixed-shape canopy with rigid suspension lines and is assumed to have a conical ribbon canopy. The geometry and mass properties of the parachute have been taken from Ibrahim and Engdahl (1974). The geometry of the parachute and riser is shown in Figure 4.10, while typical dimensions of the fully inflated conical ribbon canopy shape are given in Figure 4.11.
In these figures, the following notations have been used:

- m_c = mass of the canopy (kg)
- m_l = mass of the suspension lines (kg)
- R_0 = nominal radius of the inflated mouth of the canopy (m)

The following relationships for the parachute geometry are used:

$$R_0 = 0.36 D_0 \tag{4.34}$$

$$S_{p,\text{ref}} = \frac{\pi}{4}(0.72 D_0)^2 \tag{4.35}$$

$$L_{cp} = 0.163 D_0 \tag{4.36}$$

The suspension line angle γ and the projected distance AL_{cm} of the suspension lines are given by:

$$\gamma = \arcsin\left(\frac{R_0}{L_s}\right) \tag{4.37}$$

$$AL_{cm} = L_s \cos\gamma = \sqrt{R_0^2 + L_s^2} \tag{4.38}$$

The length L_1 between the CoP and the convergence point of suspension lines is:

$$L_1 = L_{cp} + AL_{cm} \tag{4.39}$$

The CoM location for the entire canopy, including the added mass m_a (the mass under the canopy which is accelerated/decelerated by the motion of the system), is given by:

$$L_{cm} = \frac{AL_{cm} m_l/2 + L_1(m_c + m_a)}{m_l + m_c + m_a} \tag{4.40}$$

where

- m_a = added mass (kg) = $V_c \rho$

- V_c = volume of canopy (m^3)
- ρ = atmospheric density (kg/m^3)

The volume of the canopy is:

$$V_c = \frac{2}{3}\pi(0.325D_0)(0.36D_0)^2 \tag{4.41}$$

The moments of inertia of the parachute about the parachute CoM are given by:

$$I_{xx_p} = \frac{m_l L_s^2 \sin^2\gamma}{12} + \frac{2}{3}m_c(0.36D_0)^2 + 0.063\rho(R_0)^5 \tag{4.42}$$

$$I_{yy_p} = I_{zz_p} = \frac{m_l L_s^2 \cos^2\gamma}{12} + m_c\left(L_{cm} - \frac{AL_{cm}}{2}\right)^2 + \frac{m_c}{3}(0.325^2 + 0.36^2)D_0^2 \tag{4.43}$$

$$+ m_a(AL_{cm} - L_{cm})^2 + 0.042\rho(R_0)^5 + m_a(L_1 - L_{cm})^2 \tag{4.44}$$

The inertia tensor of the re-entry vehicle (payload) with respect to the local CoM of the re-entry vehicle is:

$$\mathbf{I} = \begin{bmatrix} I_{xx_r} & 0 & 0 \\ 0 & I_{yy_r} & 0 \\ 0 & 0 & I_{zz_r} \end{bmatrix} \tag{4.45}$$

The total inertia tensor, including all parachutes and the re-entry vehicle, is computed by determining the location of the global CoM. The total moments of inertia are given by:

$$I_{xx_{\text{tot}}} = I_{xx_r} + n_p I_{xx_p} \tag{4.46}$$

$$I_{yy_{\text{tot}}} = I_{yy_r} + n_p I_{yy_p} + I_{\text{shift}} \tag{4.47}$$

$$I_{zz_{\text{tot}}} = I_{zz_r} + n_p I_{zz_p} + I_{\text{shift}} \tag{4.48}$$

where I_{shift} is computed using Steiner's rule:

$$I_{\text{shift}} = n_p(m_c + m_l + m_a)L_{p,cm}^2 + m_r L_{r,cm}^2 \tag{4.49}$$

Refer to Figure 4.9 for the relation between the CoM of the re-entry vehicle and the attachment point.

4.6. External Forces and Moments

The external forces and moments acting on the parachute and capsule result from aerodynamic and gravitational origins. These forces and moments are crucial in shaping the descent trajectory of the system. Additionally, moments due to offsets in the aerodynamic force application points relative to the centres of mass are also considered.

4.6.1. Aerodynamic Forces

The aerodynamic forces acting on the parachute (F_{Ap}) and the capsule (F_{Ar}) are defined in the aerodynamic reference frame (index A) as:

$$\mathbf{F_{Ap,A}} = \begin{pmatrix} -D_p \\ -S_p \\ -L_p \end{pmatrix} \tag{4.50}$$

$$\mathbf{F_{Ar,A}} = \begin{pmatrix} -D_r \\ -S_r \\ -L_r \end{pmatrix}, \tag{4.51}$$

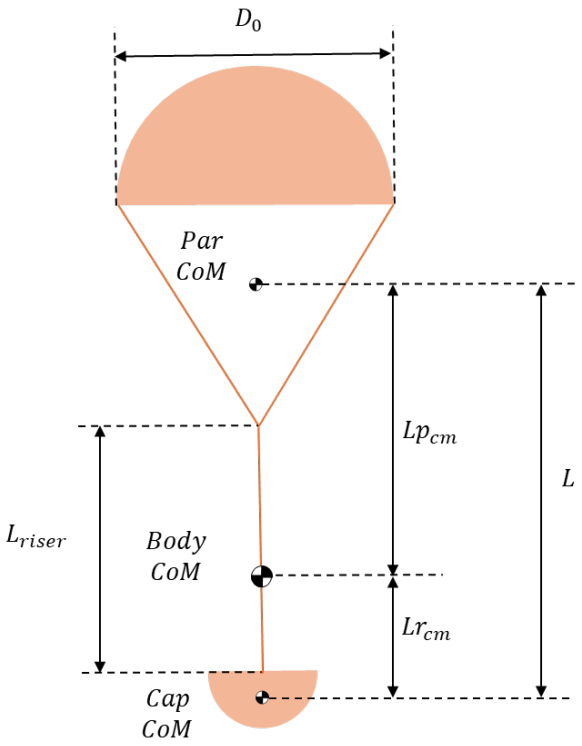

Figure 4.8: The general geometry of the parachute system.

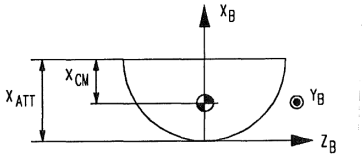

Figure 4.9: The relation between the CoM of the re-entry vehicle and the attachment point. (Mooij, 1992)

where D, S, and L represent the drag, side force, and lift components, respectively. These are given with respect to a reference point and are positive in their respective directions.
To express these forces in the rotational reference frame (R), the transformation is applied as:

$$\mathbf{F_{Ap,R}} = \mathbf{C_{R,A}}\mathbf{F_{Ap,A}}, \quad \mathbf{F_{Ar,R}} = \mathbf{C_{R,A}}\mathbf{F_{Ar,A}}, \tag{4.52}$$

where $C_{R,A}$ is the transformation matrix from the aerodynamic frame to the rotational frame.

4.6.2. Gravitational Forces

The gravitational forces are expressed in the rotational reference frame as:

$$\mathbf{F_{Gp,R}} = (m_c + m_l)\mathbf{g_R} \tag{4.53}$$

$$\mathbf{F_{Gr,R}} = m_r \mathbf{g_R} \tag{4.54}$$

where m_c, m_l, and m_r are the masses of the parachute, connecting lines, and capsule, respectively. The vector g_R is the gravitational acceleration in the rotational frame.

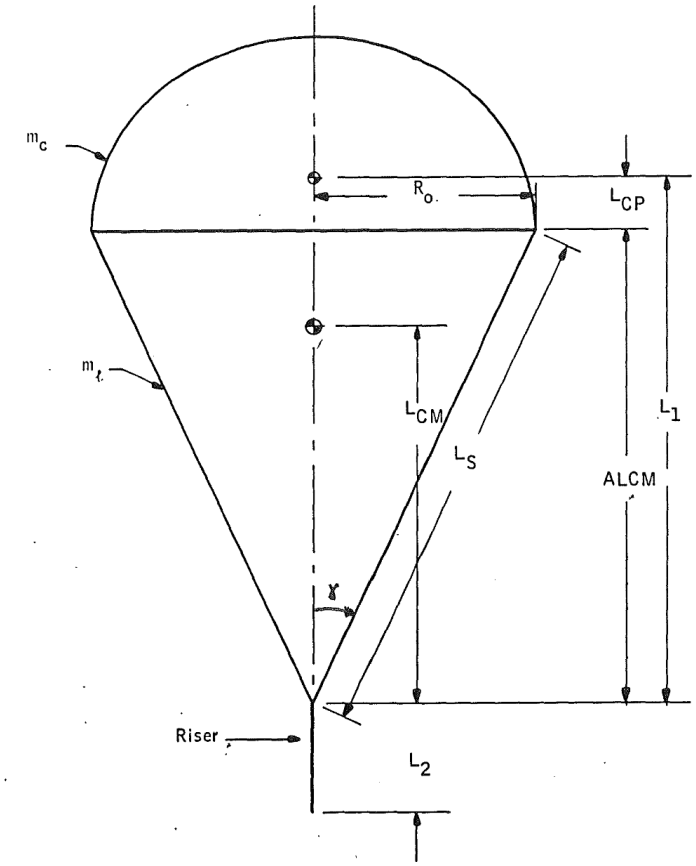

Figure 4.10: Parachute and riser geometry (Ibrahim and Engdahl, 1974).

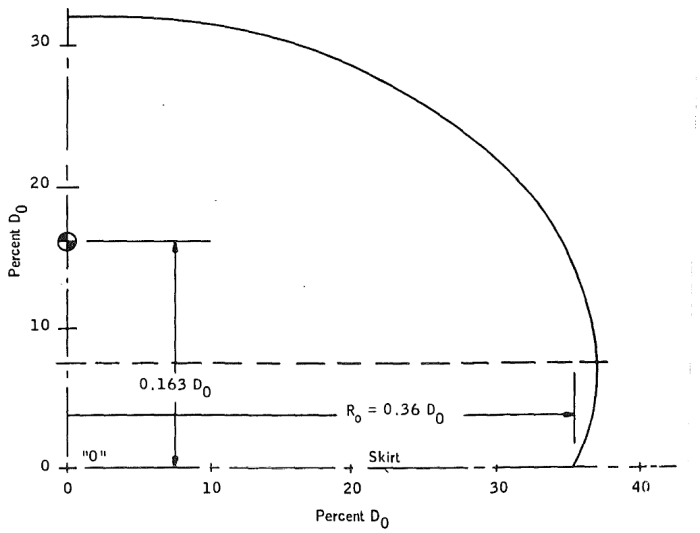

Figure 4.11: Fully inflated conical ribbon canopy shape (Ibrahim and Engdahl, 1974).

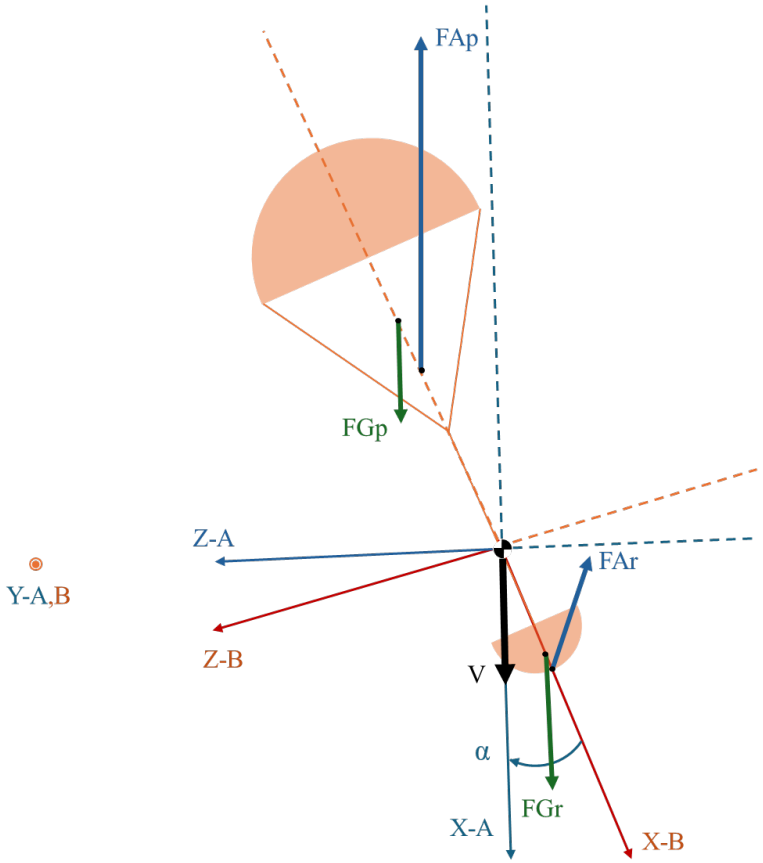

Figure 4.12: External forces acting on the system.

4.6.3. Aerodynamic Moments

The aerodynamic moments for the parachute and capsule are defined in the body frame (index B) with respect to the aerodynamic reference point. These moments are given as:

$$\mathbf{M_{Ap,B}} = \begin{pmatrix} L_p \\ M_p \\ N_p \end{pmatrix} \tag{4.55}$$

$$\mathbf{M_{Ar,B}} = \begin{pmatrix} L_r \\ M_r \\ N_r \end{pmatrix} \tag{4.56}$$

where L, M, and N represent the rolling, pitching, and yawing moments, respectively.
When the aerodynamic reference point does not coincide with the global centre of mass, an additional moment arises due to force offsets. This moment is expressed as:

$$\Delta\mathbf{M_{A,B}} = \mathbf{r_{p,B}} \times \mathbf{F_{Ap,B}} + \mathbf{r_{r,B}} \times \mathbf{F_{Ar,B}} \tag{4.57}$$

where:

$$\mathbf{r_{p,B}} = \begin{pmatrix} L_{p,cm} \\ 0 \\ 0 \end{pmatrix}, \quad L_{p,cm} > 0 \tag{4.58}$$

$$\mathbf{r_{r,B}} = \begin{pmatrix} -L_{r,cm} \\ 0 \\ 0 \end{pmatrix}, \quad L_{r,cm} > 0 \tag{4.59}$$

are the position vectors of the aerodynamic force application points relative to the centres of mass.

4.6.4. Summary of Forces and Moments

The total force vector in the rotational frame is:

$$\mathbf{F_R} = \mathbf{F_{Ap,R}} + \mathbf{F_{Ar,R}} + \mathbf{F_{Gp,R}} + \mathbf{F_{Gr,R}}, \tag{4.60}$$

and the total moment vector in the body frame is:

$$\mathbf{M_B} = \mathbf{M_{Ap,B}} + \mathbf{M_{Ar,B}} + \mathbf{M_{Gp,B}} + \mathbf{M_{Gr,B}} + \Delta\mathbf{M_{A,B}} \tag{4.61}$$

4.6.5. Aerodynamic Coefficients

The aerodynamic forces and moments depend on the aerodynamic coefficients. For instance, the lift force is given as:

$$L = C_L \overline{q} S_{\text{ref}} \tag{4.62}$$

where:

$$\overline{q} = \frac{1}{2}\rho V^2 \tag{4.63}$$

and C_L is the lift coefficient, which is computed as:

$$C_L = C_{L_0} + C_{L_\alpha}\alpha \tag{4.64}$$

Here, α is the angle of attack, and C_{L_α} is the lift gradient.
This framework ensures accurate modelling of forces and moments for the parachute-capsule system, accounting for aerodynamic, gravitational, and coupling effects.

Aerodynamic properties

The aerodynamic forces and moments in this study are computed using validated aerodynamic coefficients sourced from Mooij (1992). These coefficients include lift (C_L), drag (C_D), moment (C_m), normal force (C_N), and side force (C_S) coefficients. They were used to characterize the aerodynamic behaviour of the parafoil-capsule system across a range of angles of attack (α), sideslip angles (β), and Mach numbers.
For verification purposes during the development of the 6DOF parachute model, the relationships between these coefficients and aerodynamic parameters were plotted and analysed. These plots, which provide a comprehensive overview of the aerodynamic properties, are included in Appendix A (Figures A.1 to A.5). They demonstrate the variations in aerodynamic forces and moments under different flow conditions and form the basis for the aerodynamic modelling used throughout this study.

5

9DOF Model

In this chapter, we extend the parafoil-capsule system to a 9-degree-of-freedom (9DOF) model, incorporating both the parafoil and payload as individual rigid bodies connected by a hinge. The model captures the translational and rotational dynamics of each body, considering aerodynamic, gravitational, and hinge-related forces. This detailed modelling approach provides a comprehensive understanding of the parafoil-payload dynamics in preparation for descent simulations on planetary bodies like Titan. Multiple 9DOF Parafoil systems were consolidated and in the end, a combination of Prakash and Ananthkrishnan (2006), Slegers and Costello (2003) and Mooij et al. (2003) was used.

5.1. Equations of Motion

The equations of motion for the 9DOF parafoil-payload system are developed to capture both the translational and rotational behaviour. These equations are divided into dynamics, which include forces and moments acting on the system, and kinematics, which describe the positional and angular relationships.
The translational and rotational dynamics are represented through matrix and vector formulations, where each point of interest (e.g., parafoil centre of mass, payload centre of mass, and hinge connection point) is described by its respective force and moment interactions.

Positions

The position vectors of key points on the parafoil system can be expressed as follows (see also Figure 5.1):

$$\mathbf{r}_p = \begin{pmatrix} x_p \\ y_p \\ z_p \end{pmatrix} = \begin{pmatrix} -R_p \sin(\mu) \\ 0 \\ -R_p \cos(\mu) \end{pmatrix} \tag{5.1}$$

Here, $\mathbf{R}_{cp}$ is the position vector from point $HingeC$ (e.g., hinge point) to point $ParC$ (e.g., parafoil centre of mass), with R_p denoting the physical distance and μ the rigging angle.
Similarly, the position vector from point $HingeC$ to point $CapC$ (e.g., payload centre of mass) is given by:

$$\mathbf{r}_r = \begin{pmatrix} x_r \\ y_r \\ z_r \end{pmatrix} = \begin{pmatrix} 0 \\ 0 \\ R_r \end{pmatrix} \tag{5.2}$$

In this case, R_r represents the physical distance from the hinge point $HingeC$ to the payload mass centre $CapC$.

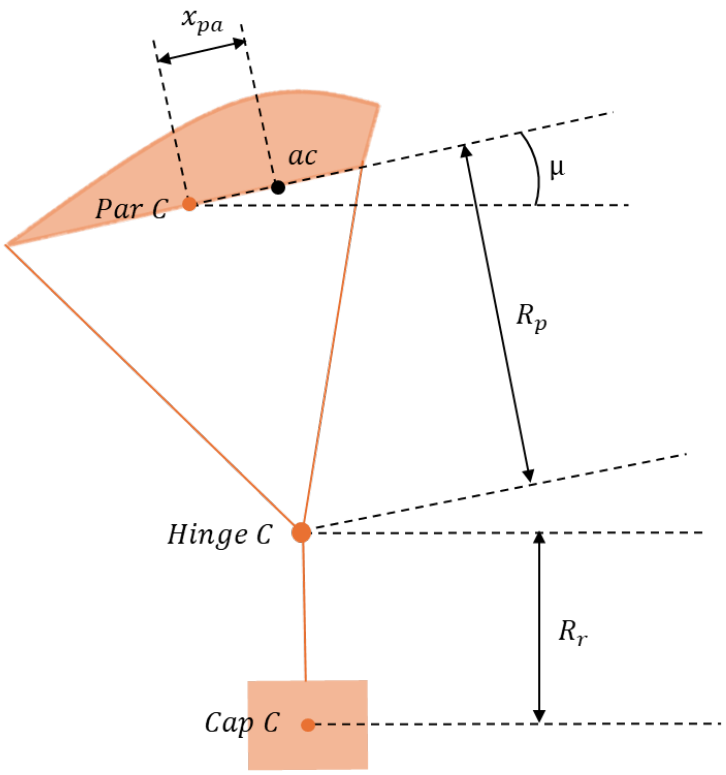

Figure 5.1: General geometry of the 9DOF parafoil system.

These vector definitions establish the geometric relationships necessary for formulating the system's equations of motion.

$$\boldsymbol{S}_{\boldsymbol{r}_p} = \begin{bmatrix} 0 & -z_p & y_p \\ z_p & 0 & -x_p \\ -y_p & x_p & 0 \end{bmatrix} \tag{5.3}$$

$$\boldsymbol{S}_{\boldsymbol{r}_r} = \begin{bmatrix} 0 & -z_r & y_r \\ z_r & 0 & -x_r \\ -y_r & x_r & 0 \end{bmatrix} \tag{5.4}$$

These skew-symmetric matrices represent cross products for calculating moments based on the distances $\boldsymbol{r}_p$ and $\boldsymbol{r}_r$ between the hinge (C) and points p (parafoil) and r (payload), respectively.

Rotational Velocities and Angular Rates

The angular velocities $\boldsymbol{\omega}_p$ and $\boldsymbol{\omega}_r$ of the parafoil and payload are defined as follows:

$$\boldsymbol{\omega_p} = \begin{pmatrix} p_p \\ q_p \\ r_p \end{pmatrix}, \quad \boldsymbol{\omega_r} = \begin{pmatrix} p_r \\ q_r \\ r_r \end{pmatrix} \tag{5.5}$$

The corresponding skew-symmetric matrices $\boldsymbol{\Omega}_p$ and $\boldsymbol{\Omega}_r$ capture the rotation rates used in calculating relative rotational effects:

$$\boldsymbol{\Omega_P} = \begin{bmatrix} 0 & -r_p & q_p \\ r_p & 0 & -p_p \\ -q_p & p_p & 0 \end{bmatrix}, \quad \boldsymbol{\Omega_r} = \begin{bmatrix} 0 & -r_r & q_r \\ r_r & 0 & -p_r \\ -q_r & p_r & 0 \end{bmatrix} \tag{5.6}$$

Inertia and Mass Matrices

The inertia matrices for the payload $\boldsymbol{I}_r$ and the parafoil $\boldsymbol{I}_p$ characterize each body's resistance to rotational acceleration:

$$\boldsymbol{I_r} = \frac{m_r}{12}\begin{bmatrix} W^2+H^2 & 0 & 0 \\ 0 & D^2+H^2 & 0 \\ 0 & 0 & D^2+W^2 \end{bmatrix}, \quad \boldsymbol{I_P} = \begin{bmatrix} I_{xx} & 0 & I_{xz} \\ 0 & I_{yy} & 0 \\ I_{zx} & 0 & I_{zz} \end{bmatrix} \tag{5.7}$$

The mass matrices $\boldsymbol{M}_r$ and $\boldsymbol{M}_p$ account for each body's mass and added mass effects due to the surrounding fluid (if applicable).

$$\boldsymbol{M_r} = m_r \boldsymbol{I}_{3\times3}, \quad \boldsymbol{M_P} = (m_p + m_{\text{added}})\boldsymbol{I}_{3\times3} \tag{5.8}$$

Hinge Moment Model

The hinge between the parafoil and payload introduces moments based on angular displacement and angular velocity differences between the two bodies. This hinge behaves as a 3D spring-damper system, where stiffness and damping coefficients along each rotational axis provide restoring and resistive moments, respectively. This hinge was modelled after the 9DOF parafoil created in a different article (Mooij et al., 2003).

$$\mathbf{M_H} = \begin{bmatrix} K_\phi & 0 & 0 \\ 0 & K_\theta & 0 \\ 0 & 0 & K_\psi \end{bmatrix}\begin{pmatrix} \Delta\phi \\ \Delta\theta \\ \Delta\psi \end{pmatrix} - \begin{bmatrix} c_\phi & 0 & 0 \\ 0 & c_\theta & 0 \\ 0 & 0 & c_\psi \end{bmatrix}\begin{pmatrix} \Delta\dot{\phi} \\ \Delta\dot{\theta} \\ \Delta\dot{\psi} \end{pmatrix} \tag{5.9}$$

where $\Delta\phi$, $\Delta\theta$, and $\Delta\psi$ represent the angular displacements between the parafoil and payload, and $\Delta\dot{\phi}$, $\Delta\dot{\theta}$, $\Delta\dot{\psi}$ are their respective rates. This model simulates the resistance offered by the hinge connection to relative rotations.

Kinematics of the Parafoil and Payload

To complete the equations of motion, we include kinematic equations that describe the translational and rotational movement of the parafoil and payload relative to the inertial frame. These relationships enable the computation of changes in position and orientation over time.

$$\begin{bmatrix} -M_r S_{r_{Cr}} & 0_{3\times3} & M_r T_r & T_r \\ 0_{3\times3} & -(M_p+M_F)S_{r_{Cp}} & (M_p+M_F)T_p & -T_p \\ I_r & 0_{3\times3} & 0_{3\times3} & -S_{r_{Cr}} T_r \\ 0_{3\times3} & I_p + I_F & 0_{3\times3} & S_{r_{Cp}} T_p \end{bmatrix}\begin{pmatrix} \dot{\omega}_r \\ \dot{\omega}_p \\ \dot{V}_C \\ F_C \end{pmatrix} = \begin{pmatrix} B_1 \\ B_2 \\ B_3 \\ B_4 \end{pmatrix} \tag{5.10}$$

The B vectors are defined as follows:

$$B_1 = \boldsymbol{F}_{a_p} + \boldsymbol{F}_{g_p} + \boldsymbol{F}_{b_p} - \boldsymbol{\Omega}_P(M_p+M_F)\boldsymbol{\Omega}_r S_{r_{Cp}}\boldsymbol{V}_C, \tag{5.11}$$

$$B_2 = \boldsymbol{F}_{a_r} + \boldsymbol{F}_{g_r} - \boldsymbol{\Omega}_r M_r \boldsymbol{\Omega}_r S_{r_{Cr}}, \tag{5.12}$$

$$B_3 = \boldsymbol{M}_{g_r} - \boldsymbol{\Omega}_r I_r \boldsymbol{\omega}_r, \tag{5.13}$$

$$B_4 = \boldsymbol{M}_{a_p} + \boldsymbol{M}_{g_p} + \boldsymbol{M}_{b_p} - \boldsymbol{\Omega}_p I_p \boldsymbol{\omega}_p, \tag{5.14}$$

where:

- $\boldsymbol{F}_{a_p}, \boldsymbol{F}_{a_r}$: aerodynamic forces on the parafoil and capsule,
- $\boldsymbol{F}_{g_p}, \boldsymbol{F}_{g_r}$: gravitational forces on the parafoil and capsule,
- $\boldsymbol{F}_{b_p}$: buoyancy force on the parafoil,
- $\boldsymbol{M}_{a_p}, \boldsymbol{M}_{g_p}, \boldsymbol{M}_{b_p}$: aerodynamic, gravitational, and buoyancy moments on the parafoil,
- M_p, M_F, M_r: masses of the parafoil, fluid (added mass), and capsule,
- I_p, I_F, I_r: inertia matrices for the parafoil, fluid, and capsule,

Table 5.1: Extended frame transformations for the 9DOF model, showing additional aerodynamic and body frames for parafoil (p) and capsule (r).

From	To	Transformation Matrix	Involved Variables
I	Bp	$C_{I,Bp}$	Parafoil Quaternions
I	Br	$C_{I,Br}$)	Capsule Quaternions
Ap	Bp	$C_{Ap,Bp} = C_3(\beta_{a,p})C_2(-\alpha_{a,p})$	$\alpha_{a,p}$: aoa (parafoil), $\beta_{a,p}$: sideslip (parafoil)
Ar	Br	$C_{Ar,Br} = C_3(\beta_{a,r})C_2(-\alpha_{a,r})$	$\alpha_{a,r}$: aoa (capsule), $\beta_{a,r}$: sideslip (capsule)

- $\boldsymbol{\Omega}_r, \boldsymbol{\Omega}_p$: angular velocity operators for the capsule and parafoil,
- $\mathbf{S}_{\mathbf{r_{Cr}}}, \mathbf{S}_{\mathbf{r_{Cp}}}$: skew-symmetric matrices for the position vectors r_{Cr} and r_{Cp},
- $\boldsymbol{V}_C$: velocity vector of the centre of mass.

Extended Reference Frames in the 9DOF Model

In the 9DOF model, the fundamental reference frames introduced in the 6DOF analysis remain applicable.
However, due to the presence of two distinct bodies (parafoil and capsule) within the 9DOF system, the body and aerodynamic frames each split into two sets—one for the parafoil and one for the capsule. Specifically, we now have:

- $\mathbf{B_p}$ and $\mathbf{B_r}$: Body frames for parafoil (p) and capsule (r), respectively.
- $\mathbf{A_p}$ and $\mathbf{A_r}$: Aerodynamic frames for parafoil and capsule, respectively.

Each of these frames follows the same transformation logic as in the 6DOF case, but applied independently to the parafoil and capsule. This allows the computation of separate aerodynamic angles for each body, denoted $\alpha_{a,p}, \beta_{a,p}, \sigma_{a,p}$ for the parafoil and $\alpha_{a,r}, \beta_{a,r}, \sigma_{a,r}$ for the capsule.
Table 5.1 illustrates the extended reference frame relationships and their associated transformation matrices, building on the standard frames from the 6DOF model:
By introducing these extended frames, the 9DOF equations of motion can accurately capture the individual aerodynamic environments and motions of both the parafoil and the capsule. This approach ensures that their dynamic interactions are faithfully represented, facilitating a deeper understanding of the coupled system's behaviour.

5.2. Model Geometry and Aerodynamic Properties

In this section, we discuss the geometrical and aerodynamic properties that influence the behaviour of the parafoil and payload. These properties include the mass and inertia distributions, aerodynamic centres, and coefficients that determine how the bodies respond to external forces.

Apparent Mass Considerations

The apparent mass and inertia effects are important when considering the added resistance to motion due to the surrounding fluid. The apparent mass matrix $\mathbf{I_{a.m.}}$ and the apparent inertia matrix $\mathbf{I_{a.i.}}$ are used to represent these effects:

$$\mathbf{I_{a.m.}} = \begin{bmatrix} A & 0 & 0 \\ 0 & B & 0 \\ 0 & 0 & C \end{bmatrix} \tag{5.15}$$

$$\mathbf{I_{a.i.}} = \begin{bmatrix} I_A & 0 & 0 \\ 0 & I_B & 0 \\ 0 & 0 & I_C \end{bmatrix} \tag{5.16}$$

Table 5.2: Parameters of the parafoil system

Parameter	Symbol	Value
Canopy area	S	$3.14\,m^2$
Aspect ratio	AR	3
Canopy span	b	$3.07\,m$
Canopy chord	c	$1.02\,m$
Canopy thickness	t	$0.075\,m$
Canopy height	a	$0.164\,m$
Line length	R	$1.84\,m$
Rigging angle	μ	-12 deg
Parafoil areal density	σ	$0.45\,kg/m^2$
Parafoil anhedral angle	ϵ	47.74 deg
Distance between Capsule point and Hinge	R_r	$0.31\,m$
Distance between Parafoil point and Hinge	R_p	$1.24\,m$
Distance between Parafoil point and ac (parafoil aerodynamic centre)	x_{pa}	$0.26\,m$
Payload dimensions	$W = D = H$	$0.5\,m$
Payload drag coefficient	C_{Dr}	0.4
Payload reference area	S_B	$0.25\,m^2$

The apparent mass and inertia contributions are calculated according to the following equations from Prakash and Ananthkrishnan (2006):

$$A = 0.666\rho\left(1+\frac{8}{3}a^* t^2\right)t^2 b \tag{5.17}$$

$$B = 0.267\rho\left(1+2\frac{a^*}{t^*}AR^2(1-t^{*2})\right)t^2 c \tag{5.18}$$

$$C = 0.785\rho\sqrt{1+2a^*(1-t^2)}\frac{AR}{1+AR}c^2 b \tag{5.19}$$

$$I_A = 0.055\rho\frac{AR}{1+AR}c^2 b^3 \tag{5.20}$$

$$I_B = 0.0308\rho\frac{AR}{1+AR}\left(1+\frac{\pi}{6}(1+AR)ARa^* t^{*2}\right)c^4 b \tag{5.21}$$

$$I_C = 0.0555\rho\left(1+8a^{*2}\right)t^2 b^3 \tag{5.22}$$

where

- $AR = \frac{b}{c}$ is the aspect ratio.
- $a^* = \frac{a}{b}$ is the arc-to-span ratio.
- $t^* = tc^{-1}$ is the relative thickness.
- ρ is the fluid density.
- a, b, c, and t represent characteristic dimensions of the system.

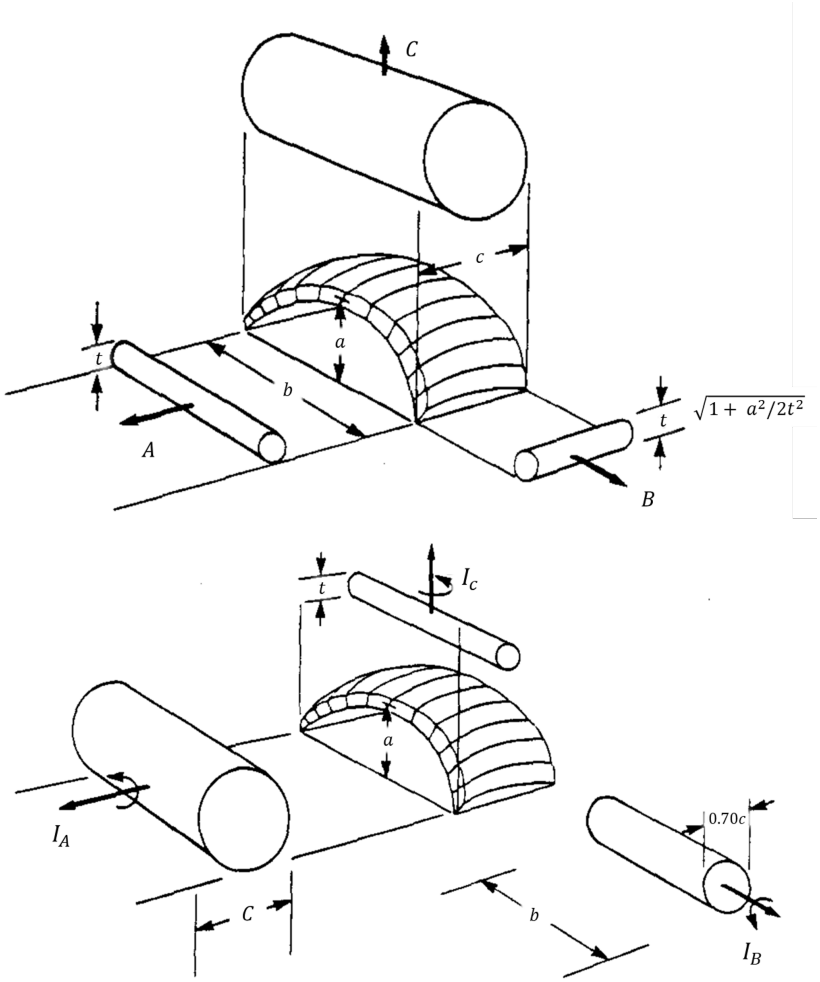

Figure 5.2: Apparent mass description of the parafoil: Adapted from LISSAMAN and BROWN (1993)

5.3. Aerodynamic Forces and Moments

This section details the forces and moments acting on the 9DOF parafoil-payload system due to aerodynamic, gravitational, and buoyancy effects. Considering both the parafoil and payload as separate rigid bodies connected by a hinge, the analysis captures the influence of their unique aerodynamic properties and dynamic interactions. The equations herein include expressions for aerodynamic forces, such as lift, drag, and side forces, as well as the resulting moments about the hinge point. These formulations are essential for accurately modelling the coupled behaviour of the parafoil and payload under various flight conditions and understanding their contributions to overall system stability and performance.

5.3.1. Aerodynamic Parameter Equations

The aerodynamic parameter equations provide a mathematical framework to describe the relationships between these coefficients and the flow variables. For the parafoil and capsule, the equations capture contributions from static and dynamic aerodynamic effects, control surface deflections, and coupling terms. This ensures accurate modelling of the forces and moments experienced by the system during its descent.

$$C_D = C_{D0} + C_{D\alpha^2}\alpha^2 + C_{D\delta_s}\delta_s \tag{5.23}$$

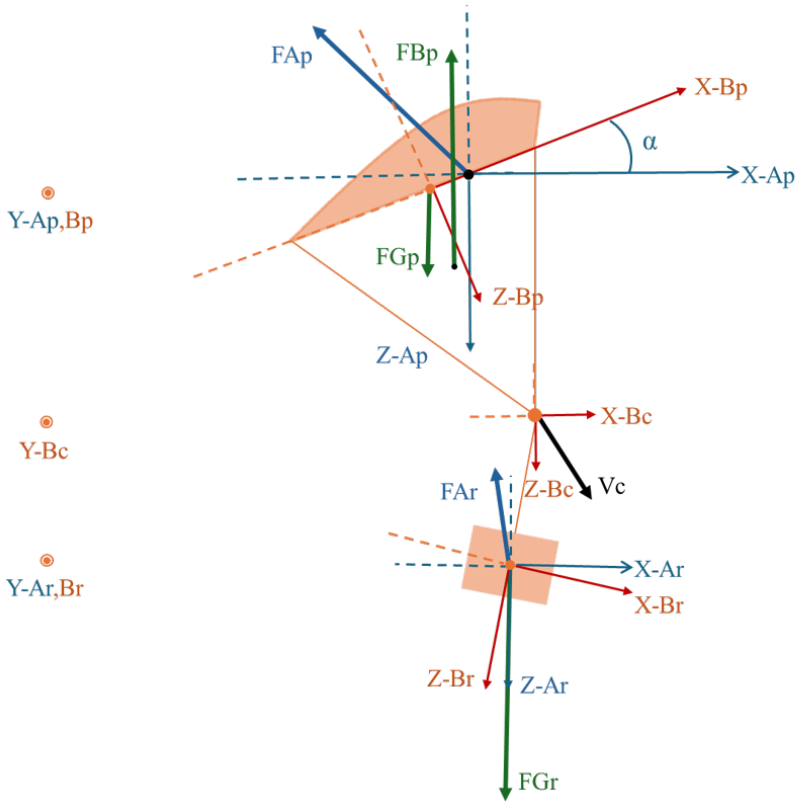

Figure 5.3: External forces acting on the system.

$$C_Y = C_{Y\beta}\beta \tag{5.24}$$

$$C_L = C_{L0} + C_{L\alpha}\alpha + C_{L\delta_s}\delta_s \tag{5.25}$$

$$C_X = \frac{-C_D u_p + C_L w_p}{V_P} \tag{5.26}$$

$$C_Z = \frac{-C_D w_p - C_L u_p}{V_P} \tag{5.27}$$

$$C_l = C_{l\beta}\beta + \frac{b}{2V_P}C_{lp}p + \frac{b}{2V_P}C_{lr}r + C_{l\delta_a}\delta_a \tag{5.28}$$

$$C_m = C_{m0} + C_{m\alpha}\alpha + \frac{c}{2V_P}C_{mq}q \tag{5.29}$$

$$C_n = C_{n\beta}\beta + \frac{b}{2V_P}C_{np}p + \frac{b}{2V_P}C_{nr}r + C_{n\delta_a}\delta_a \tag{5.30}$$

5.3.2. Forces

The parafoil and payload experience aerodynamic forces $\boldsymbol{F}_{a_p}$ and $\boldsymbol{F}_{a_r}$, along with corresponding moments based on their respective areas and airspeeds. The forces are modelled as follows:

$$\boldsymbol{F}_{a_p} = \frac{1}{2}\rho V_p^2 S \begin{pmatrix} C_X \\ C_Y \\ C_Z \end{pmatrix} \tag{5.31}$$

$$\boldsymbol{F}_{a_r} = \frac{1}{2}\rho V_r^2 S_r \begin{pmatrix} C_{X_r} \\ C_{Y_r} \\ C_{Z_r} \end{pmatrix} \tag{5.32}$$

where:

- ρ: atmospheric density,
- V_p and V_r: airspeeds of the parafoil and capsule, respectively,
- S and S_r: reference areas for the parafoil and capsule,
- C_X, C_Y, C_Z: aerodynamic coefficients for the parafoil,
- $C_{X_r}, C_{Y_r}, C_{Z_r}$: aerodynamic coefficients for the capsule.

Additionally, gravitational and buoyancy forces acting on the parafoil and capsule are given as:

$$\boldsymbol{F}_{G_p} = m_p \mathbf{g} \tag{5.33}$$
$$\boldsymbol{F}_{G_r} = m_r \mathbf{g} \tag{5.34}$$
$$\boldsymbol{F}_{B_p} = -m_{\text{added}} \mathbf{g} \tag{5.35}$$

where:

- m_p and m_r: masses of the parafoil and capsule,
- m_{added}: added mass for buoyancy,
- $\mathbf{g}$: gravitational acceleration vector.

5.3.3. Moments

The aerodynamic and gravitational forces, along with the buoyancy force, generate moments due to their offset from the centre of mass. These moments are computed using the skew-symmetric matrices S_{rp} and S_{rr}.
The resulting moments are calculated as:

$$\boldsymbol{M}_{G_p} = S_{rp} \boldsymbol{F}_{G_p} \tag{5.36}$$
$$\boldsymbol{M}_{G_r} = S_{rr} \boldsymbol{F}_{G_r} \tag{5.37}$$
$$\boldsymbol{M}_{B_p} = S_{rp} \boldsymbol{F}_{B_p} \tag{5.38}$$
$$\boldsymbol{M}_{a_p} = S_{rp} \boldsymbol{F}_{a_p} \tag{5.39}$$
$$\boldsymbol{M}_{a_r} = S_{rr} \boldsymbol{F}_{a_r} \tag{5.40}$$

where:

- $\boldsymbol{M}_{G_p}$: moment due to gravitational force on the parafoil,
- $\boldsymbol{M}_{G_r}$: moment due to gravitational force on the capsule,
- $\boldsymbol{M}_{B_p}$: moment due to buoyancy force on the parafoil,
- $\boldsymbol{M}_{a_p}$: moment due to aerodynamic force on the parafoil,
- $\boldsymbol{M}_{a_r}$: moment due to aerodynamic force on the capsule.

The aerodynamic moments acting on the parafoil are defined as:

$$M_{Ap} = \frac{1}{2}\rho V_p^2 S \begin{pmatrix} bC_l \\ cC_m + x_{pa}C_z \\ bC_n \end{pmatrix} \tag{5.41}$$

where:

- b: span of the parafoil,
- c: chord length,
- x_{pa}: aerodynamic centre offset,
- C_l, C_m, C_n, C_z: aerodynamic coefficients for lift, pitching moment, yawing moment, and normal force.

6

Software Design

This chapter focuses on the design, verification, and validation of the software models developed to analyse the parafoil-capsule system's descent dynamics under Titan-like conditions. The primary goal of this study is to understand the inherent stability and dynamic behaviour of parafoil systems during planetary descent. This verification process ensures that the models accurately capture the physical phenomena necessary to address the following research objectives and sub-questions introduced in chapter 1:

1. **Stability in Dynamics**: What are the key factors influencing the rotational stability of parafoil systems during descent on Titan?

2. **Dynamic Coupling Effects**: How do flexibility and coupling between the parafoil and capsule impact the overall dynamics of the system?

The verification steps presented in this chapter are essential to ensure the accuracy and robustness of the models used to answer these questions. The verification process specifically addresses the scope, which emphasizes:

- **Model Development:** Ensuring both 6DOF and 9DOF models accurately represent the parafoil-capsule dynamics.

- **Verification Criteria:** Confirming energy conservation, and eigenvalue analysis outcomes.

- **Open-Loop Stability Analysis:** Evaluating the system's response to perturbations without active control inputs.

By rigorously verifying these models, this chapter establishes a solid foundation for the sensitivity analyses and wind tests conducted in chapter 7. The verification steps ensure that the subsequent results are based on reliable and physically accurate simulations, ultimately contributing to the study's overall goal of advancing precision landing technologies for Titan.

6.1. Software Architecture Overview

The software architecture, illustrated in Figure 6.1, outlines the overall structure of the 6DOF parachute-payload system model. Developed in MATLAB Simulink, the modular design allows for organised development, testing, and validation of each subsystem while leveraging the robustness of a variable time-step integrator (ode15s). This integrator was chosen for its ability to efficiently handle the rapidly changing dynamics of the system, especially made to handle stiff equations.

6.1.1. Top-Level System Diagram

Figure 6.1 illustrates the updated top-level software architecture for the 6DOF model, showcasing how various components interact through well-defined inputs and outputs. This diagram provides a clear depiction of the modular structure, emphasizing how transformations, forces and moments, and equations of motion integrate into a cohesive system.
The system architecture is divided into the following primary subsystems, each responsible for a specific function within the simulation:

1. **Transformations**: This block provides the necessary transformation matrices to convert between different reference frames (e.g., inertial to body frame) and calculate orientation angles. It ensures consistency in coordinate systems across all subsystems.

2. **Flight Module**: The flight module computes aerodynamic properties such as lift, drag, and pitching moment coefficients, using input parameters like angle of attack (α) and sideslip angle (β). It directly feeds these coefficients to the forces and moments block for further computations.

3. **System Module**: This block defines the mass, geometry, and inertia properties of the system, including parafoil and payload characteristics. It accounts for variations in these properties during the simulation and ensures accurate representation of the system's physical attributes.

4. **Hinge Mechanism**: Specific to the 9DOF model, this block models the dynamics of the hinge connecting the parafoil and payload. It computes spring and damper forces that account for the relative motion between the components.

5. **Environment**: The environment subsystem models atmospheric conditions such as density, pressure, and wind velocities (both steady-state and gust components). It provides these values based on the system's altitude and state, ensuring accurate simulation of external influences.

6. **Forces and Moments**: This subsystem calculates the resultant forces and moments acting on the system by combining inputs from the flight module, environment, and system module. It outputs these values to the equations of motion block for state propagation.

7. **Equations of Motion (EOM)**: This block integrates the translational and rotational equations of motion using the $ode15s$ solver. It uses inputs from the forces and moments block and propagates the state variables (position, velocity, orientation) for the next time step.

The modular design of this architecture facilitates independent testing and debugging of each subsystem, allowing them to be verified in isolation before integrating into the full system. Simulink's Goto/From tags are utilized to streamline data flow, reducing clutter and improving readability of the model layout.

6.1.2. Simulation Propagation

The propagation of state vectors forms the core of the simulation process. At each time step, the simulation follows a structured sequence of computations, ensuring that all forces, moments, and environmental influences are accurately captured. The updated propagation logic is as follows:

1. **Compute Position, Velocity, and Attitude Angles**: Position, velocity, and attitude states are updated using inputs from the environment and transformations subsystems. These values serve as the foundation for subsequent computations.

2. **Retrieve Wind Data**: The wind vector is obtained from the environment subsystem, incorporating both steady-state and gust components. The wind conditions depend on the current altitude, latitude, and longitude.

3. **Compute Flight Parameters**: Parameters such as atmospheric density, Mach number, and dynamic pressure are calculated based on the current airspeed and altitude of the system.

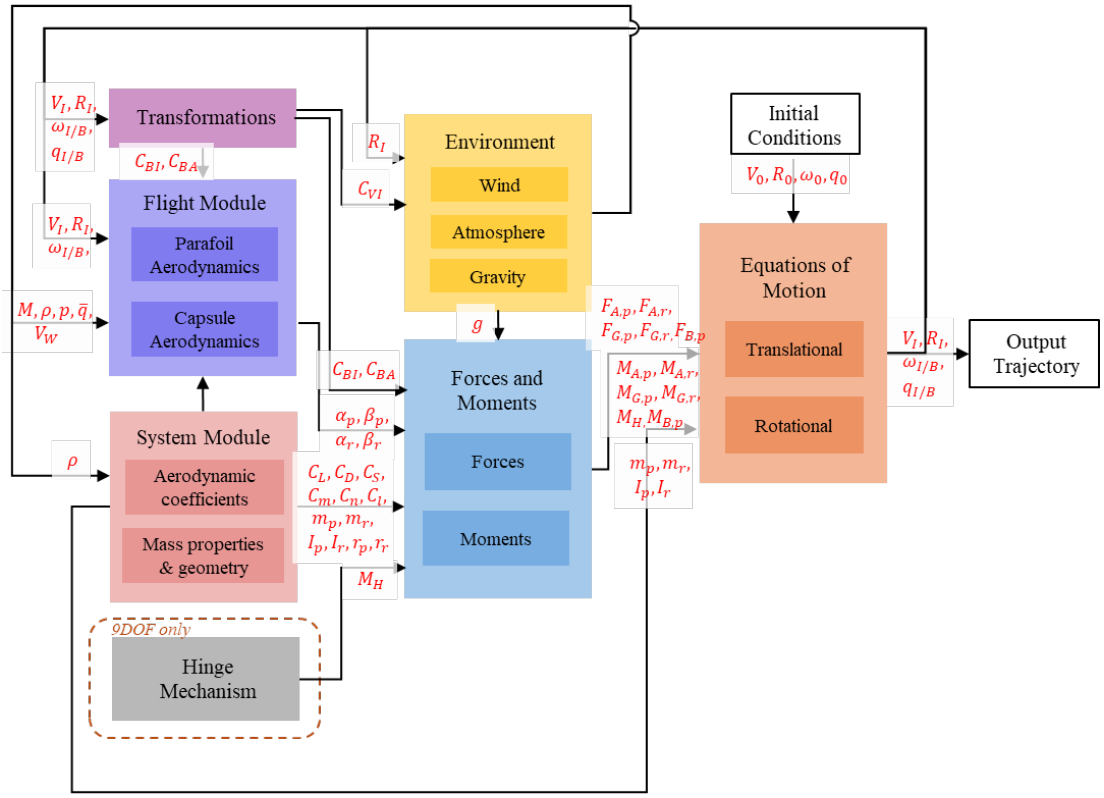

Figure 6.1: Software architecture of the 6DOF parachute-payload system model.

4. **Calculate Aerodynamic Forces and Moments**: Using aerodynamic coefficients from the flight module, the forces and moments block computes lift, drag, and pitching moments based on the system's current state.

5. **Update Mass Properties**: This step accounts for any changes in mass or inertia properties due to system dynamics, particularly for the parafoil and payload. These updates are provided by the system module.

6. **Evaluate Gravitational Forces**: Gravitational forces and torques are calculated based on the relative positions and mass properties of the components.

7. **Integrate Equations of Motion**: The rotational and translational equations of motion are solved using the $ode15s$ solver to update state variables, ensuring the propagation of the simulation to the next time step.

For the 6DOF system, the rotational and translational equations are treated independently, whereas the 9DOF system requires coupling between the parafoil and payload through hinge dynamics, which will be further elaborated in the 9DOF subsystem discussion.
Each of these computations ensures that the complex aerodynamic, gravitational, and environmental interactions affecting the system are accurately represented, facilitating the analysis of stability and control characteristics of both the parachute and parafoil models.

6.2. Verification and Validation

The verification efforts presented in this section are critical to ensuring the fidelity and robustness of the developed 6DOF and 9DOF parafoil models. This aligns directly with the overarching research objectives, particularly the goal of understanding the stability and dynamic behaviour of parafoil

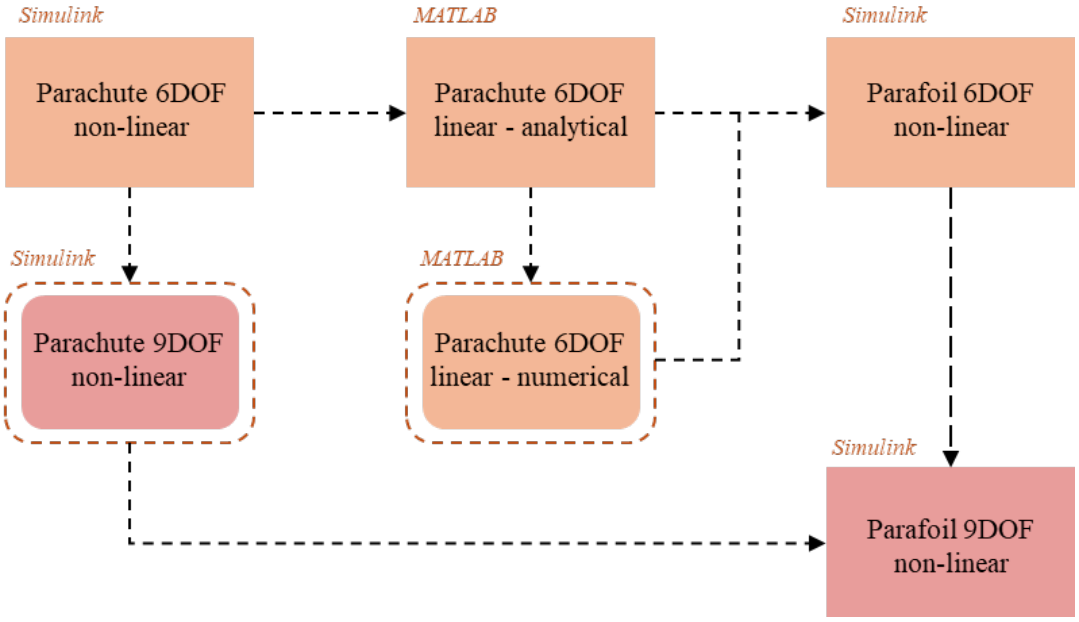

Figure 6.2: Iterative development process of dynamic models, transitioning from 6DOF parachute models to the final 9DOF parafoil model, with analytical, numerical, and non-linear verification.

systems under Titan-like conditions. High-fidelity modelling requires rigorous verification to confirm that the implemented equations of motion, aerodynamic formulations, and dynamic couplings accurately represent the physical system. Without this foundation, the sensitivity analyses and wind tests in subsequent chapters would lack the reliability needed to draw meaningful conclusions.
This chapter systematically addresses verification across multiple levels, including subsystem validations, energy conservation tests, and angular momentum checks. Each test evaluates specific aspects of the models to ensure consistency, accuracy, and adherence to physical laws. By establishing the reliability of the models, this chapter provides a solid basis for the more detailed stability and sensitivity analyses explored later in this study.

6.2.1. Verification Plan

The verification of the simulation models were carried out through a structured and systematic approach to ensure the accuracy and reliability of the results. The plan consisted of several key stages, starting with the parachute model and gradually expanding to the more complex parafoil models. Below, the steps taken for verification are described in detail.
To ensure the robustness and accuracy of the final 9DOF parafoil model, a step-by-step approach was employed, involving several intermediate models. The process began with the development of a 6DOF parachute non-linear model in Simulink, serving as the foundation for analysing the dynamic behaviour of the parachute-capsule system.
Next, two parallel verification approaches were conducted in MATLAB:

- **Analytical linearisation:** This method focused on rotational dynamics, providing a theoretical basis for stability analysis.
- **Numerical linearisation:** Central difference approximations were used to confirm the results from the analytical model.

Building on these insights, a 9DOF parachute non-linear model was developed to incorporate flexible coupling effects between the parachute and capsule. This enabled a more detailed analysis of system sensitivity and stability.

The process then advanced to parafoil-specific configurations, starting with a 6DOF parafoil non-linear model to account for unique aerodynamic effects. Finally, the 9DOF parafoil non-linear model combined all previous insights, introducing flexible dynamics between the parafoil and capsule. This iterative approach ensured a thorough verification process at every stage, systematically isolating key effects and validating assumptions, resulting in a high-fidelity and reliable final model.

Initial Validation Using Huygens Capsule Data

As an initial step in the validation process, the 6DOF parachute simulator was validated using real mission data from the Huygens capsule, provided by TU Delft. This step ensured that the simulator accurately modelled the dynamics of a parachute-capsule descent system under realistic conditions. Although the results of this validation are not shown in the report, this initial step forms an integral part of the verification process, as it demonstrated that the 6DOF simulator could reliably replicate known descent dynamics.

Subsystem Tests

To ensure the accuracy and robustness of each component within the overall software architecture, subsystem tests are performed on individual blocks identified in the software architecture diagram (Figure 6.1). These subsystems represent the core functional modules of the parafoil-capsule model, and verifying each subsystem independently helps isolate potential errors and confirm that each block performs as intended. Each subsystem test involves comparing the outputs of these blocks against analytical solutions, known benchmarks, or simplified scenarios where the expected behaviour is well understood. By validating each subsystem independently, this approach ensures that the overall model is built on reliable and accurately functioning components, reducing the risk of compounding errors in the full-system verification. These subsystem tests form a critical part of the overall verification process, providing confidence that each module contributes correctly to the complete parafoil-capsule simulation.

Vacuum Energy Balance: Parachute Model

The verification process began with an energy balance test on the 6DOF parachute model under vacuum conditions, where aerodynamic forces were excluded. In the absence of aerodynamic forces, the total energy of the system (kinetic + potential) remains constant throughout the descent. This test served as a baseline check for the accuracy of the energy calculations in the simulator. The results showed consistent total energy over time, confirming the correctness of the potential and kinetic energy formulations in the simulator. This initial step established confidence in the energy framework of the parachute model.

Aerodynamic Energy Analysis: Parachute Model

Following the vacuum energy balance test, aerodynamic forces were introduced into the 6DOF parachute model. For a vertical descent, only the drag force acts on the system, making the aerodynamic energy analysis straightforward. The work done by aerodynamic forces was calculated and observed to match the predicted energy dissipation due to drag. This test further validated the energy balance calculations in the presence of aerodynamic forces and demonstrated the accuracy of the simulator for modelling vertical descent dynamics.

Energy Balance Tests: Parafoil Models

Building on the results of the parachute model, energy balance tests were extended to the parafoil models. The 6DOF and 9DOF parafoil models were analysed under both vacuum and aerodynamic conditions. The vacuum energy balance test for the parafoils yielded results similar to the parachute model, with the total energy remaining constant over time. When aerodynamic forces were included, the work done by drag and lift forces was calculated, and the total energy loss was observed to match the expected dissipation. These tests validated the parafoil energy calculations and highlighted the differences in energy dissipation between the rigid-body 6DOF model and the flexible 9DOF model.

Table 6.1: Summary of Verification and Validation Steps

Verification Step	Description
1. Initial Validation	Validation of the 6DOF parachute simulator using Huygens capsule descent data to ensure baseline accuracy.
2. Vacuum Energy Balance Tests	Verification of energy conservation in the parachute and parafoil models under vacuum conditions.
3. Aerodynamic Energy Analysis	Analysis of energy conservation under aerodynamic forces for the parachute model.
4. Stiffness Tests	Comparison of dynamic responses between 6DOF and 9DOF parafoil models to assess the impact of flexibility.
5. Linearisation and Eigenvalue Analysis	Verification of the 6DOF simulator through linearisation and eigenvalue analysis to identify key sensitivity parameters.

Stiffness Tests: Parafoil Models

To further investigate the dynamics of the parafoil models, stiffness tests were conducted on the 9DOF model by making the spring-damper system connecting the parafoil and capsule increasingly stiff. The results were compared with the 6DOF rigid-body model. These tests revealed differences in oscillation magnitudes and damping behaviour between the two models, which were attributed to the separation of moments of inertia and load distribution in the 9DOF model. The stiffness tests provided additional insights into the dynamics of the flexible system and highlighted the importance of accurately modelling flexibility in aerodynamic systems.

linearisation and Eigenvalue Analysis

The final stage of verification involved the linearisation of the 6DOF parachute model. An analytical linearised model was developed, and its eigenvalue analysis results were compared with the numerical results from the simulator, focusing on damping ratios and natural frequencies. The close agreement between the analytical and numerical results further validated the accuracy of the simulator. Additionally, a preliminary sensitivity analysis was performed on the linearised model to identify key parameters for the subsequent sensitivity analysis chapter. This step provided a final layer of verification for the 6DOF simulator and ensured the robustness of the numerical model.

Summary of Verification

In this study, a rigorous verification process was implemented to ensure the reliability and accuracy of the simulation models developed for parafoil and parachute dynamics. Table 6.1 summarizes the key steps undertaken in this process, highlighting the progressive approach to validating individual components and system-level behaviours. These steps include initial validation against empirical data, energy conservation analyses, and comparative tests to assess the influence of flexibility and aerodynamic forces. Each step played a crucial role in building confidence in the fidelity of the models and their suitability for the analysis of parafoil stability and performance.
This comprehensive approach ensured that the simulators were thoroughly tested and validated, establishing confidence in the models used for further analysis and sensitivity studies.

6.2.2. Subsystem Verification Steps

To ensure the accuracy and robustness of the implemented software architecture, key subsystems were rigorously tested in isolation. The modular structure of the architecture facilitated independent verification of these components before integrating them into the larger system. This section

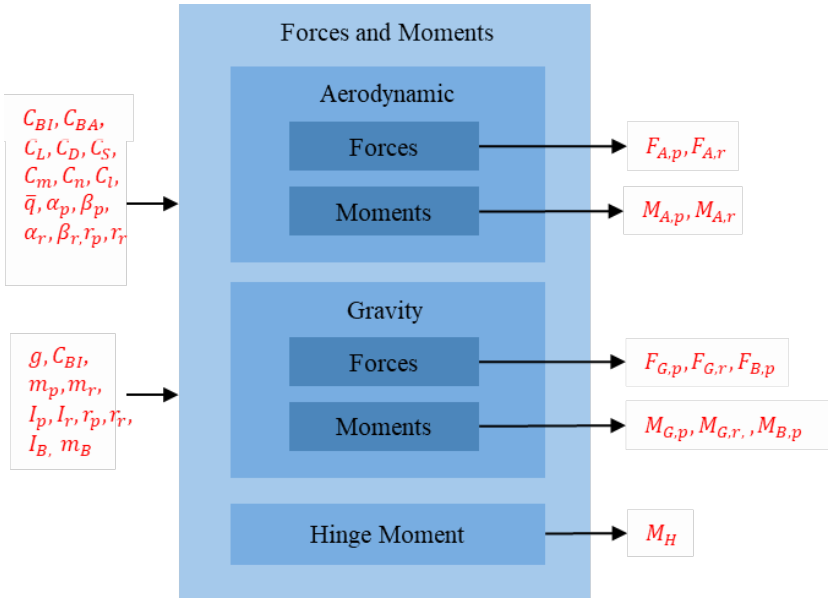

Figure 6.3: Software Diagram for the forces and moments block

elaborates on the verification procedures applied to subsystems that required additional detail due to their complexity and importance.

Forces and Moments Block

The *Forces and Moments* block, responsible for computing aerodynamic forces, moments, and gravity contributions, was validated through several targeted tests:

- **Aerodynamic Forces:** In the case of a vertical descent with a parachute model, the drag coefficient (C_{D0}) corresponding to an angle of attack (α) of 0° was passed into the block. The resulting force output in the aerodynamic frame was verified to contain only a vertical drag component, with no lift or side force contributions.
- **Forces Under Small Angles:** For a small non-zero angle of attack, the outputs of the aerodynamic force components in the x, y, and z directions were cross-verified using free-body diagrams. This ensured consistency with the expected physical behaviour of the system.
- **Moments:** For the same vertical descent scenario, aerodynamic moments were verified to be zero, as expected. In contrast, moments resulting from weight forces were checked to confirm consistency with theoretical calculations.

These verifications established confidence in the accuracy of the aerodynamic and gravity force computations under various scenarios.

Flight Module Block

The *Flight Module*, which handles body velocities and computes aerodynamic angles such as α (angle of attack) and β (sideslip angle), was subjected to verification tests that combined analytical derivations and numerical outputs:

- **Velocity Transformations:** Free-body diagrams were used to validate velocity transformations between the body and aerodynamic frames.
- **Aerodynamic Angles:** The computed values of α and β were compared against expected results derived from the velocity components in the aerodynamic frame. Discrepancies were resolved to ensure the correctness of the implemented transformations.

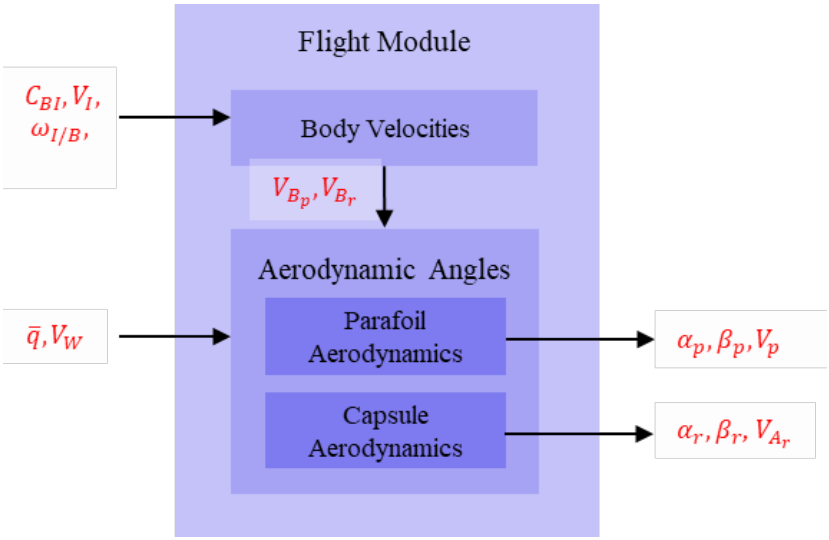

Figure 6.4: Software Diagram for the flight module block

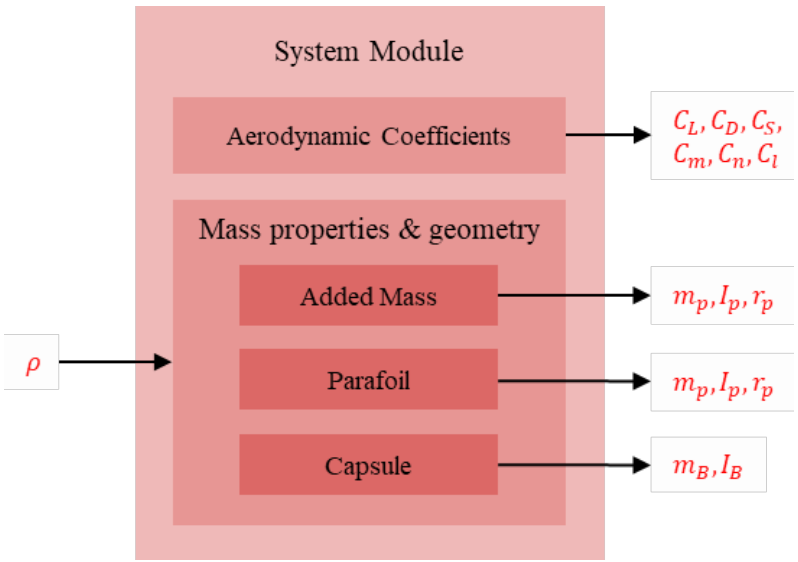

Figure 6.5: Software Diagram for the system module block

These steps confirmed that the module reliably translated velocity information into aerodynamic angles critical for force and moment calculations.

System Module Block

The *System Module*, which encapsulates constants and formulas to calculate mass and geometry properties, was verified through parameter-based tests:

- **Scaling with Density:** Outputs dependent on surface density (ρ), such as added mass and moment of inertia, were verified to scale correctly with ρ. This included plotting the behaviour of mass moment of inertia for all bodies involved in the models.

This verification ensured that the system module produced accurate results for different environmental and geometric configurations.

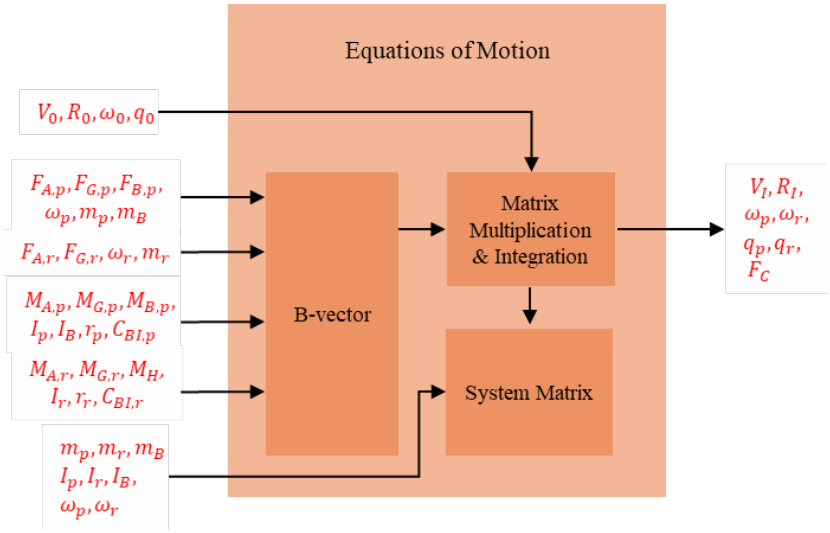

Figure 6.6: Software Diagram for the equations of motion of the 9DOF block

Equations of Motion Block

The *Equations of Motion (EOM)* block, tasked with integrating the translational and rotational dynamics, was verified as follows:

- **6DOF EOM:** For the 6DOF model, the translational and rotational equations were straightforward and validated by checking that the accelerations matched the forces divided by total mass. Angular velocities were manually calculated using moments and moments of inertia and cross-referenced with simulation outputs.

- **9DOF EOM:** The 9DOF model presented additional complexity due to the coupling of the parafoil and capsule. Separate equations for the forces and moments acting on each body were implemented. These were combined with the system matrix, which handled the distinct mass and inertia properties of the two bodies. Verification involved ensuring that matrix multiplications and state integrations produced expected state variable propagations.

By rigorously testing the subsystems, the implemented software architecture was validated to handle the complexities of both the 6DOF and 9DOF models, providing confidence in the simulation results for further analysis.

Integrated Testing Across Subsystems

While each subsystem was tested in isolation, the rotations and forces and moments blocks were isolated for every test case (*e.g.*, 6DOF parachute, 6DOF parafoil, 9DOF parafoil). These subsystems were critical for determining parameters such as angle of attack, velocity, and force and moment balances. Verification steps included:

- Checking expected outputs at $t = 0\,\text{s}$, $t = 10\,\text{s}$, etc., for all simulations.

- Validating rotation matrices, angle of attack, and velocity transformations across all cases.

- Ensuring individual force and moment balance outputs matched expected values.

These thorough validation steps provided confidence in the correctness and reliability of the overall system.

6.2.3. Verification Tests

Conservation of Energy: Vacuum

To establish a baseline for energy balance verification, both the 6DOF and 9DOF models were simulated under vacuum conditions, where aerodynamic forces and damping effects were removed. The energy components (total, kinetic, and potential) were calculated for each model, and their evolution over time was compared.

- **Total Energy Conservation:** The total energy remains constant throughout the simulation, confirming no energy dissipation in the absence of aerodynamic forces.
- **Potential and Kinetic Energy Exchange:** Potential energy decreases while kinetic energy increases, demonstrating the proper exchange of energy due to gravitational effects.
- **Agreement Between Models:** Both models produce nearly identical results for all energy components, confirming the consistency of the energy formulations across the 6DOF and 9DOF representations.

This vacuum case serves as the first step in the verification process. By removing aerodynamic forces, the simulation isolates gravitational interactions, ensuring that both models correctly implement the fundamental equations of motion and energy dynamics. The results provide confidence that any discrepancies observed in later simulations with aerodynamic forces can be attributed to aerodynamic effects, rather than numerical inconsistencies in the gravitational energy or force calculations.

Conservation of Energy: Full system

Next, the verification of the energy balance was conducted for both the 6DOF and 9DOF models by calculating the kinetic, potential, and aerodynamic energies for each mass point (capsule and parafoil). The following steps outline the methodology, equations used (followed from Hibbeler (2013)), and a discussion of the results.

The kinetic energy for each mass point was calculated using the velocity in the body-fixed frame ($\mathbf{V}_B$) as:

$$KE_{\text{trans}} = \frac{1}{2} m \mathbf{V}_B^2, \tag{6.1}$$

where m is the mass of the body, and $\mathbf{V}_B$ is the velocity magnitude in the body frame. The total translational kinetic energy for the system was obtained by summing the translational kinetic energies of the capsule and the parafoil.

In addition to translational kinetic energy, rotational kinetic energy was also calculated for each mass point. The rotational kinetic energy (KE_{rot}) was given by:

$$KE_{\text{rot}} = \frac{1}{2} \boldsymbol{\omega}^T \mathbf{I} \boldsymbol{\omega}, \tag{6.2}$$

where $\boldsymbol{\omega}$ is the angular velocity vector of the body in the body-fixed frame, and $\mathbf{I}$ is the moment of inertia tensor of the body. This term accounts for the kinetic energy due to rotational motion of both the capsule and the parafoil.

The total kinetic energy for each mass point was therefore the sum of the translational and rotational kinetic energies:

$$KE_{\text{total}} = KE_{\text{trans}} + KE_{\text{rot}}, \tag{6.3}$$

and the total kinetic energy for the entire system was obtained by summing the total kinetic energies of the capsule and the parafoil.

The gravitational potential energy was computed relative to the planetary surface:

$$PE = -\frac{GMm}{r} + \frac{GMm}{R_{\text{surface}}}, \tag{6.4}$$

where G is the gravitational constant, M is the planetary mass, m is the mass of the body, r is the radial distance from the center of the planet, and R_{surface} is the planetary radius.

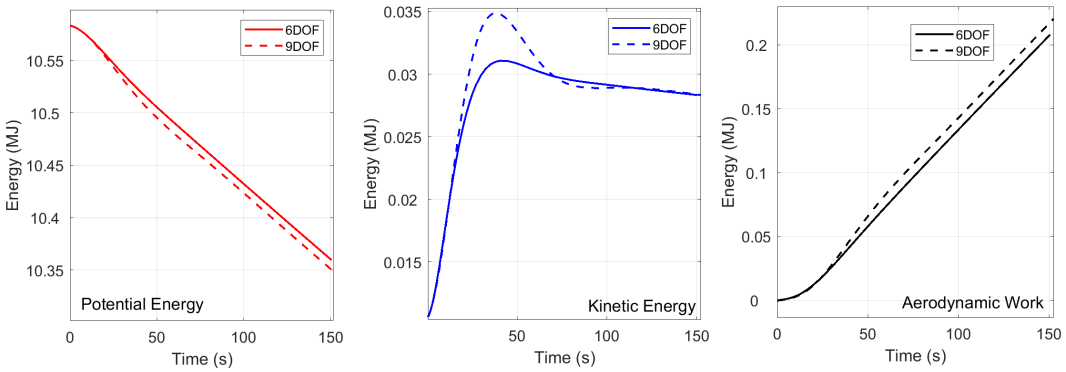

Figure 6.7: Overlay of energy components (kinetic, potential, aerodynamic) for the first 150 seconds of descent for the 6DOF and 9DOF models.

The aerodynamic energy was determined by calculating the work done by aerodynamic and buoyancy forces. The instantaneous power due to aerodynamic forces ($\mathbf{F}_{\text{aero}}$) was given by:

$$P_{\text{aero}} = \mathbf{F}_{\text{aero}} \cdot \mathbf{V}_B, \tag{6.5}$$

and the aerodynamic work was obtained by integrating this power over time:

$$AE = \int_0^{t_{\text{final}}} P_{\text{aero}}\, dt. \tag{6.6}$$

For the 9DOF model, buoyancy forces ($\mathbf{F}_{\text{buoyancy}}$) were also included in the aerodynamic energy calculation.
The energy balance was verified by comparing the sum of kinetic and potential energies at the initial time to the sum of kinetic and aerodynamic energies at the final time. At $t = 0$, the energies were calculated based on the initial conditions of the system, which included the potential energy due to the constant masses of the parachute and capsule, and the kinetic energy corresponding to the initial velocity at release, with no added mass effects from air under the parachute. This ensures that the initial energy is appropriately mass-dependent, accurately representing the state of the system at the moment of release:

$$\text{Initial Energy: } PE(0) + KE(0), \tag{6.7}$$

$$\text{Final Energy: } KE(t_{\text{final}}) + AE(t_{\text{final}}). \tag{6.8}$$

At the final time t_{final}, the kinetic energy and accumulated aerodynamic energy were calculated to confirm that the energy was conserved or dissipated as expected under aerodynamic forces.
The results of the energy balance analysis are summarised below:

- The initial total energy for the 6DOF and the 9DOF models was calculated to be approximately 10.867 MJ and 10.878 MJ, respectively.
- For the 6DOF model, the final total energy was found to be 10.806 MJ, representing a 0.55% discrepancy, likely due to numerical integration errors and unmodelled small losses.
- For the 9DOF model, the final total energy was 10.806 MJ, with a similar discrepancy.

Figure 6.7 illustrates the evolution of the kinetic, potential, and aerodynamic energy components over the first 150 seconds of descent for the 6DOF and 9DOF models. The analysis was specifically focused on this time window as the energy profiles in the full simulation showed near-identical behaviour for both models, with minimal differences. This zoomed-in view allows for a detailed examination of any discrepancies during the early stages of descent, which were otherwise obscured in the complete analysis.

During the first 150 seconds, notable differences can be observed between the two models, particularly in the kinetic energy and oscillatory behaviour. The kinetic energy peaks for the 9DOF model are higher compared to the 6DOF model during this period, with a peak difference of approximately 8.5%. This difference arises due to the inherent flexibility of the 9DOF model, where the parafoil and capsule are connected via a spring-damper mechanism, allowing a more dynamic initial response. In contrast, the 6DOF model, which represents a rigid connection between the parafoil and capsule, exhibits a more damped initial behaviour with lower energy peaks.
Additionally, the kinetic energy oscillations for the 9DOF model are more pronounced during the initial phase, with the angle of attack for the 9DOF capsule showing greater oscillatory amplitude which was approximately 10% higher peak-to-peak variation compared to the 6DOF model. This behaviour can be attributed to the inherent flexibility in the 9DOF model, where the parafoil and capsule are connected by a spring-damper mechanism, allowing energy to be dynamically exchanged between these two components. The increased oscillation amplitude in the 9DOF model reflects the flexibility-driven dynamics that occur during the initial descent, where the parafoil and capsule, treated as separate entities, can undergo more relative movement and hence more prominent energy exchanges. In contrast, the 6DOF model, representing a rigid connection between the parafoil and capsule, has more constrained dynamics, resulting in a lower oscillation amplitude and a more stable initial response. This difference highlights the effect of the spring-damper coupling in the 9DOF model, which induces additional oscillatory behaviour and enhances the initial energy transfer dynamics, leading to greater peaks that gradually stabilize over time.
The potential energy profiles, on the other hand, show minimal variation between the two models, with discrepancies below 0.5%. Both models exhibit a consistent decrease in potential energy as the system descends, demonstrating that gravitational energy exchange is effectively the same in both cases. The close agreement in potential energy suggests that the overall altitude descent behaviour of the parafoil-capsule system is largely unaffected by the differences in coupling dynamics between the two models.
For aerodynamic energy, the 6DOF model shows a slightly faster initial increase compared to the 9DOF model. This is likely because, in the rigid 6DOF model, aerodynamic forces are directly transmitted throughout the entire system without any energy dissipation through relative motion. In contrast, the 9DOF model initially dissipates some of the aerodynamic energy through the spring-damper mechanism, leading to a more gradual buildup of aerodynamic energy. However, after approximately 100 seconds, both models converge in their aerodynamic energy values, reflecting that the initial differences in energy dissipation become negligible as the system stabilizes.
The higher kinetic energy peaks and greater oscillatory amplitude in the 9DOF model highlight the influence of hinge flexibility during the initial descent. As time progresses, these differences diminish, and the energy profiles for both models become closely aligned. This suggests that while the 9DOF model initially exhibits more complex dynamics due to its flexibility, it ultimately transitions to behave similarly to the rigid 6DOF model as the hinge damping stabilizes the system. These findings reinforce the capability of the 9DOF model to represent both flexible and rigid dynamics, providing a comprehensive tool for studying parafoil-capsule interactions under various descent conditions.

Rotational Kinetic Energy Analysis

The rotational kinetic energy (KE_{rot}) was computed for both the 6DOF and 9DOF models to analyse the contribution of rotational dynamics to the overall energy of the system. The new results reveal key differences in how energy is distributed and dissipated across the two models, with important implications for understanding their dynamics.
In the 6DOF model, the rotational kinetic energy is concentrated entirely in a single body due to its rigid coupling, resulting in a higher initial peak of KE_{rot} compared to the 9DOF model. By contrast, the 9DOF model distributes energy among its components, with rotational kinetic energy contributions from both the parafoil and capsule. This redistribution results in lower individual rotational kinetic energy peaks for each component compared to the 6DOF model. However, when combined, the rotational kinetic energy of the 9DOF model remains slightly lower than that of the 6DOF model.
A critical observation from the 9DOF model is the substantial energy absorption and dissipation by the spring-damper system. The spring energy exhibits a significant peak during the initial oscilla-

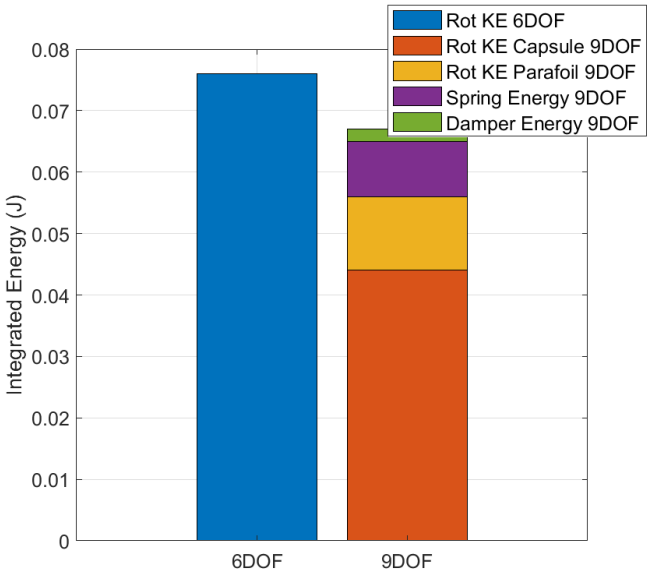

Figure 6.8: Bar chart showing the initial spike in rotational kinetic energy for the 6DOF system and the 9DOF system components

tory phase, absorbing much of the rotational energy from the parafoil and capsule. This mechanism dampens the rotational contributions more effectively than in the 6DOF model, which lacks a comparable coupling system. Over time, the spring energy dissipates entirely, along with the rotational kinetic energy, resulting in a stabilized system with negligible rotational contributions after approximately 20–30 seconds.

The bar chart in Figure 6.8 illustrating the initial energy distribution clearly demonstrates the distinct dynamics of the 9DOF model. It shows that the spring and damper energies account for a substantial portion of the system's total energy during the initial phase, while rotational energy plays a relatively minor role. This finding underscores the importance of including flexible coupling mechanisms, such as a spring-damper system, in capturing the transient energy dynamics of the system.

The differences in energy distribution between the 6DOF and 9DOF models highlight the advantages of incorporating flexibility. The rigid coupling of the 6DOF model leads to higher rotational kinetic energy and more pronounced oscillations, while the 9DOF model demonstrates a smoother dissipation of energy due to its flexibility. This flexibility not only reduces the peak rotational energy but also enhances the system's ability to stabilize more efficiently.

Conservation of Angular Momentum

Angular momentum conservation was verified for both the 6DOF and 9DOF models. The total angular momentum ($\mathbf{L}$) is given by (Hibbeler, 2013):

$$\mathbf{L} = \mathbf{I}\boldsymbol{\omega}, \tag{6.9}$$

where $\mathbf{I}$ is the moment of inertia tensor, and $\boldsymbol{\omega}$ is the angular velocity vector in the body-fixed frame.

The analysis showed a small initial spike in angular momentum within the first second of the simulation. This spike is attributed to transient effects arising from the initial conditions. After this brief spike, the angular momentum remained effectively zero throughout the descent.

This behaviour is expected, as no significant external torques acted on the system during the descent. The results confirm that the models correctly implement angular momentum conservation, aligning with the predominantly translational motion observed in the simulations.

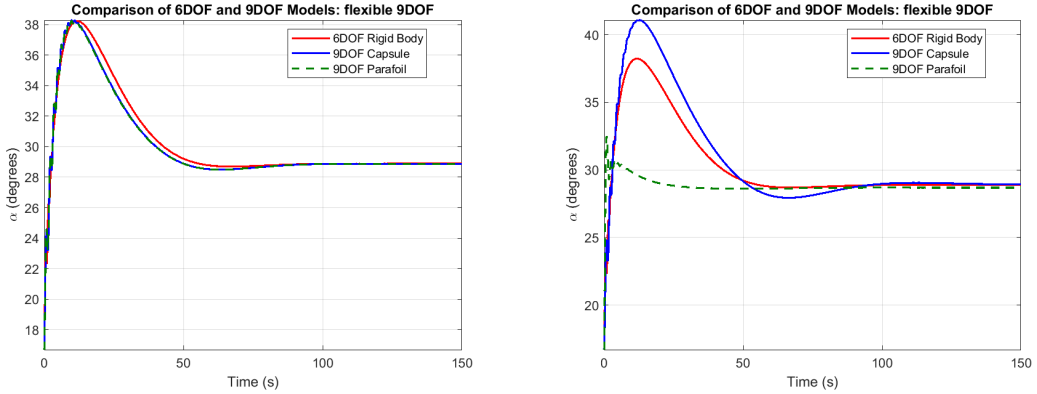

(a) Stiff 9DOF model comparison

(b) Flexible 9DOF model comparison

9DOF Hinge Stiffness

The stiffness test results serve as a critical validation tool for the 9DOF parafoil-capsule model by demonstrating its ability to replicate the dynamics of the 6DOF rigid-body model under conditions of extremely high hinge stiffness and damping. This test showcases the consistency between the two models and provides insights into the flexibility and coupling effects that distinguish them.

In the 6DOF model, the parafoil and capsule are treated as a single rigid body, with their mass and moments of inertia combined. This rigid coupling ensures that all forces and moments acting on the parafoil are directly transmitted to the entire system without dissipation or relative motion between components. As a result, the 6DOF model exhibits unified motion with larger angular oscillations driven by aerodynamic forces.

In contrast, the 9DOF model inherently allows for flexibility by treating the parafoil and capsule as two separate rigid bodies connected by a spring-damper system. Under nominal conditions, this flexibility results in distinct dynamic behaviours for the parafoil and capsule, with load distribution and energy dissipation through the hinge playing a key role in dampening oscillations. However, when the hinge stiffness and damping constants are increased to very high values, the relative motion between the parafoil and capsule is effectively eliminated, and the system begins to behave as a single rigid body. This effectively emulates the 6DOF model and confirms that the 9DOF formulation is consistent and reliable when modelling a rigid-body system.

The alignment of the 9DOF model's dynamics with the 6DOF results under stiff coupling conditions underscores the robustness of the 9DOF framework. By increasing hinge stiffness and damping, the parafoil and capsule are constrained to move in near-perfect unison, and the combined moments of inertia dominate the system's response. This behaviour validates the model's implementation and highlights its flexibility in representing both rigid and flexible system dynamics.

The results also emphasize the versatility of the 9DOF model. Under nominal conditions, the spring-damper connection allows for energy dissipation and decoupling of inertial effects, providing a realistic representation of flexible systems. Conversely, by tuning the stiffness and damping to extreme values, the model transitions to effectively represent a rigid system, mirroring the dynamics of the 6DOF model. This dual capability strengthens the confidence in the 9DOF model's fidelity and provides a comprehensive framework for analysing parafoil-capsule systems under varying coupling conditions.

In conclusion, the stiffness test results demonstrate that the 9DOF model can replicate the 6DOF rigid-body behaviour when hinge stiffness and damping are increased significantly. This finding validates the 9DOF model's ability to transition between flexible and rigid configurations, making it a robust tool for studying parafoil-capsule dynamics. The results further highlight the importance of accurately capturing system flexibility and coupling effects in dynamic simulations, as these factors play a pivotal role in determining aerodynamic stability and energy dissipation in parafoil-capsule systems.

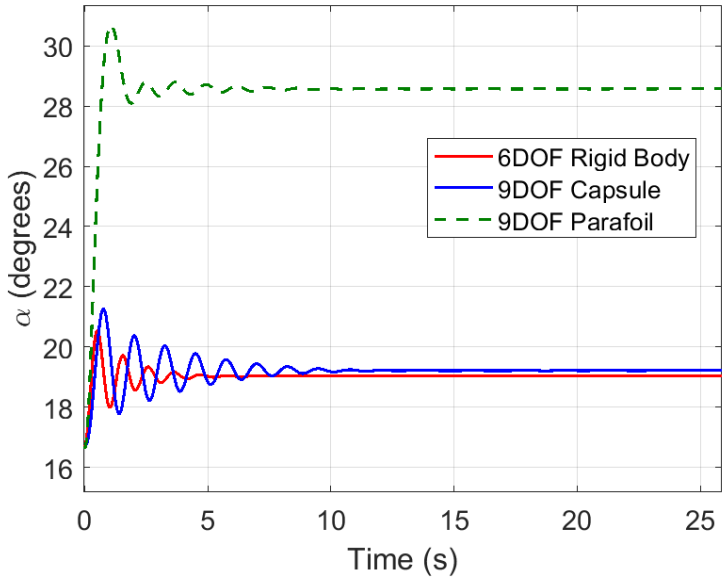

Figure 6.10: Oscillations of the 6DOF and 9DOF model at constant initial altitude and velocity conditions.

Initial Transient Perturbation

During the early stages of the simulation (typically within the first 10 s), a distinctive transient perturbation or "wobble" is observed in the angle of attack response across both the 6DOF and 9DOF models. Initially, this wobble was more pronounced, potentially suggesting numerical instabilities stemming from discretisation errors or non-ideal integrator selections. By employing a more suitable numerical solver (specifically, `ode15s`, which is designed for stiff systems) and refining the initial conditions, the amplitude of these early oscillations was significantly reduced. Despite these improvements, the residual wobble remains a consistent feature of the system's dynamics.

Upon closer examination, the wobble appears to be a physically meaningful response rather than a purely numerical artifact. In the modelled configuration, the parafoil initially experiences a rapid shift in lift and drag forces as it engages with the airflow, while the capsule hangs beneath it, imparting a competing gravitational moment. This interplay results in a brief period of dynamic adjustment as the parafoil and capsule seek a new aerodynamic and inertial equilibrium state. The mismatch in moments—lift and drag attempting to stabilize the system's orientation against the persistent weight force—naturally induces small initial oscillations. These early transients are further influenced by the chosen initial conditions for altitude and velocity; when these are held constant, the observed behaviour remains consistent, reinforcing the notion that the wobble is tied to the inherent physics of the coupled system.

Additional evidence for the physical origin of the wobble arises from test scenarios where aerodynamic forces were completely disabled. In the absence of aerodynamic loading, the system simply settles toward a vertical equilibrium (approaching a 90-degree orientation) without any initial oscillatory behaviour. This confirms that the transient wobble is not a numerical artifact, but rather a direct consequence of the complex, coupled aerodynamic and gravitational forces acting on the flexible parafoil-capsule system as it transitions into steady descent.

Integrator Trade-Off Analysis

The choice of numerical integrators plays a critical role in simulating the dynamics of the 9DOF parafoil model accurately and efficiently. Given the system's stiff equations, a suitable integrator ensures stability and smoothness while maintaining acceptable computation times. A trade-off analysis was conducted by testing multiple fixed-step and variable-step integrators, focusing on key met-

Table 6.2: Trade-off analysis of numerical integrators for the 9DOF parafoil model.

Integrator	Runtime (s)	Smoothness	Stability	Suitability for Stiff Equations
`ode15s`	32.13	Smooth	Stable	Excellent
`ode23`	22.34	Moderately Smooth	Stable	Poor
`ode113`	28.15	Moderately Smooth	Stable	Good
`ode1`	23.41	Jagged	Unstable	Poor
`ode3`	34.86	Jagged	Unstable	Poor
`ode45`	Incomplete	Smooth	-	-

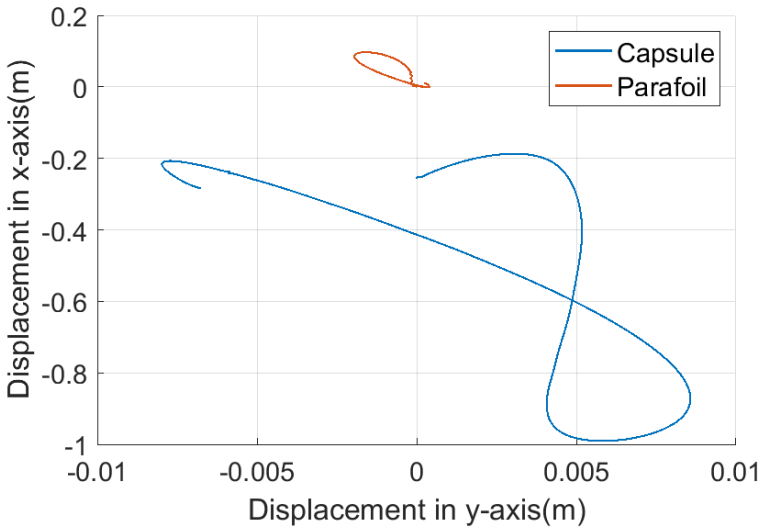

Figure 6.11: Lateral and Longitudinal Perturbation: Parafoil and Capsule centre of motion response in 100 seconds.

rics such as runtime, smoothness, stability, and suitability for stiff equations.
Table 6.2 summarizes the results of the analysis. The variable-step solver `ode15s` emerged as the most suitable choice. It demonstrated excellent stability and smoothness, particularly in capturing the parafoil's sensitive aerodynamic dynamics, while maintaining a reasonable runtime. `ode113` also showed stable results but was slightly slower than `ode15s` and less effective in handling the stiffness of the system.
While fixed-step integrators like `ode1` had faster runtimes, they introduced significant jaggedness and instability, making them unsuitable for the sensitivity and stability analyses required for this study. Similarly, `ode45`, although typically reliable, failed to complete the simulation due to the system's stiffness. Additional tuning of settings, such as reducing the time step or adjusting tolerances, could potentially improve `ode45`'s performance, but these changes would likely result in excessive computation times compared to `ode15s`.
For a more detailed comparison, including visual representations of α over time across integrators, please refer to Appendix B.

Verification Through Lateral and Longitudinal Perturbation Tests

As an additional verification step, a set of lateral and longitudinal perturbation tests were performed on the 9DOF parafoil-capsule model. In these tests, small "push" disturbances were applied to the system by giving the body an initial displacement velocity of $[2,1,1]$ m/s, shifting the parafoil and capsule centres of mass (COM) away from their hinge attachment point. Unlike the constant-force scenarios examined in other literature Mooij et al., 2003, here the focus was on transient displacements that allowed the system's intrinsic dynamics—governed by the modelled aerodynamic forces,

mass properties, and flexible coupling—to determine whether and how the bodies returned to equilibrium.

Figure 6.11 illustrate the trajectories of the parafoil and capsule COMs relative to the hinge following these disturbances for 100 seconds. Initially, the bodies were displaced longitudinally and/or laterally, causing them to deviate from their nominal equilibrium positions. As the simulation progressed, the combined effects of aerodynamic damping, gravitational forces, and the flexible suspension between the parafoil and capsule guided the system back toward a stable configuration.

Several observations can be drawn from these results:

- **Stable Equilibrium Recovery:** After the initial displacement, both the parafoil and the capsule gradually reduced their oscillatory excursions, converging toward steady equilibrium positions relative to the hinge point. This steady return to equilibrium indicates that the model's aerostructural coupling and inertial characteristics foster a stable static configuration, supporting the model's predictive fidelity.

- **Larger Displacement in x-axis:** The observed larger displacement in the x-direction compared to the y-direction can be attributed to the initial conditions set for the test. Specifically, the x-direction wind velocity was intentionally assigned a larger magnitude to replicate a scenario where wind-induced forces dominate in this axis. This setup aimed to isolate the aerodynamic behaviour of the parafoil under such conditions, providing a baseline for subsequent wind tests. The larger x-shift had the consequence of amplifying longitudinal oscillatory behaviour, which was also evident in later wind tests (chapter 7) where the angle of attack (α) oscillations exhibited a magnitude approximately twice that of sideslip (β) oscillations. These results highlight the sensitivity of parafoil dynamics to initial perturbations, particularly in the axis of greater aerodynamic loading.

- **Differentiated Responses of Parafoil and Capsule:** Although both bodies ultimately settle, the parafoil and capsule can trace distinct trajectories before reaching equilibrium. The parafoil's direct exposure to aerodynamic forces allows it to more rapidly dissipate perturbation energy. The capsule, suspended beneath the parafoil, experiences a delayed and sometimes more pronounced pendular response. These differing paths highlight the importance of modelling the hinge and flexible connections accurately, as they govern how disturbances are transmitted and damped within the system.

- **Physical Plausibility and Alignment with Literature:** While this test does not replicate the exact conditions of the referenced literature (which employed constant applied forces), the observed behaviour is qualitatively consistent with known parafoil dynamics. Systems with flexible suspensions and aerodynamic damping naturally return to an equilibrium configuration when subjected to small perturbations, provided that no sustained external forces are acting. The model's ability to "recover" from induced lateral and longitudinal shifts reinforces confidence in the implemented physics and numerical methods.

- **Usefulness for Controller Design and Operational Understanding:** By understanding how the parafoil-capsule system responds to transient lateral and longitudinal deviations, designers and operators can better anticipate its stability margins and damping characteristics. This insight can guide the development of control strategies that ensure quick and reliable return to stable flight conditions following gusts, release conditions, or other transient disturbances in real-world operations.

In sum, the perturbation tests serve as a meaningful verification exercise, demonstrating that the simulated system responds in a physically plausible manner to off-equilibrium conditions. The results complement the other verification and validation measures performed, collectively supporting the reliability and robustness of the 9DOF model.

6.3. Linearisation

The linearisation process is a critical step in analysing the stability characteristics of dynamic systems, particularly in aerospace dynamics, where natural frequencies and damping ratios are crucial for ensuring stability and control. By linearising the rotational dynamics of the 6DOF system about a nominal trajectory, the complex nonlinear equations of motion were reduced to a simplified state-space representation. This enabled direct stability analysis using eigenvalues and provided insights into the influence of key parameters.
Both analytical and numerical linearisation approaches were employed to validate the 6DOF system. The analytical linearised model involves deriving the state-space matrices directly from the system's equations of motion using symbolic or algebraic manipulation. This approach offers clarity by explicitly showing how individual parameters contribute to the system's dynamics, making it easier to interpret stability trends and sensitivities. On the other hand, the numerical linearised model uses perturbation techniques, where small changes are applied to the states and inputs, and the resulting system responses are numerically differentiated to construct the state-space matrices. This method is particularly useful for handling complex, nonlinear terms that are difficult or impractical to linearise analytically.
By combining these approaches, the analytical model provided insight into parameter sensitivities and dynamics, while the numerical model ensured that the effects of all nonlinearities were captured. Together, these methods thoroughly verified the behaviour of the 6DOF system, ensuring the linearised results aligned with the full nonlinear Simulink model.
Given the complexity of the 9DOF parafoil system, linearisation was not performed on it. Instead, the verification and validation of the 6DOF system were deemed sufficient to build confidence in the 9DOF model, as it was developed as an extension of the thoroughly tested nonlinear 6DOF system. This progressive approach—starting with the linearisation and simulation of the 6DOF system and advancing to the nonlinear 9DOF model—ensured a robust foundation for the final analysis.

6.3.1. Eigenvalue Analysis

Linearising a model enables the use of eigenvalue analysis to determine key stability parameters such as the natural frequency (ω_n), which represents the oscillation rate of the system, and the damping ratio (ζ), which quantifies how quickly oscillations decay over time, analytically. This can then be used to be compared with the same outputs obtained numerically as a form of verification.
The system consists of two mass points connected by a rigid body that rotates around a hinge. Unlike a simple single mass-point system, the actual equations of motion are calculated around this hinge point. For this specific test:

- The system is operating at a fixed altitude.
- The translational velocity norm remains constant.
- The only initial perturbation is a non-zero angle of attack α.
- All other initial rotational rates and angles are set to zero, meaning the motion occurs primarily in the axis corresponding to α.
- We are only considering rotational dynamics, so the primary variables of interest are the pitch rate q and angle of attack α.

The key equations governing the rotational dynamics of the system are the following:
The rate of change of the pitch rate q is governed by the following equation:

$$\dot{q} = \frac{M_y}{I_{yy}} + (I_{zz} - I_{xx})pr \tag{6.10}$$

The rate of change of the angle of attack α is given by:

$$\dot{\alpha} = q - (p\cos\alpha + r\sin\alpha)\tan\beta - \frac{L - mg\cos\gamma\cos\sigma}{mV\cos\beta} \tag{6.11}$$

To perform the linearisation, we use the following approach:

$$\Delta \dot{x} = A\Delta x + B\Delta u \tag{6.12}$$

where Δx is the state vector, Δu is the input vector, and **A** is the system matrix, which is constructed from the partial derivatives of the nonlinear equations of motion. It is crucial to evaluate the entries of the **A** at the equilibrium point (x_0, u_0), where x_0 is the equilibrium state and u_0 is the equilibrium input. This ensures that the linearised model accurately represents the system dynamics near the equilibrium.
The entries of **A** are derived as the partial derivatives of the state equations with respect to the state variables, evaluated at $(x = x_0, u = u_0)$:

$$A = \begin{bmatrix} \frac{\partial f_1}{\partial x_1} & \frac{\partial f_1}{\partial x_2} & \cdots & \frac{\partial f_1}{\partial x_n} \\ \vdots & \vdots & \ddots & \vdots \\ \frac{\partial f_n}{\partial x_1} & \frac{\partial f_n}{\partial x_2} & \cdots & \frac{\partial f_n}{\partial x_n} \end{bmatrix} \Bigg|_{x=x_0, u=u_0} \tag{6.13}$$

For the simplified analysis, we focus on the 6×6 A-matrix corresponding to the rotational analysis:

$$A = \begin{bmatrix} 0 & 0 & 0 & 0 & a_{p\beta} & 0 \\ 0 & 0 & 0 & a_{q\alpha} & 0 & 0 \\ 0 & 0 & 0 & 0 & a_{r\beta} & 0 \\ 0 & a_{\alpha q} & 0 & a_{\alpha\alpha} & 0 & 0 \\ a_{\beta p} & 0 & a_{\beta r} & 0 & a_{\beta\beta} & a_{\beta\sigma} \\ a_{\sigma p} & 0 & a_{\sigma r} & a_{\sigma\alpha} & a_{\sigma\beta} & a_{\sigma\sigma} \end{bmatrix} \tag{6.14}$$

The relevant terms are:

$$a_{q\alpha} = \frac{\partial C_m}{\partial \alpha} \cdot \frac{\bar{q}_0 S_{\text{ref}} c_{\text{ref}}}{I_{yy}} \tag{6.15}$$

$$a_{\alpha q} = 1 \tag{6.16}$$

$$a_{\alpha\alpha} = -\frac{\partial C_L}{\partial \alpha} \cdot \frac{\bar{q}_0 S_{\text{ref}}}{m V_0} \tag{6.17}$$

$$a_{p\beta} = \frac{1}{I_{xx}} \cdot \frac{\partial C_l}{\partial \beta} \cdot \bar{q}_0 S_{\text{ref}} b_{\text{ref}} \tag{6.18}$$

$$a_{r\beta} = \frac{1}{I_{zz}} \cdot \frac{\partial C_n}{\partial \beta} \cdot \bar{q}_0 S_{\text{ref}} b_{\text{ref}} \tag{6.19}$$

$$a_{\beta\beta} = -\frac{1}{m V_0} \cdot \frac{\partial C_s}{\partial \beta} \cdot \bar{q}_0 S_{\text{ref}} \tag{6.20}$$

$$a_{\sigma\alpha} = \tan\gamma_0 \cdot \sin\sigma_0 \cdot \frac{\partial C_L}{\partial \alpha} \cdot \frac{\bar{q}_0 S_{\text{ref}}}{m V_0} \tag{6.21}$$

$$a_{\sigma\beta} = \tan\gamma_0 \cdot \cos\sigma_0 \cdot \frac{\partial C_s}{\partial \beta} \cdot \frac{\bar{q}_0 S_{\text{ref}}}{m V_0} - \frac{L_0}{m V_0} + \frac{g_0}{V_0} \cos\gamma_0 \cos\sigma_0 \tag{6.22}$$

$$a_{\sigma\sigma} = \tan\gamma_0 \cdot \cos\sigma_0 \cdot \frac{L_0}{m V_0} \tag{6.23}$$

For the purposes of the linearisation study, which was carried out primarily as a verification step, the simpler parachute model was utilized. This model was chosen due to its straightforward dynamics, making it easier to verify and interpret compared to the more complex parafoil system. In this initial study, deviations in β (sideslip angle) and σ (bank angle) were not considered. These angles

exhibit significantly smaller deviations compared to α (angle of attack) under the tested conditions, and their effects were deemed negligible for this verification process. Consequently, only the terms related to α were retained in the final analysis, resulting in the following reduced A-matrix:

$$A = \begin{bmatrix} 0 & 0 & 0 & 0 & 0 & 0 \\ 0 & 0 & 0 & \frac{dC_{m\alpha} \cdot qS \cdot c_{\text{ref}}}{I_{yy}} & 0 & 0 \\ 0 & 0 & 0 & 0 & 0 & 0 \\ 0 & 1 & 0 & -\frac{dC_{L_\alpha} \cdot qS}{mV} & 0 & 0 \\ 0 & 0 & 0 & 0 & 0 & 0 \\ 0 & 0 & 0 & 0 & 0 & 0 \end{bmatrix} \tag{6.24}$$

6.3.2. Comparison to Nonlinear Numerical Model

To improve alignment with the observed behaviour in the numerical model, modifications were made to the calculation of the A-matrix and aerodynamic derivatives. In the Simulink numerical model, forces and moments are first calculated individually for the parafoil and capsule before being unified into the equations of motion. However, in the linearisation process, the concept of the single rigid body being modelled as two distinct mass points connected by a massless rigid bar required additional assumptions. Moment components were multiplied directly by the moment arms while calculating the δC_m for each body when getting all the aerodynamic deviations for each point in the linearisation. This adjustment ensures consistency with the numerical model, where moments are accumulated directly without averaging.

The updated aerodynamic derivatives for the relevant terms in the A-matrix are as follows:

$$a_{q\alpha} = \frac{\frac{\delta C_m}{\delta \alpha_p} \bar{q} S_{ref_p}}{I_{yy}} + \frac{\frac{\delta C_m}{\delta \alpha_r} \cdot \bar{q} S_{ref_r}}{I_{yy}} \tag{6.25}$$

$$a_{\alpha q} = 1.0 \tag{6.26}$$

$$a_{\alpha\alpha} = 0.5 \cdot \left(\frac{\frac{\delta C_L}{\delta \alpha_p} \bar{q} S_{ref_p}}{m V_p} + \frac{\frac{\delta C_L}{\delta \alpha_r} \bar{q} S_{ref_r}}{m V_r} \right) \tag{6.27}$$

In the `AeroPoint` script, the moment arm terms are defined as:

$$\delta \mathbf{C_{m_p}} = \mathbf{r_{p\_cp}} \times \mathbf{C_{AB_p}} \tag{6.28}$$

$$\delta \mathbf{C_{m_r}} = \mathbf{r_{r\_cp}} \times \mathbf{C_{AB_r}} \tag{6.29}$$

Using the reduced **A**, eigenvalue analysis was performed to determine the system's ω_n and ζ. For the parachute model, the eigenvalues predicted periodic oscillations with a natural frequency of approximately 5.06 rad/s and a damping ratio of 0.1046, matching the results from the nonlinear simulations.

To assess the stability and dynamic behaviour of the parafoil system, the same analytical expressions previously developed for the linearised parachute model was used, adapting them by substituting the parafoil-specific values for parameters such as Cm_α and CL_α. This approach provided eigenvalues of approximately -11 and -0.58 for the parafoil, both of which are real and negative, confirming aperiodic (non-oscillatory) motion.

The dominance of the smaller eigenvalue (-0.58) indicates a slower decay rate, which explains the more gradual settling behaviour observed in the 6DOF and 9DOF parafoil simulations. This slow decay rate, combined with the lack of oscillatory (imaginary) components, aligns well with the characteristic aperiodic response seen in both models. Therefore, the analytical eigenvalue results not only support the simulation observations but also provide insight into the rate at which the parafoil system returns to equilibrium after a disturbance.

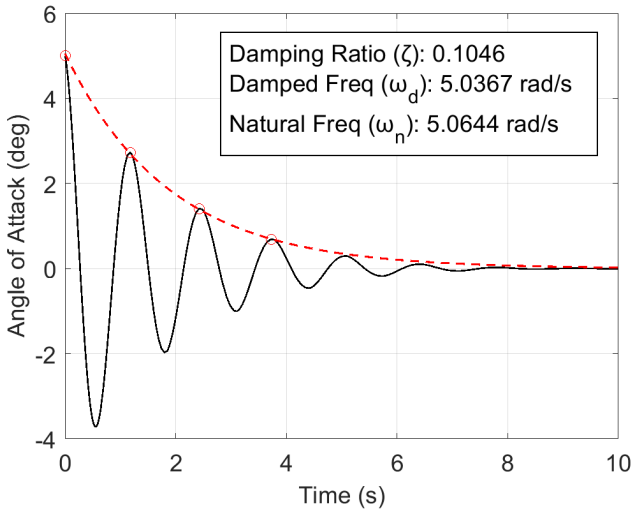

Figure 6.12: Comparison of eigenvalue analysis results with nonlinear numerical model outputs.

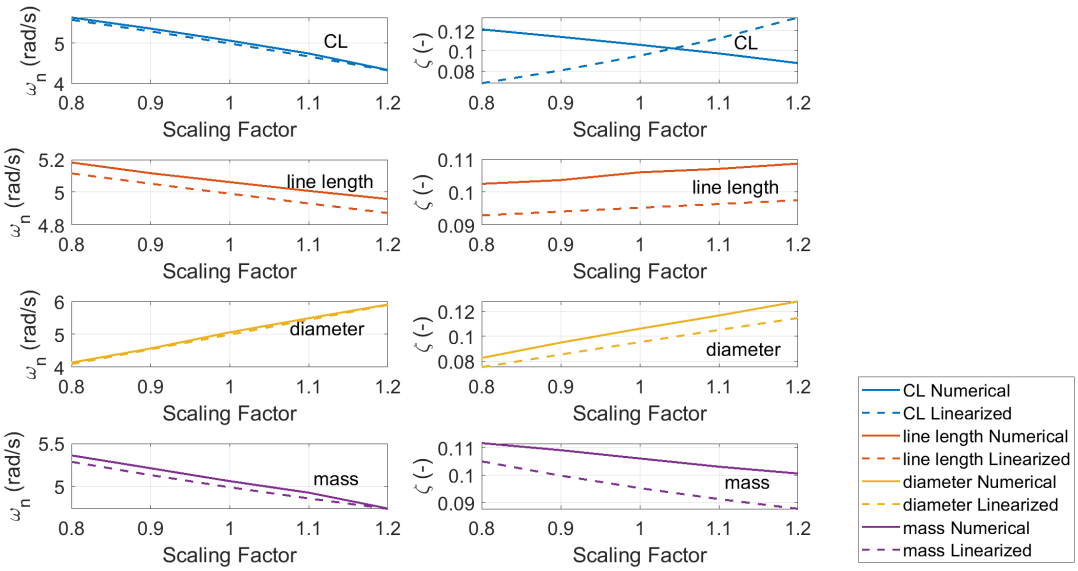

Figure 6.13: Individual parameter-by-parameter sensitivity analysis conducted and compared between the 6DOF linear parachute model (dashed lines) and the 6DOF non-linear parachute model (solid lines).

6.3.3. Preliminary Sensitivity Analysis

The nominal values of ω_n and ζ in the linearised model more closely match those observed in the numerical simulation. However, when the lift coefficient sensitivity, C_L/α, is increased, the linearised model exhibits an inverse effect on the damping ratio compared to the numerical results. In the linearised model, increasing C_L reduces ω_n but also increases ζ, whereas the numerical model shows both values decreasing.

This discrepancy arises from limitations inherent in the linearised model, where assumptions and simplifications, such as constant aerodynamic forces, restrict the ability to capture all nonlinear interactions. While the linearised model retains sensitivity to changes in C_L magnitude, the observed discrepancy in the damping ratio (ζ) stems from the relationship between the real part of the eigen-

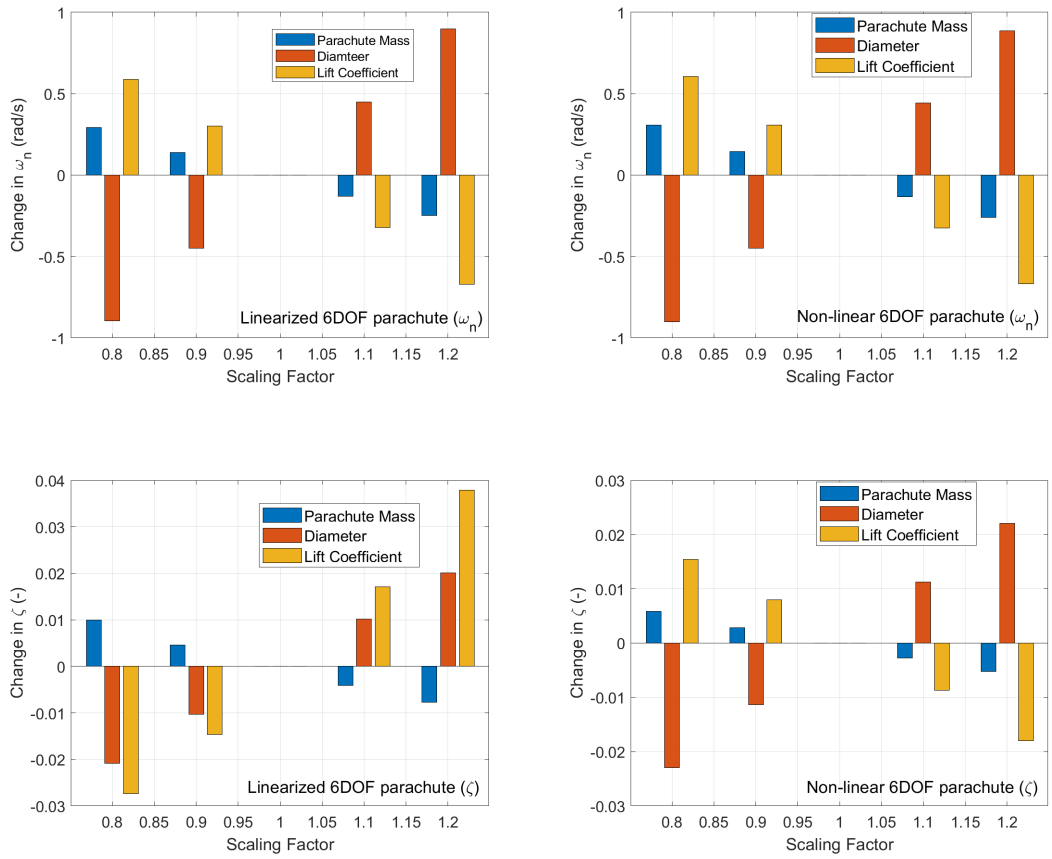

Figure 6.15: Gradient-Based Sensitivity Analysis of the 6DOF Parachute with the plots on the left showing the linearised model results and the plots on the right showing non-linear model results

value (Re) and the natural frequency (ω_n). Specifically, the damping ratio is given by:

$$\zeta = -\frac{\text{Re}}{\omega_n}, \tag{6.30}$$

where Re represents the real part of the eigenvalue, which determines the decay rate of oscillations, and ω_n is the natural frequency, which reflects the speed of oscillatory motion. As C_L increases, ω_n decreases more rapidly than Re, resulting in an overall increase in ζ predicted by the linearised model.

The linearised model's sensitivity gradient in terms of parameter magnitude provides valuable insight but does not fully reflect the nonlinear dynamics present in the numerical model. Therefore, the findings highlight a key limitation of linearisation in capturing complex parameter interactions, justifying reliance on the numerical model for final stability conclusions.

This limitation is acknowledged as an acceptable trade-off for the purposes of this thesis, providing approximate stability trends despite directional discrepancies in specific cases.

The sensitivity analysis results, encompassing both individual parameter variations and combined effects, provide critical insights into the stability behaviour of the parachute system. The analysis of individual parameter changes reveals that the lift coefficient (C_L) has the most significant impact on the natural frequency (ω_n) across both linearised and nonlinear models. Increasing C_L consistently reduces ω_n, reflecting the expected effect of larger aerodynamic forces slowing the system's oscillatory response. However, the damping ratio (ζ) shows contrasting trends: while the linearised model predicts an increase in ζ with C_L, the nonlinear model indicates a decrease. This divergence under-

scores the inherent limitations of the linearised approach, particularly its inability to fully capture nonlinear aerodynamic interactions.
The influence of parachute mass (m) and diameter (D_0) is also evident, though less pronounced compared to C_L. Increasing the parachute mass results in a moderate reduction in ω_n, primarily due to the added inertia, while the effect on ζ is relatively minor. Similarly, increasing D_0 lowers ω_n by enlarging the aerodynamic area but introduces only subtle changes to ζ. Line length (L_s), on the other hand, exhibits the weakest sensitivity among the parameters analysed. This suggests that geometrical coupling effects, while present, are secondary compared to the dominant role of aerodynamic forces in driving stability behaviour.
In contrast, the combined parameter variation analysis highlights the complex interactions that arise when multiple parameters are varied simultaneously. The natural frequency is particularly sensitive to combinations involving C_L and D_0, with larger variations observed in the nonlinear model. This emphasizes the strong dependence of stability on aerodynamic forces and the geometry of the system. The damping ratio, however, exhibits a more nuanced behaviour in the nonlinear model, particularly under high C_L conditions. While the linearised model captures general trends, it fails to replicate the detailed interactions between parameters, particularly when aerodynamic coupling effects dominate.
These findings underscore the limitations of the linearised model in capturing the full complexity of parameter interactions. The assumptions of constant aerodynamic forces and simplified dynamics restrict its ability to reflect the nonlinear behaviour observed in the numerical model. However, the linearised model still provides valuable preliminary insights, particularly in identifying the dominant parameters and their general trends. Its computational efficiency makes it a useful tool for early-stage analysis, even if it lacks the fidelity required for detailed stability assessments.
Overall, the results demonstrate the critical influence of C_L on both stability metrics, with mass and diameter playing secondary but notable roles. The nonlinear model's ability to capture cross-parameter interactions reinforces its importance as the primary tool for assessing stability in complex systems. These analyses not only validate the approach used in this study but also provide a foundation for comparing the stability behaviour of parachute and parafoil systems, guiding design optimisations for Titan descent missions.

6.4. Transition to Sensitivity Analysis

The verification and validation results presented in this chapter establish a solid foundation for the analyses explored in Chapter 7. By confirming the physical accuracy and computational reliability of the models, these tests ensure that subsequent sensitivity and wind analyses are based on trustworthy and well-understood systems. The subsystem tests, energy conservation results, and angular momentum validations collectively provide confidence that the models can capture both the fundamental dynamics and the nuanced effects of parameter variations and environmental forces. The next chapter builds on this groundwork, delving into the dynamic behaviour of the parafoil and capsule under varying conditions to answer key research questions regarding stability and adaptability.

7

Results and Analysis

The results presented in this chapter address the primary research question outlined in the introduction: *To what extent can high-fidelity dynamic modelling enhance the understanding of parafoil stability and performance for planetary landings?*
Specifically, this chapter focuses on two critical analyses:

1. **Sensitivity analysis**: Identifying the parameters most significantly influencing the stability and dynamic behaviour of parafoil systems during descent, with particular attention to *longitudinal stability*.

2. **Wind tests**: Evaluating the system's response to realistic external disturbances, including steady-state and turbulent winds, with an emphasis on both *longitudinal* and *lateral stability*.

These analyses build upon the verification efforts described in chapter 6, transitioning from foundational verification tests to a detailed exploration of how key environmental and design parameters impact the parafoil's behaviour. Together, these results aim to provide actionable insights into the parafoil's stability and control under Titan-like conditions.

Sensitivity Analysis

The sensitivity analysis focuses on oscillations in the angle of attack (α), a critical metric for longitudinal stability. During descent, the parafoil's velocity predominantly lies in the x-z plane as the initial velocity is also applied in this plane, resulting in significant oscillations in α, while oscillations in the sideslip angle (β) remain negligible unless external disturbances, such as winds or initial velocities in the y-direction, are introduced. Even under scenarios with y-direction velocity components, oscillations in α are up to two orders of magnitude larger than those in β for the parafoil in this study. Therefore, in this study, importance is placed on α as a key output parameter for assessing stability, although lateral stability is also later assessed during wind testing.
In traditional parachute systems, periodic motion often allows stability characterization using natural frequency and damping ratios. However, the parafoil system exhibited *aperiodic motion* during settling, necessitating alternative output metrics. The maximum amplitude of the angle of attack oscillation was selected as the primary stability metric for the sensitivity analysis. This choice is motivated by its direct relevance to aerodynamic performance and, therefore, to any controlled efforts in the descent of the parafoil. Excessive oscillations in α could lead to inefficiencies or instabilities, particularly in Titan's dense atmosphere, where aerodynamic forces dominate.
The sensitivity analysis in this section follows a structured approach to systematically evaluate the influence of key parameters on the system's dynamics. First, individual parameter sensitivity tests are performed on the 6DOF model to identify the most influential parameters. These insights are then applied to the 9DOF parafoil and capsule model, allowing for a comparative analysis of the two systems. Next, a combined sensitivity analysis is conducted using the parameters identified in the

individual tests. This combined analysis employs heatmaps, ANOVA, and gradient sensitivity methods to evaluate the effects of parameter interactions, starting with the 6DOF model and proceeding to the 9DOF parafoil and capsule. The results are analysed and compared at each stage, providing a comprehensive understanding of parameter sensitivities and their combined effects across both models.

Wind Tests

In addition to longitudinal stability, lateral stability is considered during wind tests. These tests introduce realistic disturbances in the y direction, simulating steady-state and turbulent wind profiles to assess the parafoil's behaviour under complex environmental conditions. The results of these wind tests provide a complementary perspective to the sensitivity analysis by highlighting the interplay between aerodynamic forces and external perturbations.

By addressing both sensitivity and wind analyses, this chapter provides critical insights into the parafoil's stability and dynamic behaviour, forming the foundation for the discussions and conclusions in subsequent chapters.

7.1. Sensitivity Analysis: Individual Effects

The sensitivity analysis explores how key parameters influence the oscillatory behaviour of the system, focusing on the angle of attack (α). A preliminary test was conducted by varying a wide range of parameters (e.g., mass, geometry, aerodynamic coefficients, atmospheric constants) from −20% to +20% around their nominal values. Through this process, five parameters were identified as having the most significant influence on the peak oscillation amplitude of α. These parameters were selected because they directly govern the fundamental aerodynamic and inertial characteristics of the system:

- **Payload mass** ($m_{payload}$): Influences the system's inertia and determines how quickly it can pitch up or down in response to aerodynamic forces.
- **Chord length** (c): Affects the lift generated per unit angle of attack, influencing the magnitude of aerodynamic moments during oscillations.
- **Lift-curve slope** (C_{L_α}): Governs the sensitivity of aerodynamic forces to changes in α, impacting oscillation amplitudes.
- **Zero-lift drag coefficient** (C_{D0}): Sets the baseline drag, affecting energy dissipation and pitch response.
- **Air density** (ρ): Scales aerodynamic forces, amplifying or diminishing their effects on stability.

These parameters produced the highest percentage deviations in the peak oscillation amplitude of α during the initial parameter sweep. Focusing on these parameters provides actionable insights into the aspects of system design and environment most critical to the parafoil's stability and controllability. The detailed results of the sensitivity analysis are presented in the subsequent sections.

7.1.1. Introduction of Overshoot as a Metric

Transient aerodynamic behaviours in parafoil dynamics require careful quantification to ensure stability and performance during descent. Among various stability metrics, overshoot—the maximum deviation from equilibrium following a disturbance—emerges as a localized and physically meaningful measure for assessing these transient responses. This subsection introduces the concept of overshoot, its relevance to parafoil dynamics, and its integration into the sensitivity analysis framework.

Theoretical Foundation and Control Theory Context

The concept of overshoot is widely recognized in control systems as a critical metric for evaluating transient responses. Overshoot measures the maximum deviation of a system from its equilibrium point following a disturbance, as commonly illustrated in standard second-order system responses. In parafoil dynamics, transient rotational and aerodynamic responses are dominant, making overshoot a relevant metric for characterizing system stability. For parafoil systems, the maximum angle of attack (α) during oscillations is analogous to overshoot in control systems. This metric captures the peak transient behaviour, providing insights into aerodynamic efficiency and stability that are not directly inferred from global metrics like natural frequency (ω_n) and damping ratio (ζ).

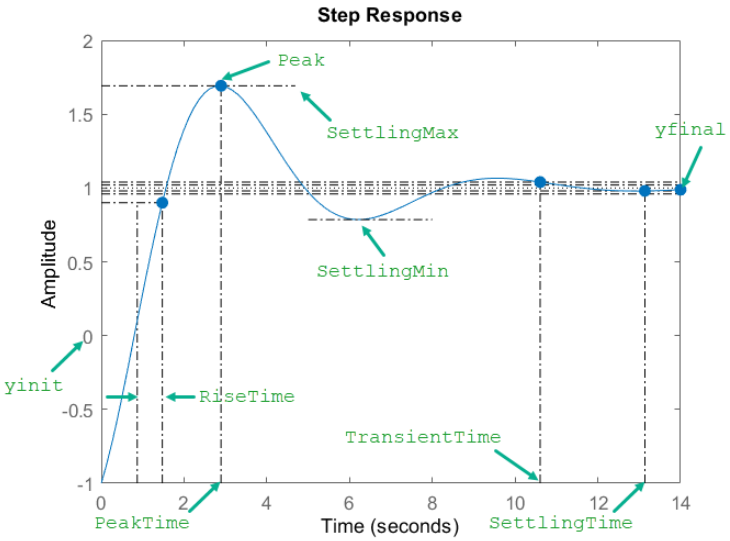

Figure 7.1: Step response of a second-order system, illustrating overshoot, rise time, and settling time.

Preliminary Comparison of Stability Metrics

To justify the use of overshoot as the primary metric, a comparative analysis was conducted, considering natural frequency, damping ratio, and maximum α. Overshoot demonstrated greater sensitivity to variations in key system parameters, such as mass and aerodynamic coefficients, compared to ω_n and ζ.

To justify the use of overshoot as the primary metric, a comparative analysis was conducted, considering natural frequency, damping ratio, and maximum α. Overshoot demonstrated greater sensitivity to variations in key system parameters, such as mass and aerodynamic coefficients, compared to ω_n and ζ. This observation highlights overshoot as a superior differentiator for sensitivity analysis, particularly in systems like parafoils where transient aerodynamic behaviours play a critical role. Further details on the inconsistencies observed with ω_n and ζ, and the rationale for using overshoot, are provided in Appendix C

Physical Interpretation of Maximum Angle of Attack

The maximum angle of attack, or overshoot, reflects the peak rotational response of the parafoil following a disturbance. This metric provides valuable aerodynamic insights:

- **Larger Overshoot:** Indicates weaker aerodynamic damping or insufficient moment control, potentially causing the parafoil to exceed safe operational limits or experience structural stress.
- **Smaller Overshoot:** Reflects stronger damping and tighter aerodynamic coupling, indicative of a system optimized for stability and control.

In Titan's dense atmosphere, where large transient responses can destabilize the parafoil or reduce descent efficiency, overshoot quantifies the dynamic range and susceptibility to instability effectively.

Integrating Overshoot into Sensitivity Analysis

Overshoot, measured by the maximum amplitude of α, serves as the primary metric for the sensitivity analysis. By focusing on overshoot, the analysis transitions from generalized stability trends to assessing specific transient aerodynamic behaviours, offering actionable insights for system design and optimization.

7.1.2. Results for the 6DOF Model

The individual sensitivity tests involved scaling each parameter by factors of 0.8, 0.9, 1.0, 1.1, and 1.2, corresponding to −20% to +20% variations. The results, shown in Figure 7.2, highlight the system's transient response to these variations. Each observation is accompanied by a physical interpretation, providing insight into the underlying aerodynamic and dynamic effects.

The sensitivity results for the 6DOF model are summarized below, focusing on how each parameter variation influences the peak α, stabilization time, and overall system dynamics.

$m_{payload}$**:** Increases in payload mass result in higher peak angles of attack. Physically, a heavier payload increases the system's total inertia, making it more resistant to rapid changes in pitch attitude. When a disturbance occurs, the system must generate higher aerodynamic moments to overcome this inertia. As a result, the angle of attack tends to overshoot more before settling, thus raising the peak. Conversely, reducing the payload mass decreases the system's inertia, enabling it to respond more rapidly and reducing the maximum pitch excursion (Ward et al. (2012)).

c**:** Changing the chord length modifies the parafoil's reference area and thus its aerodynamic force generation capability. Increasing the chord length slightly raises the peak α, as a larger lifting surface generates more lift for the same change in angle of attack. This heightened aerodynamic responsiveness can lead to a more pronounced initial overshoot. Conversely, decreasing the chord reduces the lifting surface and the force generated per unit change in α, attenuating the peak oscillation amplitude.

C_{D0}**:** The C_{D0} establishes the baseline drag the system experiences. Increasing C_{D0} while maintaining the same initial conditions results in higher drag forces, which resist the forward motion and amplify the initial pitch-up disturbance (Slegers (2003)). This causes the system to experience a larger initial peak in α before settling. Conversely, reducing C_{D0} diminishes the drag force, allowing the system to pitch more gradually and reducing the peak α. The system also tends to settle at different equilibrium angles depending on the drag magnitude, with higher drag promoting higher equilibrium pitch angles.

C_{L_α}**:** C_{L_α} determines how strongly lift responds to changes in α. In this analysis, C_{L_α} was varied while keeping the initial velocity and other conditions constant. Increasing C_{L_α} generates more lift for a given α, which helps the system reach equilibrium faster. As a result, the peak α is lower, and the system settles more quickly into a stable orientation. Conversely, reducing C_{L_α} results in less lift for the same initial conditions, causing the parafoil to deviate further in the pitching direction before settling. This highlights that higher lift forces promote stability by limiting the initial pitch excursion and accelerating the settling process.

ρ**:** ρ directly affects the dynamic pressure, which in turn influences the lift and drag forces experienced by the parafoil. An increase in ρ amplifies these forces, enhancing the parafoil's ability to stabilize after perturbations (Leishman, 2023). When ρ is increased while maintaining the same initial conditions, the amplified lift forces enable the system to stabilize faster, reducing the peak α. The higher aerodynamic forces counteract the pitching disturbance more effectively, resulting in a quicker return to equilibrium. Conversely, lower ρ weakens the aerodynamic forces, making the system less capable of counteracting the disturbance, leading to a higher peak α and slower stabilization. Additionally, changes in ρ influence the overall equilibrium pitch angle (α), with higher densities leading to lower equilibrium angles and lower densities leading to higher equilibrium angles.

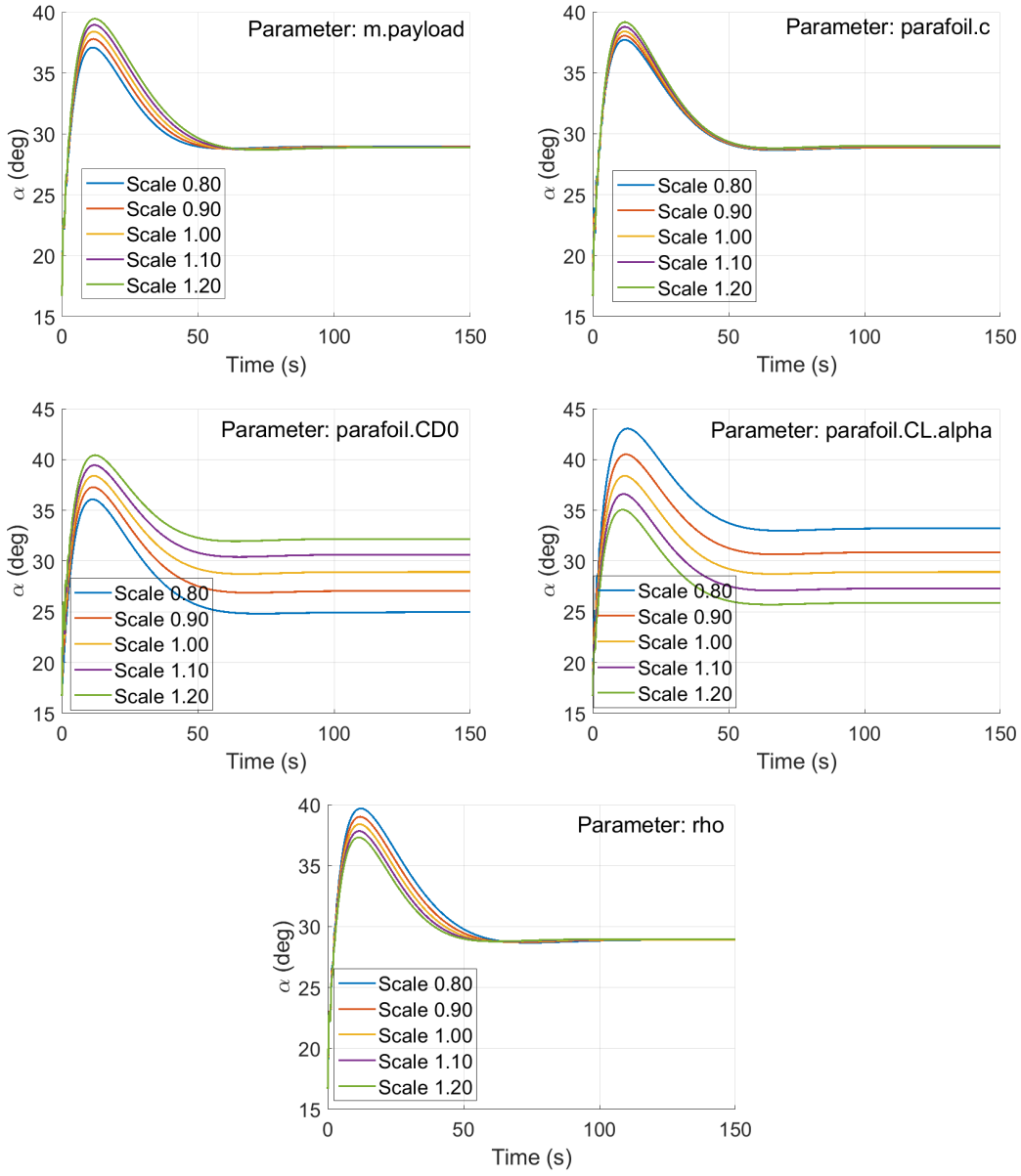

Figure 7.2: Sensitivity analysis of different parameters on the angle of attack, α, showing the 6DOF system's response under varying scales for each parameter. The parameters analysed include $m_{payload}$, c, C_{D0}, C_{L_α} and ρ.

The interplay between lift, drag, and inertia determines the system's oscillatory response. Higher C_{L_α} and ρ enhance stability by reducing the initial pitch deviation and accelerating the settling process. In contrast, higher drag forces and lower lift forces result in larger initial deviations and slower stabilization. These dynamics underscore the importance of balancing aerodynamic coefficients to achieve desired stability characteristics.

7.1.3. Results for the 9DOF Model

The 9DOF model introduces flexible coupling between the parafoil and capsule, enabling independent rotational motion. This dynamic interaction results in distinct responses for each component, as illustrated in Figures 7.3 and 7.4. These figures present the sensitivity analysis results for the

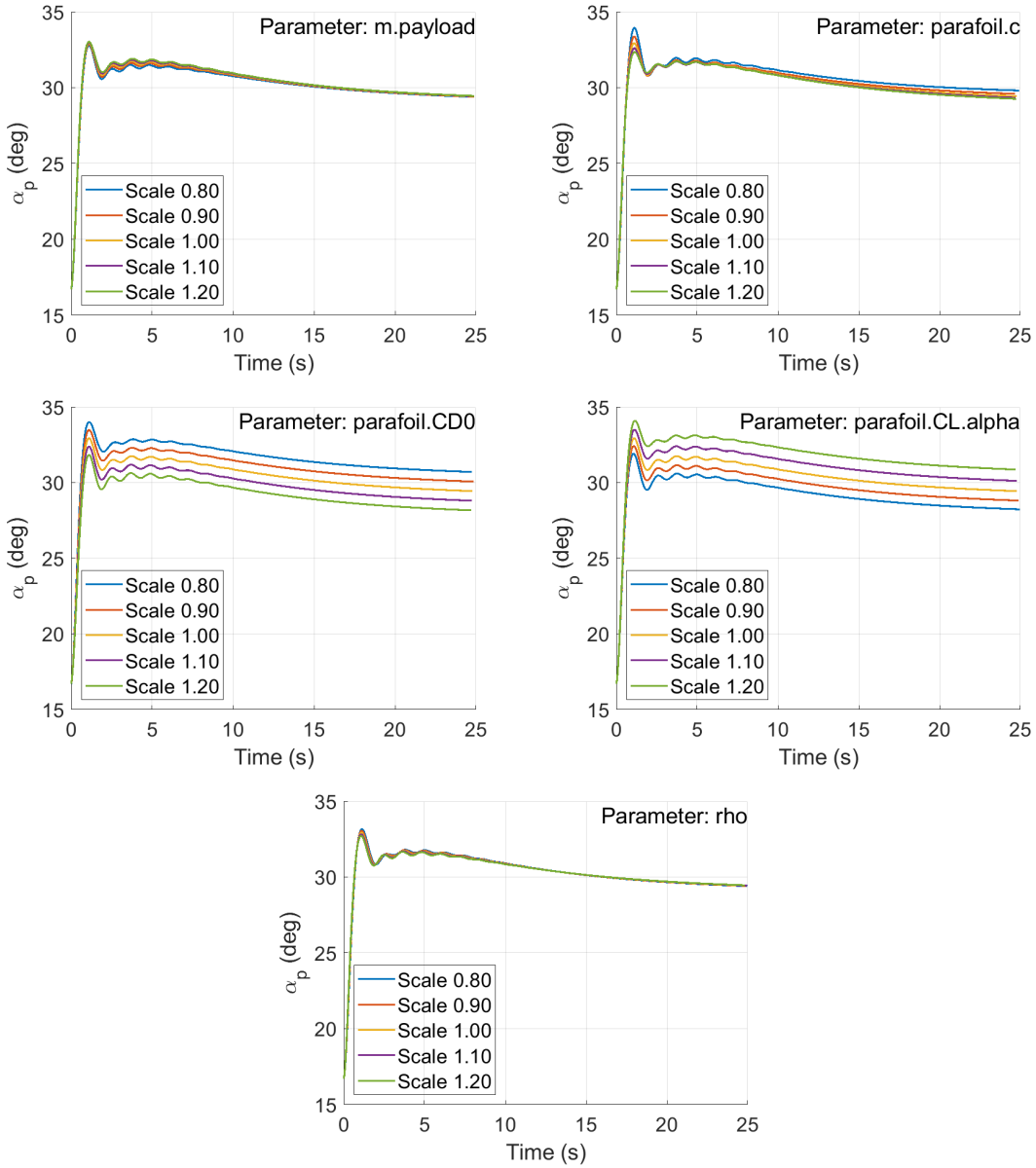

Figure 7.3: Sensitivity analysis for the parafoil of the 9DOF system: the effect of scaling each parameter on α_p (angle of attack for the parafoil) over time, up to around 25 seconds. Each plot represents a different parameter with five scaling variations, showing distinct oscillatory responses.

parafoil (α_p) and capsule (α_s), respectively, for key parameters.

- m_{payload}**:** Increasing m_{payload} leads to a higher peak α_p. The additional inertia causes the parafoil to pitch up more significantly before stabilizing. Conversely, reducing m_{payload} results in a lower peak due to reduced inertia.
- c**:** Increasing c slightly raises the peak α_p, as a larger chord increases the aerodynamic moment. The effect is moderate, with the parafoil quickly stabilizing due to its ability to adjust pitch independently.
- C_{D0}**:** Higher C_{D0} decreases the peak α_p by increasing drag, which dampens the pitch response. This effect aligns with the trends observed in the 6DOF model.

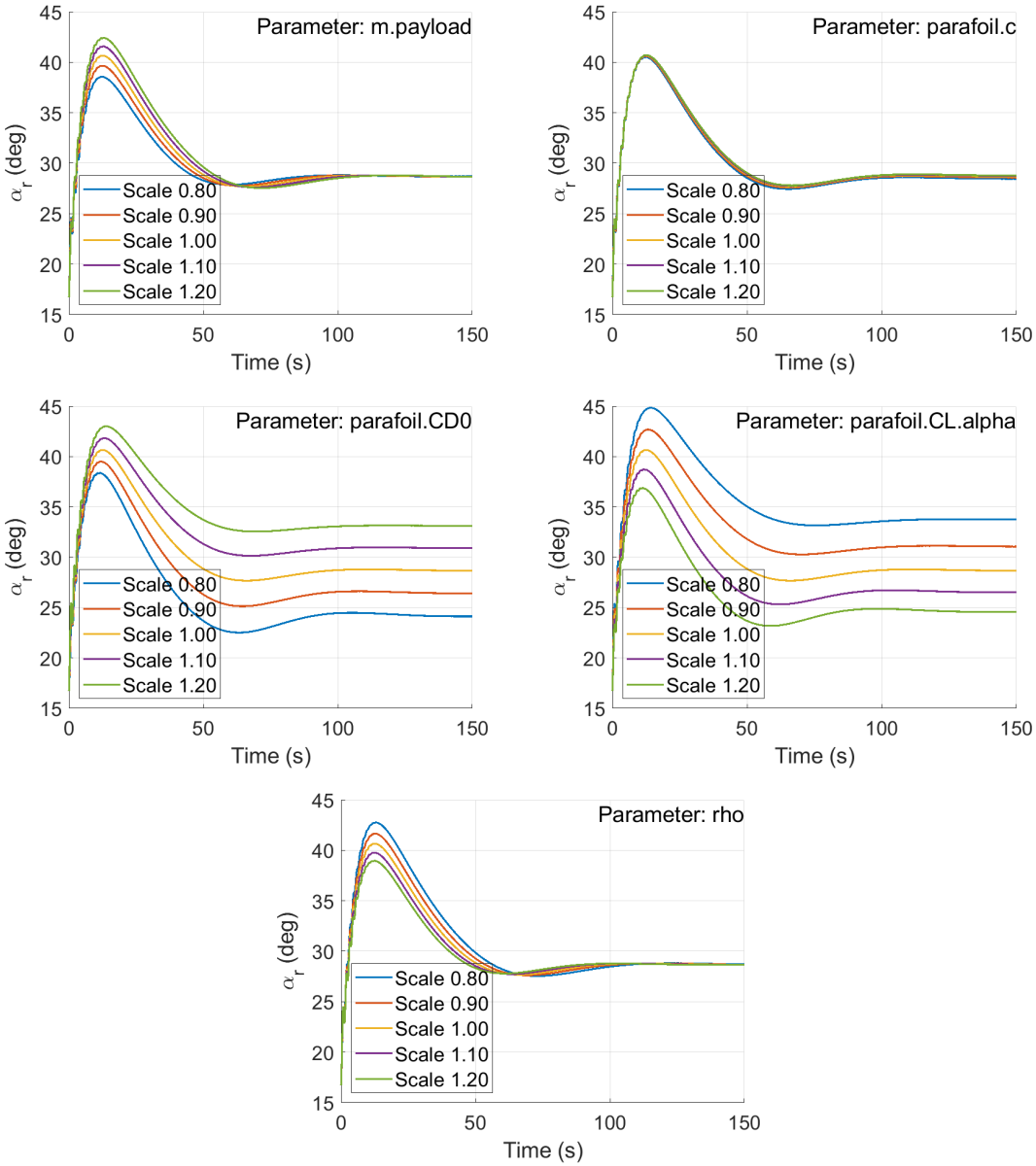

Figure 7.4: Sensitivity analysis for the capsule of the 9DOF system: the effect of scaling each parameter on α_s (angle of attack for the capsule) over time, shown up to around 150 seconds. Each plot represents a different parameter with five scaling variations, indicating the influence of each parameter on the oscillatory and stabilizing behaviour of the capsule.

- $C_{L\alpha}$**:** Increasing $C_{L\alpha}$ amplifies the peak α_p. The greater lift sensitivity causes the parafoil to respond more vigorously to pitch disturbances, resulting in a higher initial peak.
- ρ**:** Higher ρ increases aerodynamic forces, leading to a lower peak α_p due to the stronger initial lift counteracting the pitch-up motion.

Influence on the Capsule (α_s) Figure 7.4 illustrates the capsule's response to parameter variations. The trends closely resemble those observed in the 6DOF system:

- $m_{\textbf{payload}}$**:** Increasing m_{payload} results in a higher peak α_s, as the capsule's inertia amplifies its pitch excursion. This trend is consistent with the 6DOF results.

Table 7.1: Percentage deviation in peak oscillation of angle of attack (α) for the 6DOF system, the parafoil (α_p), and the capsule (α_s) of the 9DOF system.

Parameter	6DOF (%)	9DOF Parafoil (%)	9DOF Capsule (%)
$m_{payload}$	6.25	0.67	9.51
c	3.81	4.82	0.49
C_{D0}	11.46	6.57	11.41
$C_{L\alpha}$	20.92	6.61	19.56
ρ	6.12	1.34	9.33

- **c:** Changes in c have a minimal effect on the capsule's oscillation. The flexible coupling allows the capsule to align with the parafoil's pitch without significant deviation.
- **C_{D0}:** Higher C_{D0} increases drag, leading to a higher peak α_s due to the delayed damping effect. This trend is consistent with the 6DOF model.
- **$C_{L\alpha}$:** Increasing $C_{L\alpha}$ raises the peak α_s, reflecting the capsule's sensitivity to the parafoil's lift-induced pitch motion.
- **ρ:** Higher ρ results in a higher peak α_s, consistent with the 6DOF behaviour where increased aerodynamic forces amplify the capsule's oscillation.

7.1.4. Comparison

The sensitivity analysis of the 6DOF and 9DOF systems reveals significant differences in their dynamic responses due to the flexible coupling introduced in the 9DOF model. Table 7.1 summarizes the percentage deviations in peak oscillations of the angle of attack (α) for the 6DOF system, the parafoil (α_p), and the capsule (α_s) of the 9DOF system, providing a consolidated view of the parameter effects across all configurations.

The 9DOF analysis reveals an intriguing distinction: while increasing $C_{L\alpha}$ and ρ typically reduces the peak α_p for the parafoil, these same changes increase the peak α_s for the capsule. This discrepancy highlights the influence of the payload dynamics on the overall system. The capsule's inertia and its suspended position beneath the parafoil cause it to dominate the system's dynamic behaviour, as observed in the 6DOF model.

In the 6DOF model, parameters like payload mass (m_{payload}), chord length (C), zero-lift drag coefficient (C_{D0}), lift-curve slope (C_{L_α}), and air density (ρ) affect the system uniformly due to the rigid coupling between the parafoil and capsule. In contrast, the 9DOF model demonstrates a redistribution of sensitivity, with the parafoil and capsule exhibiting distinct responses. The payload mass variations have a muted effect on the parafoil but a significantly amplified impact on the capsule, reflecting the redistribution of inertial forces through the suspension system. Similarly, aerodynamic parameters such as C_{L_α} and C_{D0} show reduced sensitivity for the parafoil, as it stabilizes itself through direct aerodynamic control, while these parameters amplify oscillations in the capsule due to dynamic coupling. Air density variations also follow a similar trend, with the parafoil exhibiting lower sensitivity and the capsule showing heightened sensitivity due to cascading aerodynamic effects.

Studies have shown that the flexible coupling between the parafoil and payload allows for independent rotational motions, leading to complex dynamic interactions. For instance, Slegers and Costello (2003) noted that the parafoil canopy and payload can exhibit unique dynamic behaviours due to their flexible connection, which affects the system's stability and control characteristics. Additionally, research of Hailiang and Zizeng (1994) indicated that the pitch inertia of the payload significantly influences the stability characteristics of the parafoil-payload system, with increased inertia leading to changes in decay ratio and oscillation period. This aligns with the findings in this study that variations in parameters such as $C_{L\alpha}$ and ρ have differing impacts on the parafoil and payload, highlighting the importance of considering both components in the system's dynamic analysis.

Regarding payload mass, Studies have shown that the payload's mass and its relative motion can dominate the system's response, affecting both stability and control. For instance, Ward et al. (2012) explored control mechanisms for parafoil systems by shifting the payload's center of gravity. Their findings indicate that such weight shifts can effectively alter both lateral and longitudinal dynamics, underscoring the payload's pivotal role in manoeuvring the system. Similarly, Slegers and Costello (2003) examined the dynamics of parafoil and payload systems, highlighting that the payload's characteristics, including its mass and attachment geometry, significantly impact the system's behaviour. They noted that the payload's inertia and its coupling with the parafoil can lead to complex dynamic interactions, where the payload's motion can drive the overall system response. These studies collectively suggest that the payload's dynamics actively shape the flight characteristics of parafoil systems. The 9DOF sensitivity analysis demonstrates that the parafoil and capsule respond differently to parameter changes due to their flexible coupling. The aerodynamic coefficients $C_{L\alpha}$ and C_{D0} remain the dominant parameters, with their effects more pronounced in the capsule dynamics. These insights underscore the complexity of the parafoil-payload interaction and the importance of considering both bodies when optimizing for stability and control.

7.1.5. Design Implications

The comparison highlights the importance of designing parafoil systems that accommodate the distinct dynamics of the parafoil and capsule. For the parafoil, optimizing $C_{L\alpha}$ and c is crucial for achieving rapid stabilization and minimizing oscillations. In contrast, the capsule requires careful tuning of payload mass and suspension dynamics to mitigate its heightened sensitivity to inertial and aerodynamic effects.

Flexible coupling introduces significant design challenges, as parameters that stabilize the parafoil can inadvertently destabilize the capsule. This trade-off underscores the need for integrated design approaches that balance the aerodynamic and inertial properties of both components. For example, enhancing the parafoil's aerodynamic control can reduce its sensitivity to payload mass, but additional damping mechanisms may be required to suppress the capsule's oscillations.

Additionally, the findings emphasize the utility of the 9DOF model for capturing nuanced interactions that are absent in the 6DOF system. While the 6DOF results provide a baseline understanding of system dynamics, the 9DOF analysis offers deeper insights into the effects of flexible coupling, enabling more informed design decisions for parafoil-payload systems operating in complex environments like Titan's dense atmosphere.

7.2. Sensitivity Analysis: Combined Effects

7.2.1. Overview of Combined Sensitivity

In addition to individual parameter sensitivity analysis, this section explores the combined effects of multiple parameters varied simultaneously. The motivation for this approach arises from the vast dataset generated, consisting of 3125 unique parameter combinations ($5 \times 5 \times 5 \times 5 \times 5$), where each of the five key parameters is scaled across five levels (0.8, 0.9, 1.0, 1.1, 1.2). analysing this dataset requires methodologies capable of capturing the complex interactions between parameters and their collective impact on system dynamics.

Three complementary approaches were employed to interpret the combined effects:

1. **Pairwise Heatmaps:** Visualizing the interaction between two parameters at a time while keeping others fixed.
2. **Gradient Sensitivity Analysis:** Extracting trends in the system response by analysing gradients derived from the full dataset.
3. **Analysis of Variance (ANOVA):** Quantifying the individual and interactive contributions of parameters to the overall variability in the system response.

These approaches collectively provide insights into dominant parameters, non-linear interactions, and critical parameter combinations. This section introduces each method, explains the underlying theory, and presents the results with physical interpretations.

Pairwise Parameter Interaction Analysis

Combination Effects in Sensitivity Analysis Pairwise heatmaps provide an intuitive visualization of how two parameters interact when varied simultaneously. This method isolates the combined effects of two parameters by fixing the remaining parameters at nominal values, reducing the dimensional complexity of the dataset while highlighting key trends and interactions.

How to Read the Heatmaps: Each heatmap (e.g., Figure 7.5) depicts the peak oscillation amplitude (α) as a function of two parameter scalings:

- The horizontal axis corresponds to the scaling of one parameter (e.g., $m_{payload}$).
- The vertical axis corresponds to the scaling of another parameter (e.g., C_{D0}).
- The colour intensity represents the resulting peak angle of attack, with lighter shades indicating lower peaks and darker shades indicating higher peaks.

Clear gradients along an axis suggest that the parameter on that axis has a dominant influence on the response. Patterns indicating interaction effects between the two parameters appear as curved or non-linear colour transitions. Sweet spots, or regions of optimal performance, may also emerge from these visualizations.

Gradient Sensitivity Analysis

Gradient sensitivity analysis leverages the full dataset to evaluate trends and variations in the system's response (α) to simultaneous parameter changes. This approach computes directional gradients for the combined parameter space, highlighting which parameters or parameter combinations drive the most significant changes in the system response.

How the Gradient Analysis Works: The gradient analysis extracts subsets of the dataset to compute response variations:

- For each parameter, the system response (α) is analysed along its axis of variation while keeping all other parameters fixed.
- The resulting gradient values indicate the rate of change of α with respect to parameter scaling, identifying regions of high sensitivity or stability.
- This method allows for clear identification of dominant parameters across the entire dataset without reducing the dimensional complexity as in the pairwise heatmaps.

How to Interpret Gradient Results: High gradient magnitudes in specific regions suggest areas where parameter variations have an amplified effect on α. Conversely, low gradients indicate stable regions where parameter variations minimally impact the system response. This analysis complements the pairwise heatmaps by offering a quantitative measure of sensitivity trends.

ANOVA for Sensitivity Analysis

Theoretical Context of ANOVA: Analysis of Variance (ANOVA) is a statistical method that partitions the total variability in a dataset into contributions from individual factors (parameters) and their interactions. It provides insights into which parameters or combinations of parameters have statistically significant effects on the response (α). From technical reports of NASA (Deloach, 2010) to books developing different applications for mechanical and aerospace engineering (Libretexts, 2024, Middleton, 2022), various sources were consulted to obtain both foundational knowledge of ANOVA and apply it in this methodology.

How ANOVA Works: ANOVA analyses the variance of α across the parameter combinations:

- **Sum of Squares (SS):** Measures the total variation in the response (α) attributable to a particular parameter or interaction. Larger SS values indicate that the parameter or interaction has a stronger effect on the response.
- **Degrees of Freedom (d.f.):** Represents the number of independent values that can vary for a given parameter or interaction. For a single parameter, the degrees of freedom equal the number of levels minus one. For interactions, d.f. depends on the product of the levels of the interacting parameters.
- **Mean Square (MS):** Calculated as the SS divided by the corresponding d.f., it represents the average contribution of each degree of freedom to the total variation. It is used to compare effects across parameters and interactions.
- **F-value:** The ratio of the MS for a parameter or interaction to the MS of the residual (error). A higher F-value indicates that the parameter has a more significant effect relative to the background noise in the data.
- **Probability (p-value):** The likelihood that the observed effects occurred due to random chance. Smaller p-values (e.g., $p < 0.05$) suggest that the parameter or interaction effect is statistically significant.

How to Interpret ANOVA Results: ANOVA results are typically presented in tabular form, as shown in Table 7.2. Each row corresponds to a parameter or interaction, while the columns summarize the SS, d.f., MS, F-value, and p-value. Here's how to interpret each component in the context of parafoil dynamics:

- **Main Effects:** Dominant parameters (e.g., C_{L_α} or $m_{payload}$) have high SS and F-values, with significant p-values, indicating strong direct influence on α.
- **Interaction Effects:** Interaction terms (e.g., $C_{L_\alpha} \times \rho$) with moderate SS and F-values highlight that the influence of one parameter is conditional on the scaling of another. These are critical for understanding coupled effects in the system.
- **Residuals (Error):** Represent unexplained variability due to factors not included in the analysis. Low residual SS indicates that the key parameters and interactions have captured most of the variability in the response.

For instance, Table 7.2 highlights the relative importance of C_{L_α}, C_{D0}, and $m_{payload}$ in influencing the parafoil dynamics. C_{L_α} appears as the dominant factor with the highest SS and F-value, signifying its critical role in stability. Interaction terms, such as $C_{D0} \times \rho$, emphasize the need to consider coupled aerodynamic effects.

Implications for Parafoil Stability and Control: By combining ANOVA with heatmaps and gradient sensitivity analysis, this comprehensive approach provides a clear hierarchy of parameter importance and interactions. For example:

- Parameters with high F-values and low p-values warrant focused design attention, as they have the most significant impact on stability and control.
- Interactions with moderate significance guide optimization strategies, such as fine-tuning coupled effects between aerodynamic coefficients.

These insights guide design optimization for enhanced stability and control, ensuring that critical parameters and interactions are appropriately addressed.

7.2.2. Results for the 6DOF Model

The combined effects of the parameters on the 6DOF parafoil model were analysed using three complementary methods: pairwise heatmaps, ANOVA, and gradient-based sensitivity analysis. These approaches provide a detailed understanding of how parameter variations interact to influence the system's dynamic behaviour. Given the complexity of the analysis with 5^5 combinations of parameters resulting in 3125 cases, each method highlights different aspects of the system's sensitivity.

Pairwise Parameter Interaction Analysis

The heatmaps in Figure 7.5 reveal several key insights into the combined effects of the parameters on the peak oscillation amplitude (α):

- **Dominance of C_{L_α} and C_{D0}**: The parameters C_{L_α} and C_{D0} dominate the system's response in almost every combination. This dominance is evident from the distinct colour gradients along the axes representing these parameters, regardless of the scaling of the second parameter. For example:
  - In the heatmap for C_{L_α} vs. $m_{payload}$, the colour gradient primarily follows C_{L_α}, indicating that changes in C_{L_α} have a stronger effect on α than $m_{payload}$.
  - In the heatmap for C_{D0} vs. ρ, the gradient follows C_{D0}, showing that C_{D0} has a greater impact than ρ.
- **Interaction Between ρ and $m_{payload}$**: The heatmap for ρ vs. $m_{payload}$ shows a sweet spot where the peak α is highest when ρ is lowest and $m_{payload}$ is highest, and vice versa. This suggests that the interplay between air density and payload mass significantly influences the system's dynamic response.
- **Amplification of Individual Effects:** The trends observed in the individual parameter analysis are amplified when parameters are combined. For instance:
  - The stabilizing effect of higher C_{L_α} is even more pronounced when combined with lower C_{D0}.
  - The destabilizing effect of higher C_{D0} is more evident when paired with lower ρ.
- **Main Effects vs. Interactions:** In many heatmaps, the gradients are primarily aligned along one parameter axis, confirming a dominant main effect. However, in some cases (e.g., ρ vs. $m_{payload}$), the color pattern changes based on the combination of both parameters, indicating a true interaction effect.

Studies have shown that parafoils with higher aspect ratios exhibit increased lift-curve slopes and improved lift-to-drag ratios, indicating better aerodynamic efficiency. However, increased drag due to factors like canopy design can offset these benefits (Yakimenko, 2005b), which supports the differences and combination effects seen from C_{L_α} and C_{D0}. Additionally, as observed and expected from theory, research (Yang et al., 2017) also indicates that parafoil performance is particularly sensitive to changes in air density and payload mass (including in combination), as these parameters directly influence the aerodynamic forces and moments acting on the system. Adjustments in these parameters can significantly impact stability and control.

In summary, the pairwise heatmaps provide a deeper understanding of how parameters interact to influence the parafoil's dynamic response. The dominance of C_{L_α} and C_{D0} highlights the importance of aerodynamic coefficients in determining stability, while interactions between parameters like ρ and $m_{payload}$ reveal nuanced dependencies that can guide design optimization and control strategies.

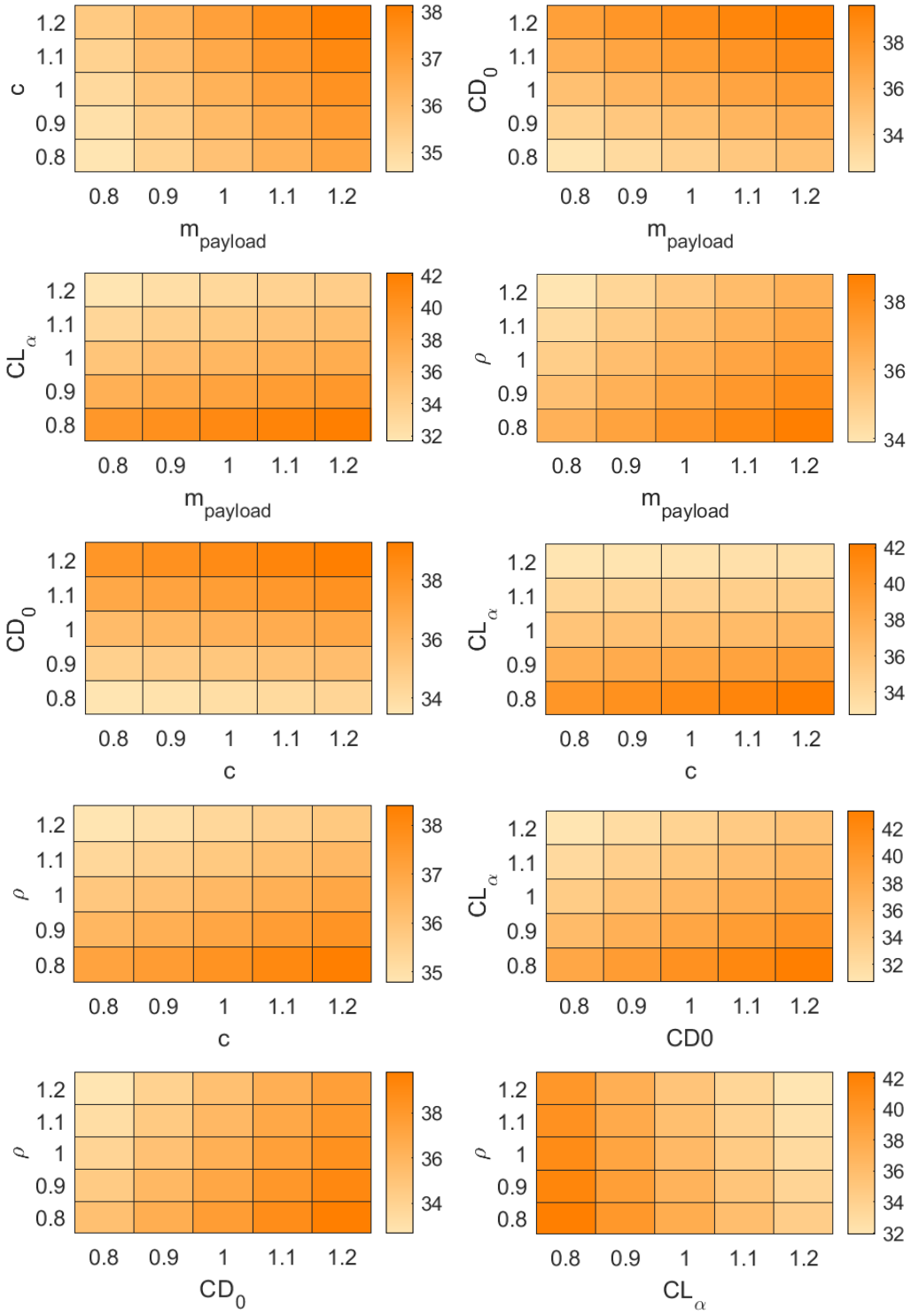

Figure 7.5: Heatmaps showing pairwise sensitivity analysis results for the 6DOF parafoil model. The legend represents the peak α values for each test, the lighter orange indicating lower values of peak α and vice versa.

Table 7.2: ANOVA Table for 6DOF Model

Source	Sum Sq.	d.f.	Mean Sq.	F	Prob > F
m_{payload}	2.35×10^{3}	4	5.87×10^{2}	3.01×10^{6}	0
parafoil_c	5.87×10^{2}	4	1.47×10^{2}	7.52×10^{5}	0
C_{D0}	8.59×10^{3}	4	2.15×10^{3}	1.10×10^{7}	0
$C_{L\alpha}$	2.51×10^{4}	4	6.27×10^{3}	3.21×10^{7}	0
ρ	2.34×10^{3}	4	5.86×10^{2}	3.01×10^{6}	0
$m_{\text{payload}} \times \text{parafoil}_c$	6.60	16	4.13×10^{-1}	2.13×10^{3}	0
$m_{\text{payload}} \times C_{D0}$	6.40	16	4.00×10^{-1}	2.06×10^{3}	0
$m_{\text{payload}} \times C_{L\alpha}$	0.00	16	0.00	4.80×10^{-1}	9.58×10^{-1}
$m_{\text{payload}} \times \rho$	6.00×10^{-1}	16	4.00×10^{-2}	1.85×10^{2}	0
$\text{parafoil}_c \times C_{D0}$	7.10	16	4.44×10^{-1}	2.28×10^{3}	0
$\text{parafoil}_c \times C_{L\alpha}$	1.08×10^{2}	16	6.76	3.47×10^{4}	0
$\text{parafoil}_c \times \rho$	4.50	16	2.81×10^{-1}	1.45×10^{3}	0
$C_{D0} \times C_{L\alpha}$	24.1	16	1.51	7.73×10^{3}	0
$C_{D0} \times \rho$	4.90	16	3.06×10^{-1}	1.58×10^{3}	0
$C_{L\alpha} \times \rho$	0.00	16	0.00	1.27	2.06×10^{-1}
Error	6.00×10^{-1}	2944			
Total	3.91×10^{4}	**3124**			

ANOVA Results

To quantify the relative contributions of individual parameters and their interactions, an Analysis of Variance (ANOVA) was performed. The results are summarized in Table 7.2.

The Sum of Squares (SS) represents the total variability in the response (α) attributable to each parameter or interaction term. Larger SS values indicate parameters with a more pronounced impact on the dynamic response, as they contribute significantly to variations in the peak angle of attack. In this study, C_{L_α}, C_{D0}, and $m_{payload}$ emerge as dominant factors with high SS values. For example, C_{L_α} exhibits the largest SS (2.51×10^4), reflecting its substantial influence on lift generation and stabilization. Similarly, the significant SS of C_{D0} (8.59×10^3) highlights its critical role in drag-induced damping, which mitigates oscillatory behaviour. In contrast, interaction terms such as $m_{payload} \times C_{L_\alpha}$ show negligible SS, indicating limited influence of higher-order effects on system dynamics.

The F-statistic quantifies the relative strength of each parameter's effect compared to residual variability, with higher values indicating greater significance. Parameters like C_{L_α} and C_{D0} exhibit exceptionally high F-statistics (3.21×10^7 and 1.10×10^7, respectively), underscoring their dominance in governing the parafoil's response. These high F-values also suggest that variations in these parameters lead to highly predictable changes in the system's dynamics, which is crucial for design and control optimization. Conversely, interaction terms such as $C_{D0} \times \rho$ show moderate F-values, reflecting a secondary yet noteworthy influence of coupled effects.

The most significant contributors to the maximum oscillation amplitude are C_{L_α}, C_{D0}, and $m_{payload}$. Each parameter plays a distinct physical role in shaping the system's behaviour:

- C_{L_α}**:** With the highest F-statistic and SS, C_{L_α} governs the lift response, directly influencing the system's ability to stabilize after disturbances. Its dominance reflects the parafoil's dependence on precise lift control for maintaining stability.

- C_{D0}**:** As the primary driver of drag-induced damping, C_{D0} mitigates oscillatory motion and enhances stabilization. Its strong contribution emphasizes the importance of optimizing drag coefficients for smooth descent trajectories.

- $m_{payload}$**:** Payload mass contributes significantly to the system's inertia, with higher masses amplifying oscillatory behaviour and delaying stabilization. This highlights the need for careful tuning of payload weight to balance stability and responsiveness.

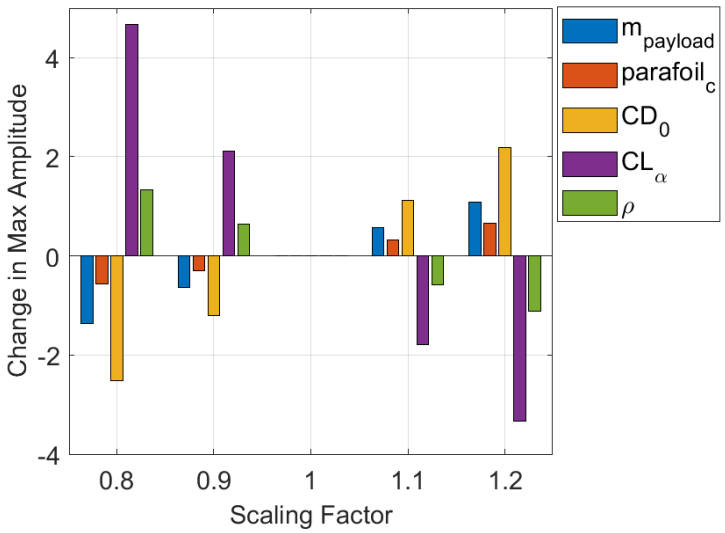

Figure 7.6: Gradient-Based Sensitivity Analysis of the 6DOF Parafoil. The vertical axis indicates changes in peak α relative to the nominal case.

Interaction terms, though generally less influential than main effects, provide insights into coupled dynamics:

- $m_{payload} \times C_{D0}$**:** This interaction suggests that for heavier payloads, higher drag coefficients are essential to suppress destabilizing oscillations effectively. It highlights the interplay between inertial resistance and damping forces.
- $C_{L_\alpha} \times c$**:** The interaction between C_{L_α} and parafoil chord length (c) captures how aerodynamic moments amplify the stabilizing effects of the lift-curve slope. A larger chord enhances C_{L_α}'s impact, whereas a smaller chord diminishes it.

The ANOVA results provide a quantitative validation of the trends observed in the heatmaps. Both approaches consistently highlight the dominance of C_{L_α}, C_{D0}, and $m_{payload}$ in shaping the system's response. For instance, the high SS and F-values for these parameters in the ANOVA align with their pronounced effects in the heatmaps, where distinct color gradients emphasized their significant influence. While the heatmaps offer a visual interpretation of pairwise interactions, ANOVA quantifies these effects, allowing a more rigorous comparison of parameter contributions and interactions.
The absence of significant higher-order effects (e.g., three-way or four-way interactions) indicates that the primary mechanisms governing the parafoil's behaviour such as lift generation, drag-induced damping, and inertial resistance act largely independently. The dominance of main effects suggests that the system's dynamics are driven by well-understood physical principles, simplifying the optimization process.
The ANOVA results provide clear guidance for design and control optimization. Parameters with high F-values and SS, such as C_{L_α} and C_{D0}, should be prioritized in stability and control strategies. Their contributions dominate the system's response, enabling targeted adjustments for improved performance. Additionally, the insights from interaction terms emphasize the importance of considering coupled dynamics, such as the interplay between payload mass and aerodynamic coefficients, to achieve robust and stable designs.

Gradient-Based Sensitivity Analysis

Gradient analysis (Figure 7.6) provides insights into the parameter impacts across all combinations, quantifying how variations influence the peak oscillation amplitude (α). The trends observed are as follows:

- **Positive Gradients:** Most parameters, like as m_{payload}, C_{D0}, and parafoil$_c$, show positive gradients, meaning that scaling them smaller leads to lower peak oscillations, while scaling them larger results in higher peak values of α. This behaviour aligns with their roles in increasing either the system's inertia or aerodynamic forces, which amplify or dampen oscillations.

- **Negative Gradients for C_{L_α} and ρ:** In contrast, C_{L_α} and ρ demonstrate negative gradients. Increasing C_{L_α} reduces peak α, indicating its stabilizing effect via enhanced aerodynamic damping. Similarly, higher ρ strengthens aerodynamic forces, which dampen oscillations and stabilize the system. Reducing these parameters produces larger peaks in α, revealing their critical role in governing the stability and responsiveness of the parafoil system.

- **Minor Asymmetry in C_{L_α}:** A subtle asymmetry is observed in the C_{L_α} gradient, where reductions in C_{L_α} result in reduced damping effects. This likely reflects the inherent sensitivity of this particular parafoil design to lift generation changes. Since C_{L_α} was varied only within a positive range (20% smaller and larger than nominal), this asymmetry does not indicate stall effects but could instead highlights the nonlinear interaction of C_{L_α} with drag and moment terms as Equation 5.25 shows at least a linear relationship between lift and both the C_{L_α} and α.

The gradient sensitivity analysis reinforces the significance of C_{L_α} and C_{D0} as primary tuning parameters for achieving stability. Their roles in aerodynamic damping and drag-induced stabilization are crucial, especially when balancing against inertial effects driven by m_{payload}. Careful adjustment of these parameters is essential to maintain stability while minimizing overshooting thresholds of instability in dynamic conditions.

7.2.3. Results for the 9DOF Model

The 9DOF model introduces a new level of complexity compared to the 6DOF system, as the parafoil and capsule can now respond independently due to the flexible coupling between them. This dynamic independence reveals unique interactions and sensitivities for each component, which are analysed in terms of pairwise parameter interactions, gradient-based sensitivity, and ANOVA.

Pairwise Parameter Interactions

Figures 7.7 and 7.8 present the pairwise parameter sensitivity results for the parafoil (α_p) and the capsule (α_s), respectively. These heatmaps illustrate how combinations of two parameters affect the peak oscillation amplitude. Each plot shows a grid of parameter scaling factors, with color intensity indicating the resulting peak angle of attack.

Parafoil Pairwise Interactions Figure 7.7 highlights the dominant influence of aerodynamic parameters such as C_{L_α}, C_{D0}, and the chord length (c) on the parafoil's dynamics. The following observations can be made:

- **Dominant Aerodynamic Parameters:** C_{L_α} has the most significant effect on the parafoil's peak α_p, with sharp gradients visible in the heatmaps. This parameter directly influences lift generation and stabilization, as observed in both the individual parameter and gradient analyses. C_{D0} and c also show clear effects, highlighting their role in modifying aerodynamic force distributions.

- **Interaction Effects:** Strong interactions exist between aerodynamic parameters, such as $C_{L_\alpha} \times c$ and $C_{D0} \times \rho$, as evidenced by pronounced gradients in their heatmaps. These interactions reflect the combined influence of lift, drag, and geometry on the parafoil's dynamics.

- **Minimal Overall Impact:** While the parafoil heatmaps show stronger contrasts in certain interactions, the overall amplitude changes are relatively smaller compared to the capsule. This suggests that the parafoil, while sensitive to aerodynamic parameters, does not influence the system's peak oscillations as significantly as the capsule does.

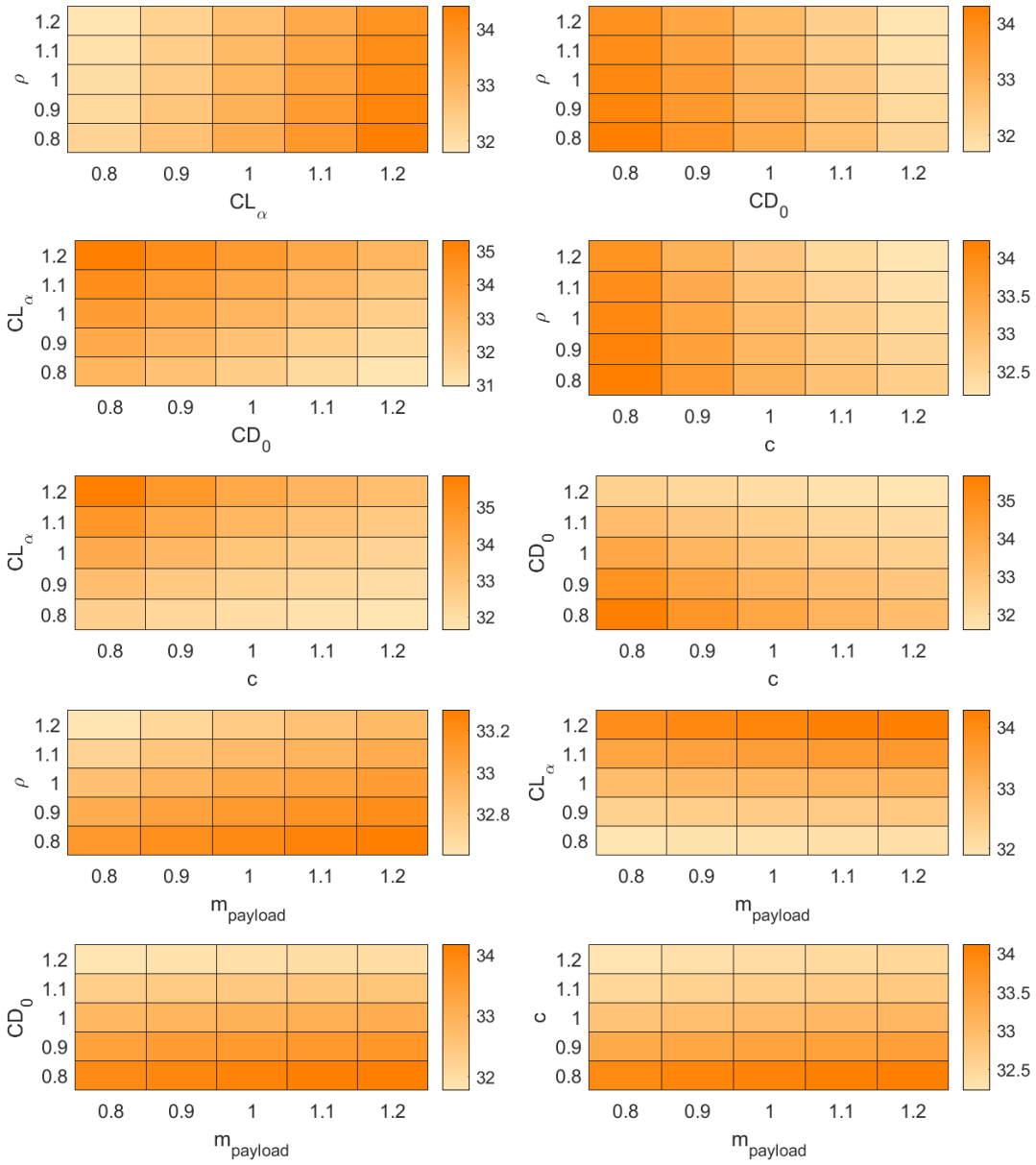

Figure 7.7: Heatmap showing sensitivity analysis results for the 9DOF parafoil model (parafoil dynamics). The legend represents the peak α_p values for each test, the lighter orange indicating lower values of peak α_p and vice versa.

Capsule Pairwise Interactions Figure 7.8 shows the capsule's response, with distinct trends compared to the parafoil:

- **Amplified Inertial Effects:** The capsule's sensitivity to m_{payload} is more pronounced than for the parafoil, as its dynamics are heavily influenced by inertial coupling with the payload. This aligns with findings from the 6DOF model, where payload mass was a critical factor for capsule oscillations.
- **Dominance of Aerodynamic Parameters:** C_{L_α} and C_{D0} remain the most impactful parameters for the capsule, similar to the parafoil. However, their effects are amplified due to the flexible coupling, which propagates parafoil-induced disturbances to the capsule.

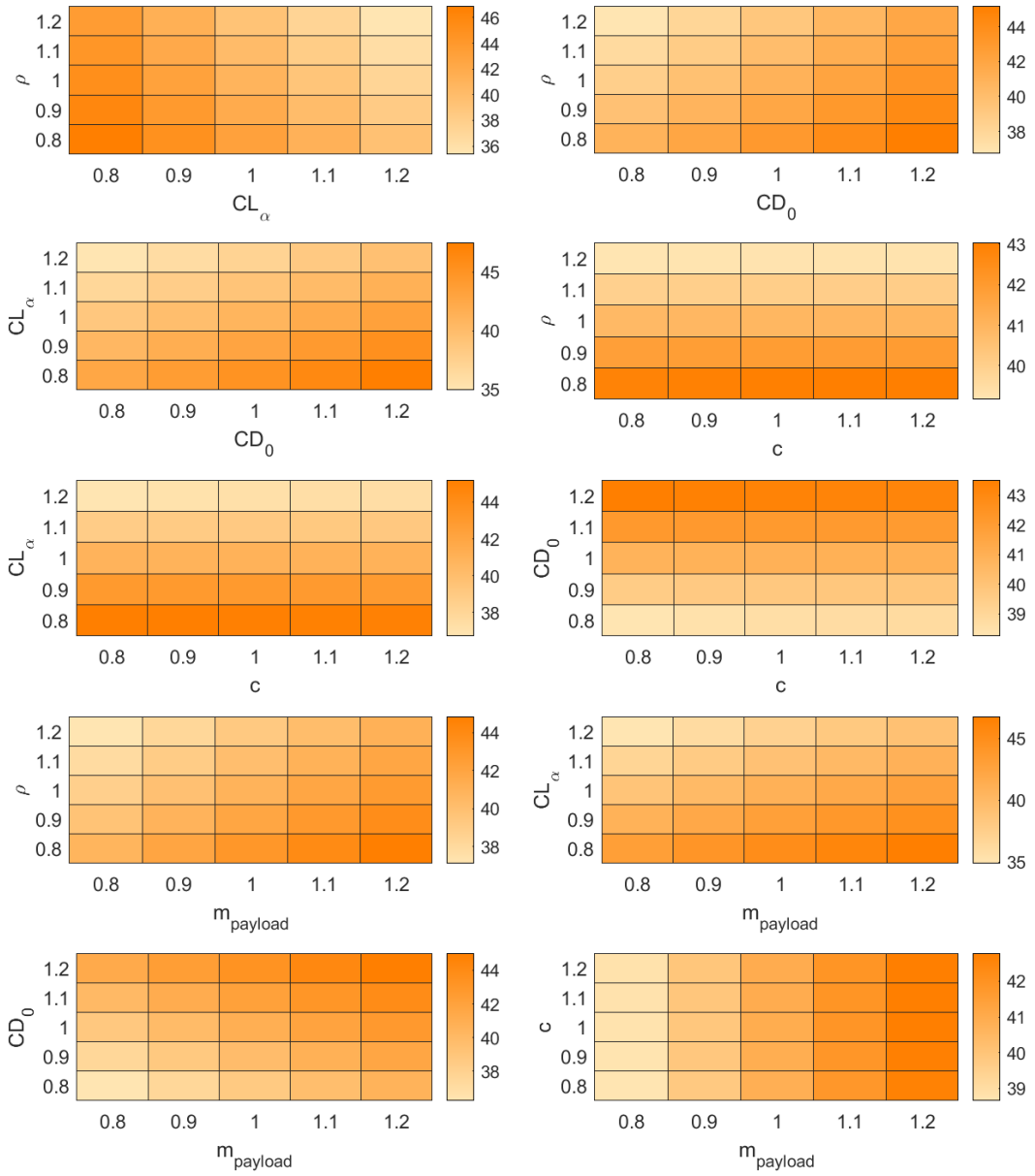

Figure 7.8: Heatmap showing sensitivity analysis results for the 9DOF parafoil model (capsule dynamics). The legend represents the peak α_r values for each test, the lighter orange indicating lower values of peak α_r and vice versa.

- **Consistency with 6DOF System:** The heatmap trends for the capsule largely follow those observed in the 6DOF system, highlighting its dominant role in the coupled 9DOF system. The 6DOF system, modelled as a single rigid body, mirrors the capsule's behaviour in the 9DOF model due to its direct coupling with the parafoil and payload.
- **Dynamic Coupling Effects:** The heatmaps reveal delayed stabilization for the capsule compared to the parafoil, highlighting the role of dynamic coupling. Parameters like m_{payload} interact strongly with C_{L_α} and C_{D0}, leading to complex oscillatory behaviours.

The capsule heatmaps demonstrate trends similar to those observed in the 6DOF system, reinforcing its role as the dominant driver of the coupled system's behaviour. While the parafoil heatmaps

Table 7.3: ANOVA Table for 9DOF Parafoil

Source	Sum Sq.	d.f.	Mean Sq.	F	Prob > F
m_{payload}	2.34×10^{1}	4	5.85×10^{0}	1.02×10^{4}	0
parafoil_c	1.13×10^{3}	4	2.82×10^{2}	4.93×10^{5}	0
C_{D0}	2.09×10^{3}	4	5.21×10^{2}	9.10×10^{5}	0
$C_{L\alpha}$	2.07×10^{3}	4	5.17×10^{2}	9.03×10^{5}	0
ρ	7.69×10^{1}	4	1.92×10^{1}	3.35×10^{4}	0
$m_{\text{payload}} \times \text{parafoil}_c$	1.80×10^{-1}	16	1.13×10^{-2}	1.91×10^{1}	0
$m_{\text{payload}} \times C_{D0}$	2.20×10^{-1}	16	1.38×10^{-2}	2.45×10^{1}	0
$m_{\text{payload}} \times C_{L\alpha}$	1.85×10^{0}	16	1.15×10^{-1}	2.02×10^{2}	0
$m_{\text{payload}} \times \rho$	7.40×10^{-1}	16	4.63×10^{-2}	8.05×10^{1}	0
$\text{parafoil}_c \times C_{D0}$	1.38×10^{2}	16	8.63×10^{0}	1.51×10^{4}	0
$\text{parafoil}_c \times C_{L\alpha}$	1.54×10^{2}	16	9.63×10^{0}	1.68×10^{4}	0
$\text{parafoil}_c \times \rho$	1.70×10^{-1}	16	1.06×10^{-2}	1.85×10^{1}	0
$C_{D0} \times C_{L\alpha}$	7.40×10^{0}	16	4.63×10^{-1}	8.07×10^{2}	0
$C_{D0} \times \rho$	1.10×10^{-1}	16	6.88×10^{-3}	1.15×10^{1}	0
$C_{L\alpha} \times \rho$	5.40×10^{-1}	16	3.38×10^{-2}	5.94×10^{1}	0
Error	1.69×10^{0}	2944	5.74×10^{-4}		
Total	5.69×10^{3}	**3124**			

Table 7.4: ANOVA Table for 9DOF Capsule

Source	Sum Sq.	d.f.	Mean Sq.	F	Prob > F
m_{payload}	6.16×10^{3}	4	1.54×10^{3}	5.76×10^{6}	0
parafoil_c	1.02×10^{1}	4	2.55×10^{0}	9.55×10^{3}	0
C_{D0}	8.91×10^{3}	4	2.23×10^{3}	8.34×10^{6}	0
$C_{L\alpha}$	2.46×10^{4}	4	6.14×10^{3}	2.30×10^{7}	0
ρ	5.40×10^{3}	4	1.35×10^{3}	5.05×10^{6}	0
$m_{\text{payload}} \times \text{parafoil}_c$	0	16	0	4.30×10^{-1}	0.9752
$m_{\text{payload}} \times C_{D0}$	1.74×10^{1}	16	1.09×10^{0}	4.08×10^{3}	0
$m_{\text{payload}} \times C_{L\alpha}$	1.32×10^{1}	16	8.25×10^{-1}	3.10×10^{3}	0
$m_{\text{payload}} \times \rho$	5.00×10^{-1}	16	3.13×10^{-2}	1.24×10^{2}	0
$\text{parafoil}_c \times C_{D0}$	3.50×10^{1}	16	2.19×10^{0}	8.19×10^{3}	0
$\text{parafoil}_c \times C_{L\alpha}$	3.54×10^{1}	16	2.21×10^{0}	8.28×10^{3}	0
$\text{parafoil}_c \times \rho$	0	16	0	1.09×10^{1}	0
$C_{D0} \times C_{L\alpha}$	4.00×10^{0}	16	2.50×10^{-1}	9.44×10^{2}	0
$C_{D0} \times \rho$	3.17×10^{1}	16	1.98×10^{0}	7.43×10^{3}	0
$C_{L\alpha} \times \rho$	2.74×10^{1}	16	1.71×10^{0}	6.41×10^{3}	0
Error	8.00×10^{-1}	2944	2.72×10^{-4}		
Total	4.52×10^{4}	**3124**			

exhibit stronger contrasts in parameter interactions (e.g., $C_{L_\alpha} \times c$), the overall amplitude of changes is smaller, making these effects less impactful on the system's stability compared to the capsule. This highlights the importance of inertial effects and aerodynamic coupling in shaping the overall dynamics, with the capsule's behaviour driving system-level trends in both the 6DOF and 9DOF models.

ANOVA Analysis for the 9DOF Model

Tables 7.3 and 7.4 summarize the ANOVA results for the parafoil and capsule, respectively. These tables provide a statistical breakdown of parameter contributions to the system dynamics.

Parafoil Analysis: Table 7.3 shows the ANOVA results for the 9DOF parafoil. Several key trends emerge:

- **Main Effects:**
  - C_{L_α}, C_{D0}, and c exhibit nearly identical contributions, as evidenced by their similar Sum of Squares values (2.07×10^3, 2.09×10^3, and 1.13×10^3, respectively). This aligns with the heatmaps, where these parameters showed comparable impacts on the parafoil's peak angle of attack (α_p).
  - ρ) has a relatively lower Sum of Squares (7.69×10^1), suggesting its influence on the parafoil's dynamics is present but less significant compared to aerodynamic parameters.
- **Interactions:**
  - Prominent interactions include $C_{L_\alpha} \times c$ (Sum of Squares 1.54×10^2) and $C_{D0} \times C_{L_\alpha}$ (Sum of Squares 7.40×10^0), which confirm that geometric and aerodynamic parameters collectively shape the parafoil's stability.
  - The interaction $m_{\text{payload}} \times C_{L_\alpha}$ is significant, showing a Sum of Squares of 1.85×10^0, highlighting that the payload modulates aerodynamic sensitivity, though to a lesser degree than in the capsule.
- **System Dynamics Insights:** The smaller magnitudes of C_{L_α} and C_{D0} contributions compared to the capsule suggest that while the parafoil exhibits notable sensitivity, its oscillations are less amplified. The ANOVA findings mirror the observations from the heatmaps, where the parafoil's dynamics were influenced by strong contrasts but lower overall amplitude changes than the capsule.

Capsule Analysis: Table 7.4 presents the ANOVA results for the 9DOF capsule, showcasing distinct dynamics:

- **Main Effects:**
  - C_{L_α} dominates with a Sum of Squares of 2.46×10^4, far exceeding the contributions of other parameters. This aligns with the capsule's dependency on lift stabilization, as highlighted in the heatmaps and gradient sensitivity results.
  - **Parasite Drag Coefficient** (C_{D0}) and m_{payload} follow, with Sum of Squares of 8.91×10^3 and 6.16×10^3, respectively. These parameters significantly affect the capsule's dynamics, consistent with the 6DOF system.
- **Interactions:**
  - Prominent interactions include $m_{\textbf{payload}} \times C_{D0}$ (Sum of Squares 1.74×10^1) and $m_{\textbf{payload}} \times C_{L_\alpha}$ (Sum of Squares 1.32×10^1), indicating strong inertial-aerodynamic coupling.
  - Higher-order interactions, such as $C_{L_\alpha} \times \rho$, also exhibit notable contributions (Sum of Squares 2.74×10^1), underscoring the combined effects of environmental and aerodynamic forces.
- **Magnitude Differences:** Compared to the 6DOF system, the capsule exhibits significantly higher Sum of Squares values for all primary parameters and interactions. This reflects the amplified oscillations and greater parameter sensitivity in the 9DOF system due to the dynamic coupling.

The ANOVA results from the 9DOF parafoil and capsule reveal key differences and similarities when compared to the 6DOF model:

- **Parameter Sensitivity:**

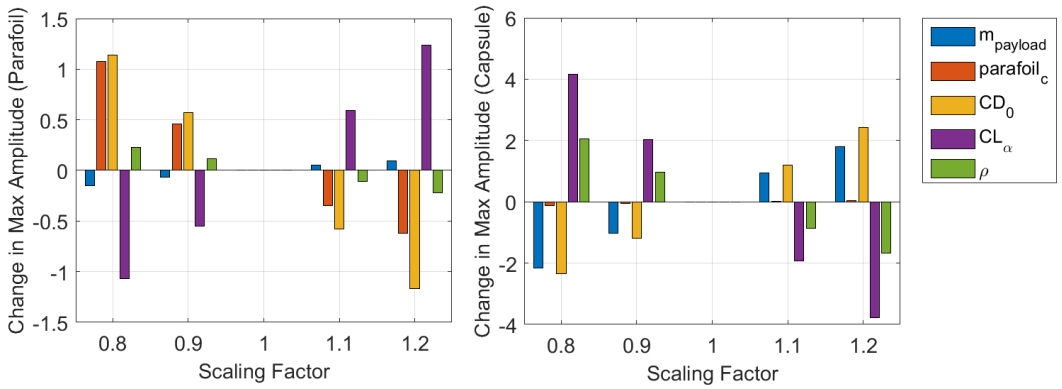

Figure 7.9: Gradient-based sensitivity analysis of the 9DOF model, showing maximum oscillation amplitude for parameter scaling factors.

  - In the 6DOF model, C_{L_α} and C_{D0} were also dominant, particularly for the single rigid body. This trend continues in the capsule of the 9DOF model, where these parameters govern lift and drag stabilization.
  - However, in the parafoil, C_{L_α}, C_{D0}, and c exhibit equal contributions, reflecting the parafoil's unique dynamics due to flexible coupling.

- **Interaction Effects:**
  - The capsule's interactions are more pronounced in the 9DOF model than in the 6DOF system. This suggests that the flexibility and coupling introduce additional complexity, amplifying the effects of combined parameters.
  - The parafoil exhibits fewer significant interactions, highlighting its comparatively linear response within the tested range.

- **Amplitude of Oscillations:**
  - The capsule's higher Sum of Squares values confirm it experiences larger oscillations than the parafoil, consistent with the 6DOF system's behaviour, where the rigid body response aligns more closely with the capsule dynamics of the 9DOF model.

Implications for Design and Stability: These ANOVA findings emphasize the need for careful tuning of aerodynamic coefficients (C_{L_α}, C_{D0}) and payload mass to achieve stability. While the parafoil exhibits strong geometric influences, the capsule's sensitivity to lift and drag necessitates precise control to mitigate oscillations. The 9DOF results highlight the significance of dynamic coupling in amplifying certain effects, which must be accounted for in design optimization strategies.

Gradient-Based Sensitivity Analysis

The gradient-based sensitivity results, shown in Figure 7.9, quantify the impact of each parameter's scaling on the peak oscillation amplitude. The parafoil and capsule exhibit contrasting sensitivity profiles:

Parafoil Sensitivity For the parafoil, the gradient bars in Figure 7.9 (left) represent the change in maximum α_p relative to the nominal configuration as each parameter is scaled. The key observations are:

- **Dominant Parameters:** The lift-curve slope (C_{L_α}), parasite drag coefficient (C_{D0}), and chord length (c) exhibit the strongest gradients, indicating their critical influence on the parafoil's

maximum oscillation amplitude. Increasing C_{L_α} or c generally reduces peak α_p, while increasing C_{D0} increases it. These trends align with heatmap results, confirming their impact on stabilizing aerodynamic effects.

- **Smaller Gradient Magnitudes:** Compared to the capsule, the parafoil exhibits smaller gradient magnitudes, suggesting reduced sensitivity to parameter changes. This reflects the parafoil's ability to self-stabilize through direct aerodynamic control.

- **Limited Inertial Influence:** Payload mass (m_{payload}) and air density (ρ) have minor effects on the parafoil's dynamics, as indicated by their low gradient magnitudes. This is consistent with the parafoil's greater reliance on aerodynamic parameters for stability.

Capsule Sensitivity For the capsule, the gradient bars in Figure 7.9 (right) show the change in maximum α_s for each parameter's scaling. The observations include:

- **Dominant Parameters:** Similar to the 6DOF system, the lift-curve slope (C_{L_α}), parasite drag coefficient (C_{D0}), and payload mass (m_{payload}) have the largest gradients. Increasing C_{L_α} or m_{payload} amplifies α_s, while increasing C_{D0} reduces it.

- **Amplified Sensitivity:** The capsule exhibits larger gradient magnitudes than the parafoil, highlighting its heightened sensitivity to parameter variations. This amplification results from dynamic coupling, where disturbances from the parafoil propagate to the capsule.

- **Minimal Effect of Parafoil Geometry:** The parafoil chord length (c) has a negligible impact on the capsule's dynamics, as its influence on lift generation is primarily restricted to the parafoil.

The gradient-based sensitivity analysis reveals that the capsule in the 9DOF system behaves similarly to the 6DOF system, with dominant contributions from C_{L_α}, C_{D0}, and m_{payload}. However, the capsule exhibits amplified sensitivities due to dynamic coupling with the parafoil. In contrast, the parafoil shows reduced sensitivity and smaller gradient magnitudes, emphasizing its role as a stabilizing component in the system.
The analysis underscores the importance of balancing parafoil and capsule dynamics. While aerodynamic parameters like C_{L_α} and C_{D0} directly influence stability, their effects differ between the parafoil and capsule. A holistic design approach is required to optimize system performance, considering both aerodynamic and inertial contributions. For instance:

- Increasing C_{L_α} can stabilize the parafoil but may amplify capsule oscillations due to coupling effects.

- Adjusting C_{D0} provides damping for the capsule but could reduce parafoil efficiency.

- Careful tuning of m_{payload} is essential to avoid destabilizing oscillations while maintaining overall system stability.

This integrated perspective highlights the necessity of accounting for dynamic interactions in design and control strategies to ensure robust performance under varying conditions.

7.2.4. Comparison and Analysis of Sensitivity Results

The sensitivity analysis conducted for both the 6DOF and 9DOF models highlights critical insights into the dynamics of parafoil-payload systems. These insights reveal how aerodynamic, geometric, and inertial parameters influence stability and oscillatory behaviour, providing a deeper understanding of the system's physical behaviour and guiding future design considerations.

Table 7.5: Dominant parameters for the 6DOF system, 9DOF parafoil, and 9DOF capsule based on combined sensitivity analysis.

Parameter	6DOF System	9DOF Parafoil	9DOF Capsule
Aerodynamic ($C_{L\alpha}$, C_{D0})	**Dominant**	**Dominant**	**Dominant**
Geometry (c)	Secondary	**Dominant**	Minimal
Inertia ($m_{payload}$)	Moderate	Minimal	**Dominant**
Atmospheric (ρ)	Moderate	Minimal	Moderate

Key Findings from the 6DOF and 9DOF Models

The dominant parameters identified for the 6DOF system, 9DOF parafoil, and 9DOF capsule are summarized in Table 7.5. These results provide a clear hierarchy of parameter influence across the different models.

- **Aerodynamic Parameters (C_{L_α}, C_{D0}):** Aerodynamic coefficients dominate the dynamics of all configurations. The sensitivity of C_{L_α} and C_{D0} varies between the parafoil and capsule due to dynamic coupling in the 9DOF system:
  - For the parafoil, increasing C_{L_α} amplifies oscillations, while increasing C_{D0} reduces them.
  - For the capsule, these trends are inverted. Increasing C_{L_α} stabilizes oscillations, while increasing C_{D0} amplifies them. This highlights the parafoil's role as the primary aerodynamic control surface and its indirect influence on the capsule.
- **Geometric Parameter (c):** The parafoil chord length plays a significant role in the parafoil's dynamics, reflecting its direct aerodynamic control. For the capsule, the effect of c is minimal, as its motion is primarily governed by coupling with the parafoil.
- **Inertia (m_{payload}):** Payload mass has moderate influence in the 6DOF model but becomes the dominant driver of capsule oscillations in the 9DOF system. Its negligible influence on the parafoil reflects the decoupled nature of the parafoil's aerodynamic response.
- **Atmospheric Density (ρ):** While moderate across all configurations, ρ has a more noticeable effect on the parafoil in the 9DOF model due to its immediate interaction with aerodynamic forces.

Comparison Between Parafoil and Capsule Dynamics

The 9DOF model reveals distinct differences in sensitivity between the parafoil and capsule:

- **Parafoil Sensitivity:** The parafoil's maximum amplitude is driven by C_{L_α}, c, and C_{D0}, with moderate sensitivity to ρ. Its ability to stabilize quickly through direct aerodynamic interaction moderates the magnitude of oscillations.
- **Capsule Sensitivity:** The capsule exhibits higher sensitivity to C_{L_α}, C_{D0}, and m_{payload}. The flexible coupling amplifies these effects, leading to larger oscillations compared to the parafoil.
- **Trend Inversion:** The inversion of C_{L_α} and C_{D0} effects between the parafoil and capsule highlights the complex interplay between aerodynamic forces and dynamic coupling. While aerodynamic changes stabilize one component, they can destabilize the other, necessitating a balanced design approach.

Comparison with the 6DOF Model

- **Unified vs. Decoupled behaviour:** The 6DOF system behaves as a rigid unit, with consistent trends for all parameters. In contrast, the 9DOF model separates parafoil and capsule responses, revealing more complex interactions.

- **Magnitude of Effects:** The ANOVA results show higher magnitudes of Sum of Squares and F-values for the 9DOF system, indicating greater sensitivity and amplified oscillations. This reflects the added complexity of flexible coupling and independent motion.
- **Dynamic Coupling Effects:** The 9DOF model captures nuanced interactions between the parafoil and capsule, revealing nonlinear and asymmetric effects absent in the rigid 6DOF system.

Design Implications

The combined findings from the sensitivity analyses provide clear guidelines for the design and optimization of parafoil-payload systems:

- **Aerodynamic Parameter Tuning:** Optimizing C_{L_α} and C_{D0} is critical for balancing lift and damping. Increasing C_{L_α} enhances aerodynamic responsiveness but must be carefully managed to avoid destabilizing the capsule.
- **Geometric and Inertial Considerations:** Adjusting parafoil chord length (c) can improve parafoil stability without compromising capsule dynamics. Reducing payload mass or incorporating damping features can mitigate capsule oscillations.
- **Holistic Design Approach:** The inversion of trends between parafoil and capsule underscores the need for integrated design strategies. Active control systems and real-time parameter adjustments could help balance stability and efficiency across varying conditions.

Conclusion

The sensitivity analysis of the 6DOF and 9DOF models underscores the importance of aerodynamic, geometric, and inertial parameters in shaping system dynamics. The 9DOF model, with its detailed representation of parafoil and capsule interactions, offers deeper insights into parameter sensitivities and dynamic coupling, making it a valuable tool for high-fidelity design and control optimization. These findings align with literature emphasizing the need to consider multi-body interactions for precision landing and stability (Schutte et al., 2020, Yang et al., 2017, Zhu et al., 2021).

7.3. Wind Analysis

The wind analysis was conducted to study the parafoil system's behaviour under different wind scenarios. As described in the Environment chapter, the wind model includes steady-state winds and 6-turbulence gust winds which was placed at various altitude points as seen in Figure 3.3. The maximum steady-state wind was set to 10 m/s, and the maximum gust wind speed to 5 m/s, decreasing with altitude during descent. These values are based on Titan wind profiles from the literature, where maximum wind speeds near the equator at 40 km altitude were estimated at 15 m/s.
The simulations were performed for both 6DOF and 9DOF parafoil systems across various wind scenarios, including:

- **Longitudinal Wind (0°):** Wind applied in the X-Z plane.
- **Lateral Wind (90°):** Wind applied in the Y-Z plane.
- **Combined Longitudinal and Lateral Wind (45°):** Wind applied between the X-Z and Y-Z planes.

The nominal case, with no wind applied, was included as a baseline trajectory. The steady-state wind and gust contributions were combined into a wind vector, transformed into the body frame, and added to the body velocity to simulate the effects.

7.3.1. Longitudinal-Only Wind Conditions

Under purely longitudinal winds (green lines in Figure 7.10), the primary effect is a reduction in forward velocity. This headwind increases aerodynamic drag, which in turn shortens the longitudinal range compared to the nominal (no-wind) case. The resulting trajectories show this reduction clearly, with the green lines falling short of the nominal ground track.

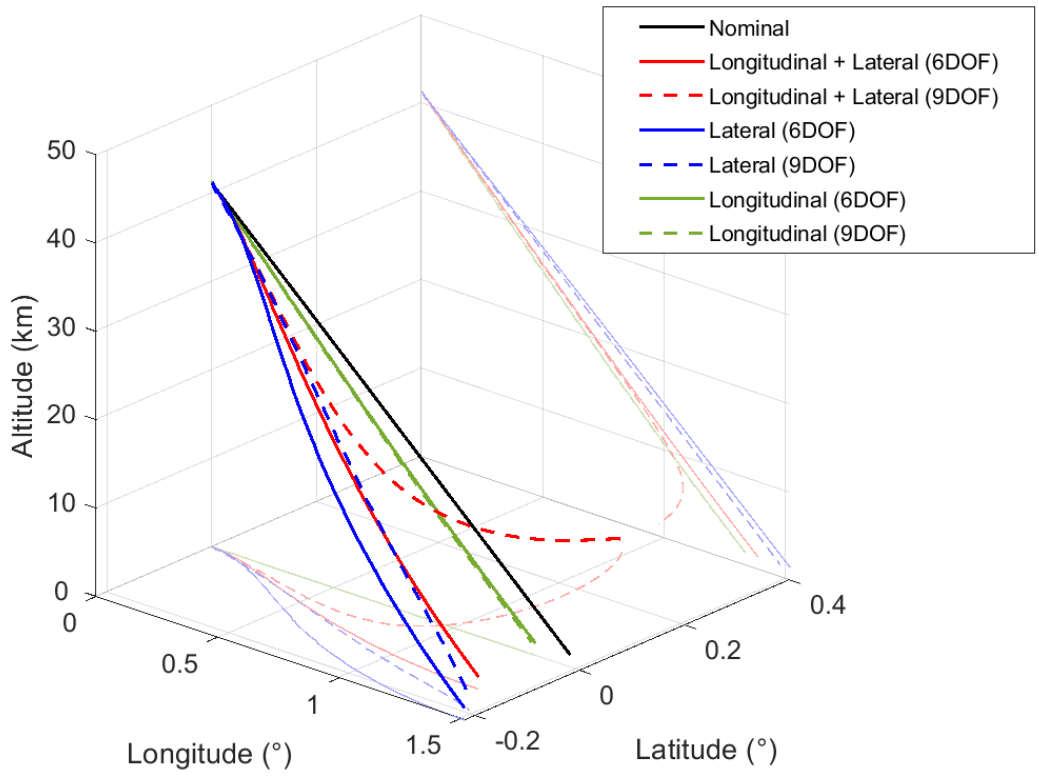

Figure 7.10: 3D trajectories of the parafoil system for each wind scenario.

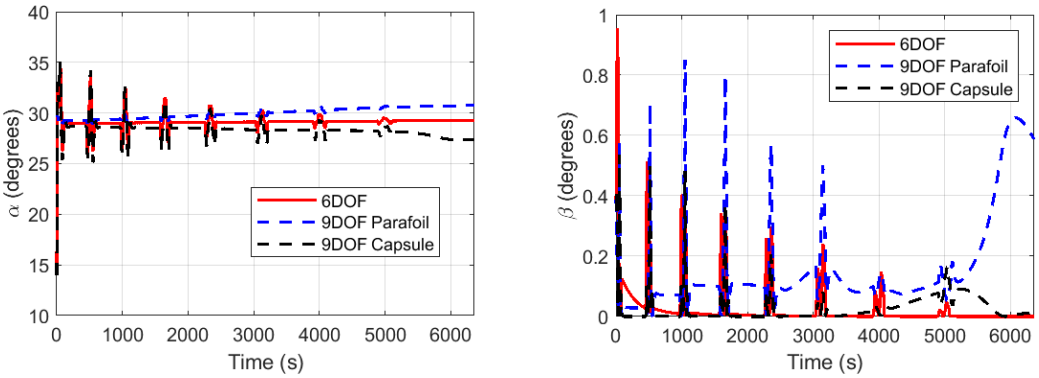

(a) Alpha plane for longitudinal + lateral winds.

(b) Beta plane for longitudinal + lateral winds.

Figure 7.11: Behaviour of the parafoil system under 45 deg (longitudinal and lateral) winds with both steady-state and gust components.

The α versus time plots (Figure 7.13) reveal that both 6DOF and 9DOF models adjust their pitch angles to reach a new equilibrium under headwind conditions. Since the wind disturbance is purely in the longitudinal direction, the sideslip angle β remains near zero throughout the descent. This behaviour is consistent with findings in the literature, where longitudinal wind disturbances primarily affect the x-z plane and lead to predictable reductions in range.

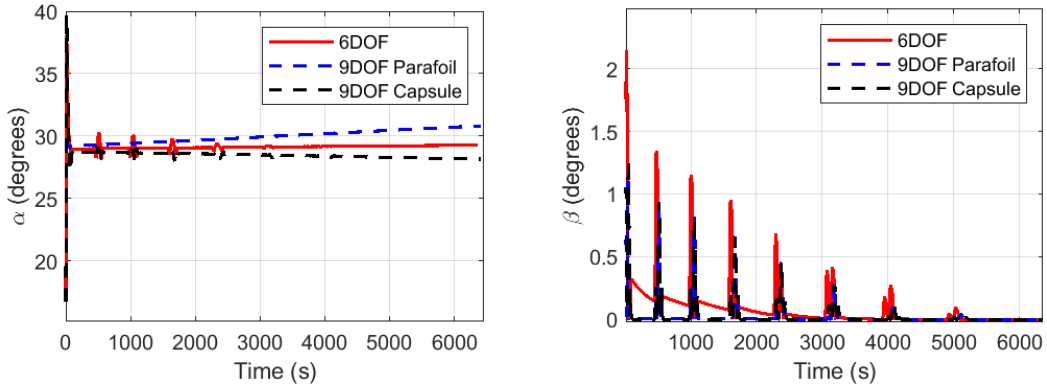

(a) Alpha plane for lateral winds.

(b) Beta plane for lateral winds.

Figure 7.12: Behaviour of the parafoil system under 90 deg lateral winds with both steady-state and gust components.

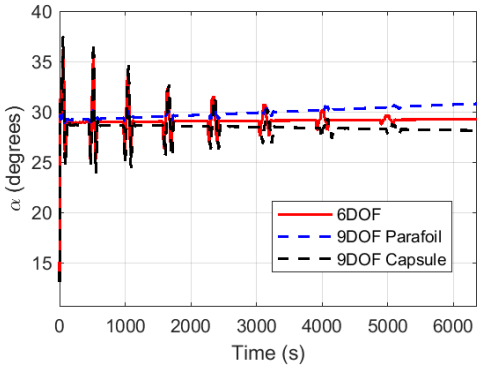

Figure 7.13: Behaviour of the parafoil system under 0 deg longitudinal winds with both steady-state and gust components, shown in the alpha plane (beta oscillations are static at 0 deg throughout).

7.3.2. Lateral-Only Wind Conditions

In the presence of lateral winds (blue lines in Figure 7.10), the system experiences noticeable lateral displacement, resulting in a final latitude offset. Unlike the longitudinal case, the forward longitudinal motion remains relatively unaffected, meaning the final longitude remains close to the nominal trajectory.

The time history plots of β (Figure 7.12b) show an initial increase in sideslip angle as the system accommodates the lateral wind. Both the 6DOF and 9DOF models exhibit damping of these β oscillations over time, eventually reaching a stable descent with a constant lateral offset. The angle of attack α (Figure 7.12a) remains largely unchanged compared to the nominal case. Studies on sideslip effects have shown that even small lateral deviations can lead to measurable lateral drift, emphasizing the need to control β to maintain accurate trajectory tracking (Feng et al., 2023).

7.3.3. Combined Longitudinal and Lateral Winds

The combined wind scenario (red lines in Figure 7.10) produces the most complex behaviour, as the system simultaneously experiences headwinds in the longitudinal direction and crosswinds in the lateral direction. For the 6DOF model (solid red line), the trajectory reflects a straightforward combination of the individual effects observed in the longitudinal-only and lateral-only cases. The result is a shorter longitudinal range (similar to the green line) and a lateral offset (similar to the blue line).

In contrast, the 9DOF model (dashed red line) exhibits a more pronounced and divergent response. The flexible coupling in the 9DOF system allows internal degrees of freedom to redistribute aerodynamic forces and moments. This redistribution can cause the parafoil to yaw or sideslip into configurations that amplify drag and lateral displacement. Studies have shown that specifically in models with higher degrees of freedom, the extra degrees of flexibility under complex wind conditions have amplified trajectory deviations due to interactivity between lateral and longitudinal dynamics (Tao et al., 2017). The β versus time plots (Figure 7.11b) indicate that the sideslip angle grows larger and persists toward the end of the trajectory, resulting in a significant shift in both longitude and latitude. Also, interesting to note is that the capsule's sideslup angle starts to grow first, already around 4000 s and this seems to lead the parafoil's sideslip angle to also grow very quickly which is what leads to the large aerodynamic forces in the lateral direction, resulting in the large deviation in latitude.
Furthermore, the α versus time results (Figure 7.11a) show subtle differences in equilibrium angles of attack for the 9DOF model under combined wind conditions. Over a long descent, these small deviations integrate into significant trajectory shifts, reinforcing the conclusion that flexible systems exhibit non-linear responses to multi-directional wind inputs.

7.3.4. Summary of Wind Effects

The combined results of the 3D trajectories and time-history plots lead to the following conclusions:

- **Longitudinal-Only Winds**: These winds reduce forward range (green lines). Both 6DOF and 9DOF models adjust their pitch (α) to reach equilibrium, with minimal lateral motion or sideslip (β).
- **Lateral-Only Winds**: These winds displace the system laterally (blue lines), resulting in a latitude offset. The sideslip angle β increases initially but stabilizes over time, with limited impact on longitudinal range.
- **Combined Winds**: The interplay of longitudinal and lateral winds introduces complexity. The 6DOF model behaves predictably as a combination of the two simpler cases, but the 9DOF model shows a markedly different response. The flexibility of the 9DOF system results in persistent β angles, increased lateral displacement, and reduced longitudinal range compared to both the nominal case and simpler wind scenarios (Feng et al., 2023, Tao et al., 2017).

These findings underscore the importance of incorporating additional degrees of freedom and flexible coupling in parafoil models. Higher-fidelity modelling captures non-linear responses and provides a more accurate depiction of real-world flight dynamics under complex wind conditions.
To supplement the wind analysis presented in this chapter, additional test results are provided in Appendix D. These tests include steady-state and gust wind effects applied individually to longitudinal and lateral wind scenarios. While not representing extreme or combined-case scenarios, these results serve as a reference for understanding the isolated effects of specific wind conditions on the parafoil system's dynamics.

7.4. Transition to Design Implications

The sensitivity and wind analyses presented in this chapter provide critical insights into the dynamic behaviour and stability of the parafoil-payload system under Titan-like conditions. The results not only address the key research questions regarding parameter influence and environmental adaptability but also highlight the complex interplay between aerodynamic forces and dynamic coupling. These findings inform the design and tuning of parafoil systems, offering actionable recommendations for optimizing stability and performance in planetary descent missions. The subsequent conclusion synthesizes these insights, linking the detailed analyses back to the broader objectives of the study and exploring their implications for future design and operational strategies.

8

Conclusions and Recommendations

This thesis has presented the development, verification, and sensitivity analysis of high-fidelity 6DOF and 9DOF simulation models for parafoil and capsule dynamics during descent on Titan. By addressing the identified research gaps, the study provides a comprehensive understanding of parafoil stability, dynamic coupling effects, and environmental influences, particularly wind disturbances. The findings not only reveal critical sensitivities but also emphasize the unique impact of lateral wind effects, an aspect often overlooked in traditional parafoil studies. This research stands out due to the thorough validation of the 9DOF model through a step-by-step verification process, starting with the 6DOF model and progressively increasing complexity. The wind analyses, in particular, offer valuable insights into both longitudinal and lateral dynamics, underscoring the need for robust designs capable of handling Titan's challenging atmospheric conditions.

8.1. Addressing the Research Questions and Objectives

This study set out to investigate the stability and dynamic behaviour of parafoil systems during descent on Titan, addressing critical aspects of rotational stability, dynamic coupling effects, and environmental influences. By developing and validating high-fidelity 6DOF and 9DOF models, conducting comprehensive sensitivity analyses, and exploring wind-induced disturbances, the research provides a detailed understanding of the factors influencing parafoil descent performance. The following subsections revisit the research questions posed in the introduction and summarize how the findings of this study successfully address these objectives. Each research question is examined through the lens of the simulation results, highlighting the key insights gained and their implications for future planetary exploration missions.

Stability in Dynamics: What are the key factors influencing the rotational stability of parafoil systems during descent on Titan?

The sensitivity analysis revealed several key parameters that significantly influence the rotational stability, particularly the angle-of-attack (α) oscillations:

- **Critical Parameters:** The C_{L_α}, C_{D0}, and m_{payload} emerged as the most influential factors. These parameters affect the peak oscillation amplitudes and overall dynamic behaviour of the system.
- **6DOF and 9DOF Comparison:** In the 6DOF model, these parameters uniformly influenced the rigid system's response. However, the 9DOF model revealed that flexible coupling redistributes

these sensitivities, with the parafoil and capsule responding differently to the same parameter changes.

- **Wind Influence:** The wind results showed that these parameters also interact with wind disturbances. For example, changes in C_{L_α} and C_{D0} can amplify or dampen the effects of crosswinds, influencing both longitudinal and lateral stability. The 9DOF model demonstrated that these aerodynamic sensitivities are magnified when the system is subjected to realistic wind profiles.

In addition to identifying the key parameters influencing rotational stability, this study employed rigorous verification methods to validate the modelling fidelity. Energy conservation tests ensured that the models adhered to fundamental physical principles, particularly during dynamic transitions such as oscillations and descent. The stiffness tests, which examined the sensitivity of the models to small perturbations, confirmed the stability of the numerical integration schemes and validated the robustness of the 9DOF model under varying stiffness parameters. These verification steps not only reinforced confidence in the model's accuracy but also provided a solid foundation for the sensitivity analyses and wind studies. The systematic approach to validation highlights the importance of model fidelity in accurately capturing the complex dynamics of coupled parafoil-capsule systems, particularly in the presence of aerodynamic and inertial interactions. These insights provide a clear understanding of how aerodynamic and inertial properties govern parafoil stability, forming a foundation for optimizing design parameters to achieve stability under varying environmental conditions.

Dynamic Coupling Effects: How do flexibility and coupling between the parafoil and capsule impact the overall dynamics of the system?

The introduction of flexibility in the 9DOF model highlighted the complex interactions between the parafoil and capsule:

- **Redistribution of Sensitivity:** The 9DOF model showed that flexible coupling redistributes the sensitivity of key parameters. The parafoil exhibits dampened oscillations due to direct aerodynamic control, while the capsule experiences amplified oscillations because of its indirect coupling.
- **Opposite Effects:** Certain parameters, such as C_{L_α} and C_{D0}, produced opposite effects on the parafoil and capsule rotations. This inverse relationship becomes even more pronounced when subjected to wind disturbances, where the parafoil stabilizes rapidly while the capsule lags, resulting in divergent behaviour.
- **Wind-Induced Dynamics:** The wind analyses revealed that dynamic coupling also influences the system's response to lateral winds. Flexible coupling can amplify the effects of crosswinds on the capsule, making it more prone to sideslip oscillations. This finding underscores the importance of considering both components independently to develop effective suspension and control strategies.

Environmental Influence: How do Titan's wind profiles and atmospheric variability affect the precision and stability of parafoil landings?

The wind analyses in chapter 7 provide some of the most unique and significant contributions of this study:

- **Impact of Wind Disturbances:** Both steady-state and turbulent wind profiles introduced substantial longitudinal and lateral disturbances. The 9DOF model, with its flexible coupling, exhibited greater sensitivity to these disturbances compared to the 6DOF model. This highlights the importance of modelling flexibility to understand the true dynamic behaviour under realistic wind conditions.

- **Lateral Stability Concerns:** β oscillations emerged as a critical factor under crosswind conditions. Even small deviations in β led to significant trajectory deviations, demonstrating that lateral stability is just as important as longitudinal stability. This aspect is rarely addressed in traditional parafoil studies, making this finding particularly valuable.

- **Model Validation:** The verification steps ensured that the wind profiles and dynamic responses were accurately modelled. The results emphasize the need for **robust aerodynamic design** and potential control strategies to mitigate wind-induced disturbances, ensuring precise and stable landings.

These insights confirm that achieving reliable parafoil performance on Titan requires careful consideration of both longitudinal and lateral stability under dynamic wind conditions.

Aerodynamic Parameters: How do variations in key aerodynamic parameters influence the stability characteristics of the parafoil during descent?

The sensitivity analyses provided a detailed understanding of how aerodynamic parameters influence system stability:

- **Dominant Aerodynamic Parameters:** The lift-curve slopeC_{L_α} and C_{D0} were the most influential aerodynamic parameters. Variations in these parameters significantly affected the peak oscillation amplitudes of both the parafoil and capsule.

- **Inverse Relationships:** The 9DOF model revealed that changes in C_{L_α} and C_{D0} produced opposite effects on the parafoil and capsule rotations. This interaction becomes even more complex under wind disturbances, where these aerodynamic parameters can either amplify or dampen the system's response to gusts and crosswinds.

- **Gradient Sensitivity Analysis:** The gradient plots confirmed that small changes in aerodynamic parameters could lead to substantial changes in system dynamics. These insights are critical for optimizing aerodynamic design to achieve robust and predictable behaviour in varying wind conditions.

This study has successfully addressed the main research question:

To what extent can high-fidelity dynamic modelling enhance the understanding of parafoil stability and performance for planetary landings?

The development and validation of the 6DOF and 9DOF models, combined with comprehensive sensitivity analyses and wind studies, provide a detailed understanding of parafoil stability and dynamic behaviour. The step-by-step verification process, including unique stiffness and energy tests, ensures confidence in the models' reliability. The inclusion of both longitudinal and lateral wind effects sets this study apart, offering a more complete analysis of parafoil dynamics. These findings bridge the gap between simplified rigid-body models and more complex flexible models, laying a foundation for designing robust parafoil systems capable of achieving precision landings on Titan and other extraterrestrial environments.

8.2. Recommendations

The findings of this thesis highlight several areas for further exploration and refinement in parafoil modelling and simulation for planetary descent missions. While this study established a robust baseline for open-loop stability analysis under Titan-like conditions, the following recommendations aim to address the limitations encountered and pave the way for future advancements.

Refining Parafoil and Parachute Models

To enhance the realism and predictive accuracy of the models, it is crucial to revisit certain assumptions and incorporate additional physical effects. For instance, the aerodynamic modelling of parafoils could be significantly improved by including material properties such as porosity and elasticity. These properties influence the deformation of the canopy under aerodynamic loads, which, in turn, affects stability and control. Additionally, the suspension lines can be modelled with flexibility to capture their dynamic response, as rigid-line assumptions oversimplify the system and may overlook critical coupling effects. To further enhance the realism of the parafoil model, adopting a multiple rigid-line representation of the parafoil canopy, as outlined in Slegers and Costello (2003), can provide a balance between simplicity and increased insight into aerodynamic performance. This approach discretizes the canopy into multiple panels, allowing for detailed modelling of local aerodynamic effects, such as panel-specific lift and drag forces, and their interactions. Compared to computationally expensive computational fluid dynamics (CFD) simulations, this method offers an efficient way to capture critical dynamics like asymmetric loading, wake effects, and local deformations, while remaining compatible with existing MATLAB/Simulink frameworks. Incorporating this multi-panel model would be a practical next step for investigating more nuanced dynamics, such as lateral-directional stability under crosswinds or control authority in clustered parafoil systems.

Particularly, the inclusion of a nonlinear mass-spring model for cloth dynamics, as developed in Anton et al. (2023), could provide a more accurate representation of the canopy's structural response. By replacing traditional linear spring models with nonlinear springs, this approach better captures the dynamic deformation behavior of the parafoil or parachute under aerodynamic forces. Coupling such structural dynamics with computational fluid dynamics (CFD) tools, as also suggested in the same work, can offer a robust framework for analyzing both steady-state and transient behaviors, particularly in cases involving wake interactions or unsteady aerodynamics. Incorporating these advanced modeling techniques would enable a deeper exploration of critical phenomena such as lateral-directional stability, transient inflation dynamics, and the effect of material properties on overall system performance.

Validation and Numerical Enhancements

The verification and validation process in this thesis revealed several areas where numerical techniques could be improved. Numerical artifacts, such as the transient "wobble" observed during early descent phases, underscored the sensitivity of the models to integrator settings. A more systematic exploration of integrator types, stiffness parameters, and damping mechanisms would strengthen the reliability of the simulations. Additionally, testing alternative numerical schemes could provide insights into the trade-offs between computational efficiency and accuracy, particularly for high-fidelity models like the 9DOF parafoil.

Cross-validation against simplified models could further enhance confidence in the results. For instance, comparing the behaviour of the 9DOF model with rigid-body approximations or single-mass systems would help isolate the impact of added complexities. Such comparative analyses can clarify the roles of flexibility and coupling, identifying cases where simpler models suffice and where high-fidelity models are indispensable.

Addressing Model Assumptions and Expanding Capabilities

Several assumptions made in this study, while necessary for simplification, limit the broader applicability of the findings. For example, the assumption of symmetric canopy loading does not account for potential asymmetries arising from manufacturing tolerances, deployment irregularities, or wind shear. Future studies should investigate the effects of such asymmetries on parafoil stability, particularly in lateral dynamics, which are critical under Titan's predominantly zonal wind patterns.

Higher-order effects, such as interactions between parafoil loading and payload dynamics, also merit further exploration. The coupling between the parafoil and the payload in this study revealed significant redistribution of sensitivities, with the parafoil and capsule responding differently to aerodynamic parameter variations. Extending this analysis to include non-linear coupling effects would provide a more comprehensive understanding of the system's dynamics and stability limits.

Advanced Environmental and Wind Modelling

Given the challenging and dynamic atmospheric conditions on Titan, integrating more advanced environmental models into future simulations is essential. Wind disturbances play a pivotal role in shaping descent dynamics, and incorporating time-varying wind fields, gusts, and shear layers would enhance the predictive robustness of the parafoil and capsule models. In particular, this study has not yet explored the impact of vertical winds, which are expected to significantly influence stability and descent trajectories, especially during turbulent phases. Testing vertical wind effects in conjunction with lateral and longitudinal wind profiles would provide a more comprehensive understanding of aerodynamic interactions in Titan's unique atmosphere.

A key recommendation is the integration of General Circulation Models (GCMs) to represent Titan's atmospheric dynamics with greater fidelity. GCMs simulate 3D wind fields, including variations in speed, direction, and pressure across different altitudes, latitudes, and seasons. Leveraging GCMs would enable simulations to account for Titan's complex seasonal and geographic atmospheric variability, such as the strong zonal winds near the equator and seasonal changes in polar wind patterns. Such models would provide insights into optimal mission windows and landing strategies, informing both descent planning and parafoil design.

Additionally, coupling GCM-derived data with the existing Titan-specific models (for some altitudes, available in Garg and Mooij (2016)) would allow for real-time trajectory adjustments based on varying wind conditions, enhancing the system's resilience and precision. For example, landing sites could be selected based on predicted wind conditions during descent, mitigating potential oscillations or deviations caused by turbulent or vertical winds.

Incorporating GCM data would not only refine parafoil descent simulations but also support the development of adaptive control strategies for precision landings. By simulating vertical and lateral wind variations across diverse atmospheric scenarios, future studies can improve parafoil robustness and optimize its performance under Titan's extreme conditions. These advancements would bridge the gap between idealized testing environments and real-world mission requirements, ensuring that the system performs reliably across a broader range of environmental influences.

Guidance, Navigation, and Control (GNC) Enhancements

While this study focused on open-loop stability, the findings establish a strong foundation for future research to incorporate closed-loop Guidance, Navigation, and Control (GNC) systems. These systems would enable parafoils to dynamically adapt to wind disturbances and trajectory deviations, ensuring precision landings under Titan's challenging atmospheric conditions. A promising avenue for advancing GNC capabilities involves leveraging convex optimization techniques for real-time guidance and control.

Convex optimization algorithms present a robust and computationally efficient framework for addressing the challenges of real-time guidance in planetary descent missions. As demonstrated by Mazouz et al. (2021), these algorithms are particularly well-suited for systems operating under complex constraints, such as wind variability and trajectory convergence requirements. Future work could integrate convex optimization into the parafoil system to dynamically adjust its descent trajectory in response to atmospheric disturbances. This approach would enable the parafoil to maintain an optimal glide path while minimizing deviations caused by turbulent or varying wind profiles. Although this algorithm was developed for lower-fidelity models, its extension to the high-fidelity 9DOF system presented in this study could provide a significant step forward in achieving robust and adaptive GNC performance.

Building on convex optimization, future GNC systems could incorporate trajectory optimization techniques such as waypoint-based or path-based planning. For parafoil systems, predictive path planning could leverage real-time environmental data to adjust glide paths and altitude control dynamically. This would ensure precise lateral and longitudinal positioning, particularly important in Titan's atmosphere, where wind disturbances can significantly impact stability and descent accuracy. The adaptability of convex optimization to nonholonomic systems like parafoils makes it a compelling candidate for enabling efficient and accurate trajectory control.

By leveraging convex optimization techniques and real-time trajectory planning, future iterations of

this study can enhance the parafoil system's adaptability and resilience, paving the way for robust and reliable planetary descent strategies.

BIBLIOGRAPHY

Anton, S. V., Rapisarda, C., Ross, O. J., & Mooij, E. (2023). Development and validation of a nonlinear fabric model for subsonic parachute aerodynamics. *Journal of Spacecraft and Rockets, 60*(6), 1871–1891. https://doi.org/10.2514/1.A35583

APL, J. H. (2017). Why titan? https://dragonfly.jhuapl.edu/Why-Titan/

Barnes, J. W. e. a. (2021). Science goals and objectives for the dragonfly titan rotorcraft relocatable lander. *The planetary science journal, 2*. https://doi.org/10.3847/PSJ/abfdcf

Coustenis, A., & Raulin, F. (2023). *Titan*. Springer Berlin Heidelberg. https://doi.org/10.1007/978-3-662-65093-6_1594

Deloach, R. (2010). Analysis of variance in the modern design of experiments. *NASA*. https://doi.org/10.2514/6.2010-1111

Dragonfly mission overview [Published by NASA. Accessed: 2024-06-12]. (2022). https://doi.org/https://nssdc.gsfc.nasa.gov/nmc/spacecraft/display.action?id=DRAGONFLY

Feng, L., Xing, X., Gong, Q., Li, Y., & Guo, Y. (2023). *Trajectory control of pfc recovery under adrc and improved los guidance law* (L. Yan, H. Duan, & Y. Deng, Eds.). Springer Nature Singapore.

Garg, K., & Mooij, E. (2016). Autonomous navigation of a balloon over saturn's moon titan. https://doi.org/10.2514/6.2016-0887

Gorman, C. M., & Slegers, N. J. (2011). Comparison and analysis of multi-body parafoil models with varying degrees of freedom. *21st AIAA Aerodynamic Decelerator Systems Technology Conference and Seminar*. https://doi.org/10.2514/6.2011-2615

Gorman, C. M., & Slegers, N. J. (2012). Evaluation of multibody parafoil dynamics using distributed miniature wireless sensors. *Journal of Aircraft, 49*(2), March–April. https://doi.org/10.2514/1.C031566

Hailiang, M., & Zizeng, Q. (1994). 9-dof simulation of controllable parafoil system for gliding and stability. *Journal of National University of Defense Technology, 16*(2), 49.

Hibbeler, R. C. (2013). *Engineering mechanics. dynamics*. Pearson.

Hörst, S. M. (2017). Titan's atmosphere and climate. *Journal of Geophysical Research: Planets, 122*(3), 432–482. https://doi.org/10.1002/2016je005240

Ibrahim, S. K., & Engdahl, R. A. (1974). *Parachute dynamics and stability analysis. [using nonlinear differential equations of motion]*. NASA. https://api.semanticscholar.org/CorpusID:117115318

Jann, T. (2006). Development and flight testing of an autonomous parafoil-load system demonstrator. *ICAS*.

Lebonnois, S., Burgalat, J., Rannou, P., & Charnay, B. (2012). Titan global climate model: A new 3-dimensional version of the ipsl titan gcm. *Icarus, 218*(1), 707–722. https://doi.org/10.1016/j.icarus.2011.11.032

Lebreton, J.-P., Coustenis, A., Lunine, J., Raulin, F., Owen, T., & Strobel, D. (2009). Results from the huygens probe on titan. *Astron. Astrophys. Rev., 17*, 149–179. https://doi.org/10.1007/s00159-009-0021-5

Leeman, A., Preda, V., Huertas, I., & Bennani, S. (2022). Autonomous parafoil precision landing using convex real-time optimized guidance and control. *CEAS Space Journal, 15*(2), 371–384. https://doi.org/10.1007/s12567-021-00406-z

Leishman, J. G. (2023). Aerodynamics of airfoil sections. *Introduction to Aerospace Flight Vehicles*. https://eaglepubs.erau.edu/introductiontoaerospaceflightvehicles/chapter/airfoil-characteristics/

Libretexts. (2024, February). Chapter 9: Analysis of variance (anova). https://eng.libretexts.org/Courses/California_State_Polytechnic_University_Humboldt/Statistical_Analysis_of_Data_for_Engineers/Chapter_09%3A_Analysis_of_Variance_%28ANOVA%29

LISSAMAN, P., & BROWN, G. (1993). Apparent mass effects on parafoil dynamics. *Aerospace Design Conference*. https://doi.org/10.2514/6.1993-1236

Lorenz, R. D. (2017). Wind shear and turbulence on titan: Huygens analysis. *Icarus*, *295*, 119–124. https://doi.org/10.1016/j.icarus.2017.06.010

Lorenz, R. D., MacKenzie, S. M., Neish, C. D., Gall, A. L., Turtle, E. P., Barnes, J. W., Trainer, M. G., Werynski, A., Hedgepeth, J., & Karkoschka, E. (2021). Selection and characteristics of the dragonfly landing site near selk crater, titan. *The Planetary Science Journal*, *2*(1), 24. https://doi.org/10.3847/PSJ/abd08f

Lorenz, R., Turtle, E., Barnes, J., Trainer, M., Adams, D., Hibbard, K., Sheldon, C., Zacny, K., Peplowski, P., Lawrence, D., Ravine, M., McGee, T., Sotzen, K., MacKenzie, S., Langelaan, J., Schmitz, S., Wolfarth, L., & Bedini, P. (2018). Dragonfly: A rotorcraft lander concept for scientific exploration at titan. *Johns Hopkins APL Technical Digest (Applied Physics Laboratory)*, *34*, 374–387.

Mazouz, R., Quadrelli, M., & Mooij, E. (2021). Convex optimization guidance for precision landing on titan. https://doi.org/10.2514/6.2021-1345

Middleton, J. A. (2022). *Experimental statistics and data analysis for mechanical and aerospace engineers*. CRC Press, Taylor; Francis Group.

Mooij, E. (1992, October). *Esa huygens probe: Entry and descent analysis* (tech. rep. No. E.W.P. 1679). European Space Research and Technology Centre (ESTEC). Noordwijk, The Netherlands.

Mooij, E. (1994). *The motion of a vehicle in a planetary atmosphere*. Delft University of Technology, Delft.

Mooij, E., Wijnands, Q., & Schat, B. (2003). 9 dof parafoil/payload simulator development and validation. *AIAA Modeling and Simulation Technologies Conference and Exhibit*. https://doi.org/10.2514/6.2003-5459

Mooij, E., Wijnands, Q., & Schat, B. (2012). 9 dof parafoil/payload simulator development and validation. *AIAA Modeling and Simulation Technologies Conference and Exhibit*. https://doi.org/10.2514/6.2003-5459

Prakash, O., & Ananthkrishnan, N. (2006). Modeling and simulation of 9-dof parafoil-payload system flight dynamics. *AIAA Atmospheric Flight Mechanics Conference and Exhibit*. https://doi.org/10.2514/6.2006-6130

Quadrelli, M. B., Schutte, A., Rimani, J., & Ernolli, L. (2019). Aero maneuvering dynamics and control for precision landing on titan. *2019 IEEE Aerospace Conference*, 1–16. https://doi.org/10.1109/AERO.2019.8742230

Schutte, A., Delaune, J., Skylanskiy, E., Hewitt, R., Daftry, S., Quadrelli, M. B., & Matthies, L. (2020). Integrated simulation and state estimation for precision landing on titan. *2020 IEEE Aerospace Conference*, 2–13. https://doi.org/10.1109/aero47225.2020.9172491

Slegers, N. (2003). On the use of rigging angle and canopy tilt for control of a parafoil and payload system. *AIAA*. https://doi.org/10.2514/6.2003-5609

Slegers, N., & Costello, M. (2003). Aspects of control for a parafoil and payload system. *Journal of Guidance, Control, and Dynamics*, *26*(6), 898–905. https://doi.org/10.2514/2.6933

Soderblom, J. M., Brown, R. H., Soderblom, L. A., Barnes, J. W., Jaumann, R., Mouélic, S. L., Sotin, C., Stephan, K., Baines, K. H., & Buratti, B. J. (2010). Geology of the selk crater region on titan from cassini vims observations. *Icarus*, *208*(2), 905–912. https://doi.org/10.1016/j.icarus.2010.03.001

Tao, J., Sun, Q., Sun, H., Chen, Z., Dehmer, M., & Sun, M. (2017). Dynamic modeling and trajectory tracking control of parafoil system in wind environments. *IEEE/ASME Transactions on Mechatronics*, *22*(6), 2736–2745. https://doi.org/10.1109/TMECH.2017.2766882

Titan exploration [Published by NASA. Accessed: 2024-06-12]. (2023). https://doi.org/https://science.nasa.gov/saturn/moons/titan/exploration/

Ward, M., Culpepper, S., & Costello, M. (2012). Parafoil control using payload weight shift. *Journal of Aircraft*, *51*. https://doi.org/10.2514/6.2012-4738

Wright, M. J. (2019). The dragonfly entry and descent system.

Yakimenko, O. (2005a). On the development of a scalable 8-dof model for a generic parafoil-payload delivery system. *AIAA*, 14. https://doi.org/10.2514/6.2005-1665

Yakimenko, O. (2005b). On the development of a scalable 8-dof model for a generic parafoil-payload delivery system. *AIAA*, 14. https://doi.org/10.2514/6.2005-1665

Yang, H., Song, L., Wang, W., & Huang, J. (2014). 4-dof longitudinal dynamic simulation of powered-parafoil. *Beijing University of Aeronautics and Astronautics*, *40*, 1615–1622. https://doi.org/10.13700/j.bh.1001-5965.2014.0086

Yang, H., Lei, S., & Chen, W. (2017). Research on parafoil stability using a rapid estimate model. *Chinese Journal of Aeronautics*, *30*. https://doi.org/10.1016/j.cja.2017.06.003

Yelle, R. V., Strobell, D. F., Lellouch, E., & Gautier, D. (1998). Engineering models for titan ' s atmosphere. *Engineering, Environmental Science, Physics*. https://api.semanticscholar.org/CorpusID:29791106

Zhu, H., Sun, Q., Liu, X., Liu, J., Sun, H., Wu, W., Tan, P., & Chen, Z. (2021). Fluid–structure interaction-based aerodynamic modeling for flight dynamics simulation of parafoil system. *Nonlinear Dynamics*, *104*, 1–22. https://doi.org/10.1007/s11071-021-06486-0

A

Parachute Aerodynamic Coefficients

To ensure accurate verification of the 6DOF parachute-capsule model, aerodynamic coefficients were sourced from validated datasets in Mooij, 1992 and implemented into the system's equations of motion. These coefficients, which include the lift (C_L), drag (C_D), moment (C_m), normal force (C_N), and side force (C_S) coefficients, form the backbone of the aerodynamic forces and moments acting on the system. Figures A.1, A.2, A.3, A.4, and A.5 present the relationships of these coefficients with respect to the angle of attack (α) and Mach number.

- **Figure A.1:** Displays the drag coefficient variation for the parafoil and capsule across Mach numbers. This highlights how drag forces change under different flow regimes, critical for assessing stability during descent.
- **Figure A.2:** Shows the lift coefficient (C_L) for both components, emphasizing the linear dependency on the angle of attack.
- **Figure A.3:** Illustrates the pitching moment coefficient (C_m) and its variations with Mach number, providing insights into pitch stability.
- **Figure A.4:** Depicts the normal force coefficient (C_N) with respect to β, emphasizing lateral force variations and their significance for yaw and roll dynamics.
- **Figure A.5:** Demonstrates the side force coefficient (C_S) dependence on angle of attack (α) and Mach number, which is relevant for assessing sideslip effects.

These plots serve to verify that the aerodynamic model accurately represents the behaviour of the parachute-capsule system under varying flight conditions. While these properties were primarily used for the 6DOF verification phase, their insights remain critical for understanding the baseline aerodynamic performance of the parachute system.

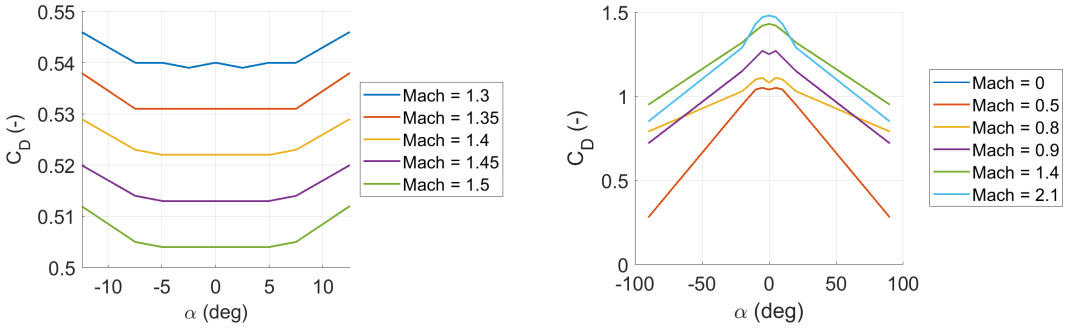

Figure A.1: Drag Coefficient Comparison for Parafoil and Capsule

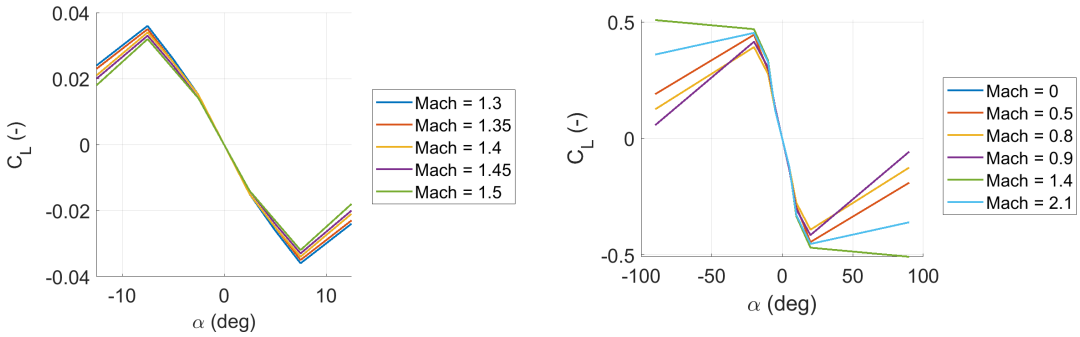

Figure A.2: Lift Coefficient Comparison for Parafoil and Capsule

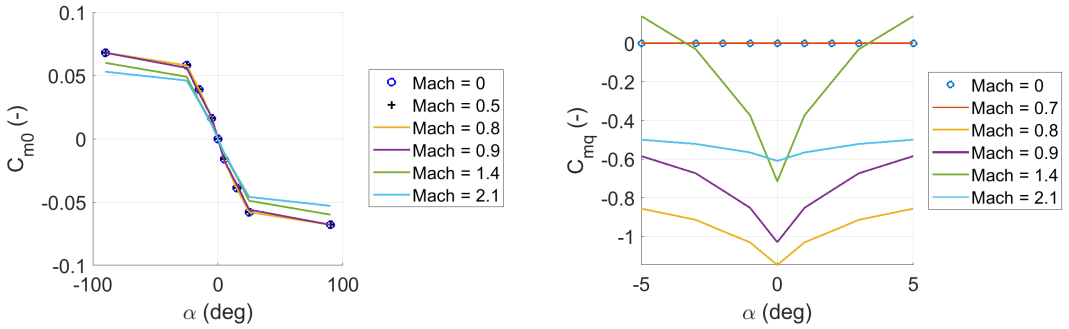

Figure A.3: Moment Coefficient Capsule

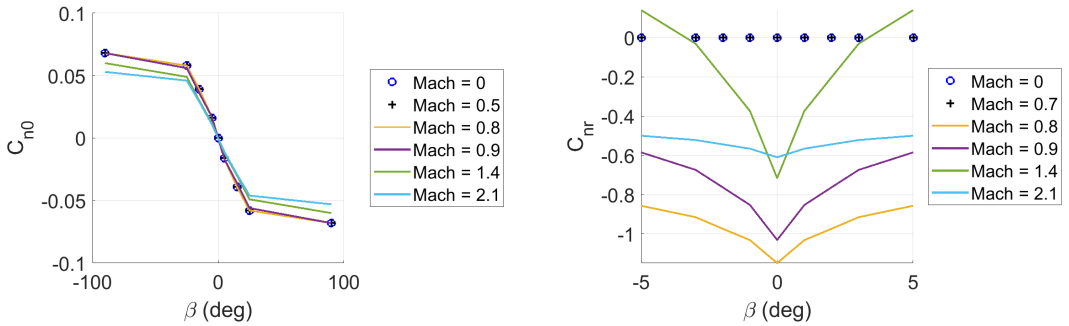

Figure A.4: Normal Force Coefficient Capsule

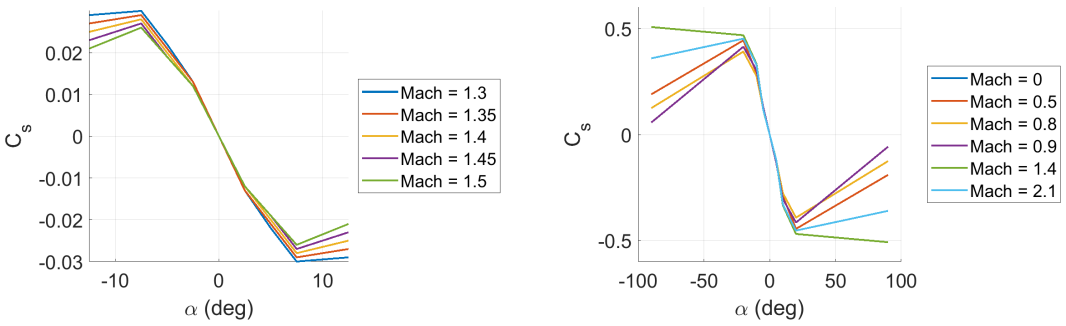

Figure A.5: Side Force Coefficient Comparison for Parafoil and Capsule

B

Detailed Integrator Trade-Off Analysis

To validate the selection of `ode15s` as the primary integrator for the 9DOF parafoil model, a detailed comparison of α_s (capsule angle of attack) over time was conducted. Figures B.1 and B.2 illustrate the results for each tested integrator, with a focus on the first 30 seconds of the descent. The second plot excludes `ode1`, which showed extreme deviations, and `ode45`, which failed to complete the simulation within a reasonable timeframe.

1. **Smoothness:**
   - `ode15s` provided the smoothest curve for α_s, making it ideal for capturing sensitive dynamics without introducing numerical artifacts.
   - Fixed-step integrators (`ode1` to `ode5`) exhibited jagged behaviour, with `ode1` performing particularly poorly, generating large numerical errors.
2. **Stability:**
   - Variable-step integrators (`ode15s`, `ode113`, and `ode23`) handled stiff equations effectively and were able to simulate the descent without significant issues.
   - `ode1` and `ode45` failed to maintain stability, with the former showing extreme oscillations and the latter being computationally infeasible beyond a few seconds of simulation time.
3. **Computation Time:**
   - `ode15s` offered a balanced trade-off, maintaining reasonable computational efficiency while ensuring accuracy.
   - Fixed-step integrators, such as `ode1`, were faster but sacrificed accuracy significantly.
   - `ode45`, although typically reliable, required an excessive runtime for this stiff system, rendering it impractical for the analysis.

Figures B.1 and B.2 provide a clear visual representation of these observations, confirming the suitability of `ode15s` for the 9DOF parafoil model.

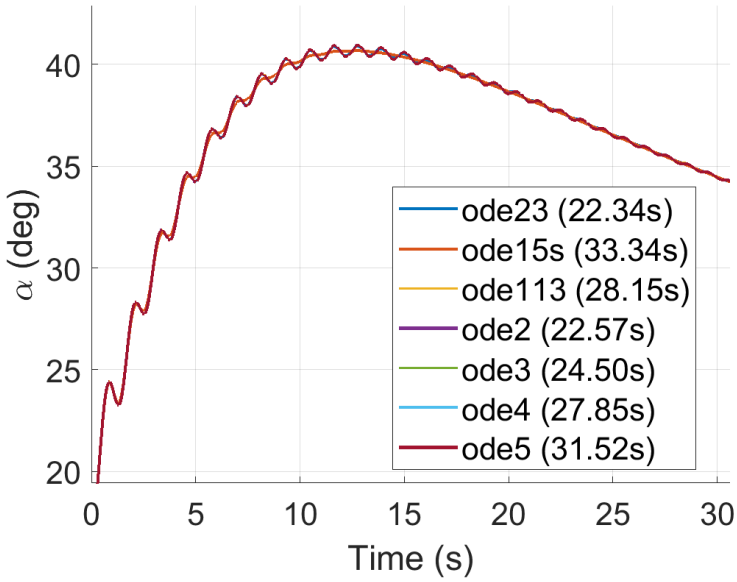

Figure B.1: Comparison of integrators: α (angle of attack) vs. time for the 9DOF model, including all integrators. Note the extreme behaviour of `ode1` and incomplete results for `ode45`.

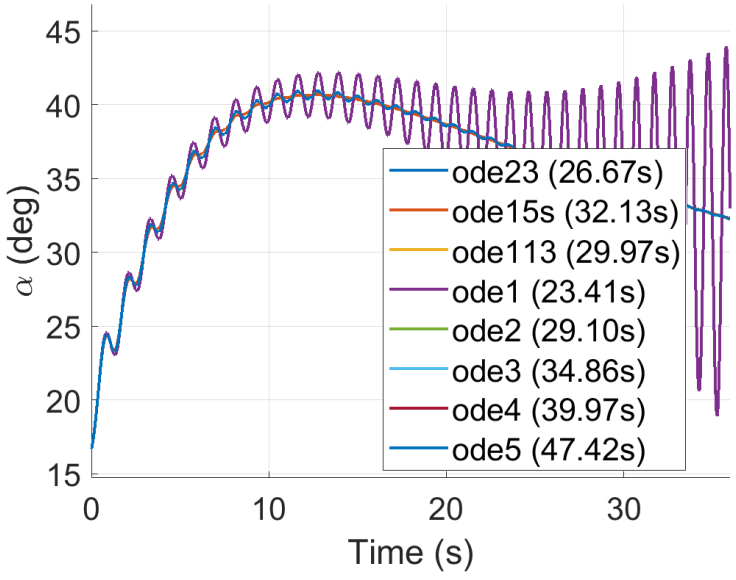

Figure B.2: Comparison of integrators: α (angle of attack) vs. time for the 9DOF model, excluding `ode1` and `ode45` for clarity.

C

Stability Metrics

This appendix provides a detailed breakdown of the comparative analysis of stability metrics considered during the early stages of this research. The table below outlines the natural frequency (ω_n), damping ratio (ζ), and overshoot values for various test cases. While natural frequency and damping ratio are widely recognized metrics for evaluating system stability, their application to parafoil dynamics in this study faced significant challenges. Specifically, the extracted values of ω_n and ζ often exhibited inconsistencies or outright failures in extraction, as indicated by the "NA" entries in the table.

The prevalence of "NA" highlights limitations in accurately characterizing certain test cases using these metrics, particularly for near-aperiodic or highly transient oscillatory responses observed in the parafoil system. These failures undermine the reliability of ω_n and ζ as primary metrics for this specific system. Conversely, overshoot—a localized and physically meaningful measure of the maximum deviation from equilibrium—proved to be consistently extractable and reflective of system behaviour. This reliability ultimately justified its selection as the primary metric for sensitivity analyses and stability assessments.

The following table summarizes the dataset, emphasizing the trends, discrepancies, and limitations of using natural frequency and damping ratio as stability metrics for the parafoil system.

Table C.1: Stability Metric Dataset: Natural Frequency, Damping Ratio, and Maximum Amplitude for Various Parameter Scales

Parameter	**Natural Frequency** (ω_n)	**Damping Ratio** (ζ)	**Max Amplitude** (α)
m_{payload} (Scale 0.80)	0.011	0.039	37.087
m_{payload} (Scale 0.90)	0.011	0.042	37.783
m_{payload} (Scale 1.00)	0.010	0.045	38.397
m_{payload} (Scale 1.10)	NA	NA	NA
m_{payload} (Scale 1.20)	0.007	0.049	39.445
c (Scale 0.80)	0.007	0.042	37.712
c (Scale 0.90)	0.010	0.044	38.046
c (Scale 1.00)	0.010	0.045	38.397
c (Scale 1.10)	0.010	0.046	38.769
c (Scale 1.20)	0.010	0.048	39.161
$C_{L,\alpha}$ (Scale 0.80)	0.008	0.041	36.403
$C_{L,\alpha}$ (Scale 0.90)	0.009	0.043	40.511
$C_{L,\alpha}$ (Scale 1.00)	0.010	0.045	38.397
$C_{L,\alpha}$ (Scale 1.10)	0.011	0.047	36.605
$C_{L,\alpha}$ (Scale 1.20)	0.010	0.047	36.031
C_{D0} (Scale 0.80)	0.008	0.059	36.078
C_{D0} (Scale 0.90)	0.009	0.051	37.278
C_{D0} (Scale 1.00)	0.010	0.045	38.397
C_{D0} (Scale 1.10)	0.011	0.043	39.446
C_{D0} (Scale 1.20)	0.011	0.037	40.433
ρ (Scale 0.80)	0.008	0.050	39.090
ρ (Scale 0.90)	0.010	0.048	39.906
ρ (Scale 1.00)	0.010	0.045	38.397
ρ (Scale 1.10)	NA	NA	NA
ρ (Scale 1.20)	0.010	0.040	37.836

D

More Wind Tests

This appendix provides additional wind test results conducted to evaluate the parafoil system's response to isolated steady-state and gust wind conditions. These tests, while supplementary to the primary analysis in Chapter 7.3, do not represent extreme-case scenarios but offer insights into the system's behaviour under specific wind influences. The results include longitudinal and lateral wind effects applied separately, with steady-state and gust components, highlighting the sensitivity of the parafoil system to varying wind profiles.

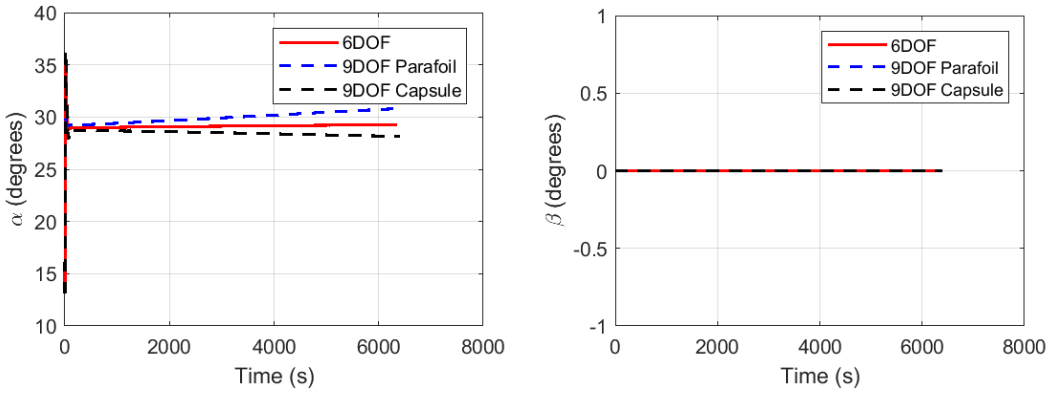

Figure D.1: Behaviour of the parafoil system under 0 deg longitudinal winds with steady-state component (alpha plane on the left, beta plane on the right).

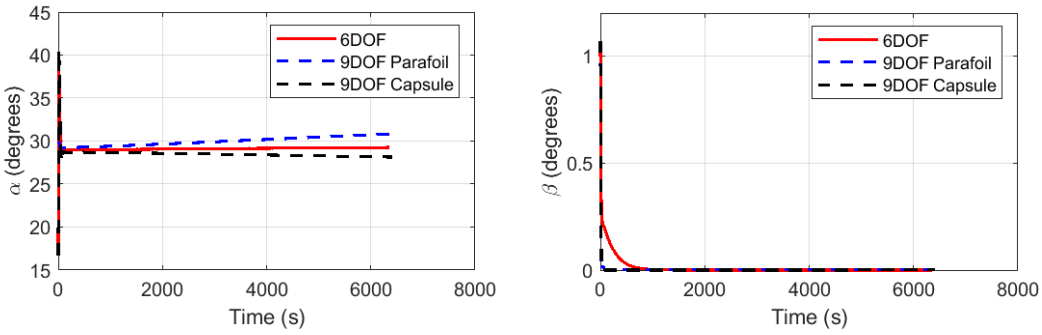

Figure D.2: Behaviour of the parafoil system under 90 deg lateral winds with steady-state component (alpha plane on the left, beta plane on the right).

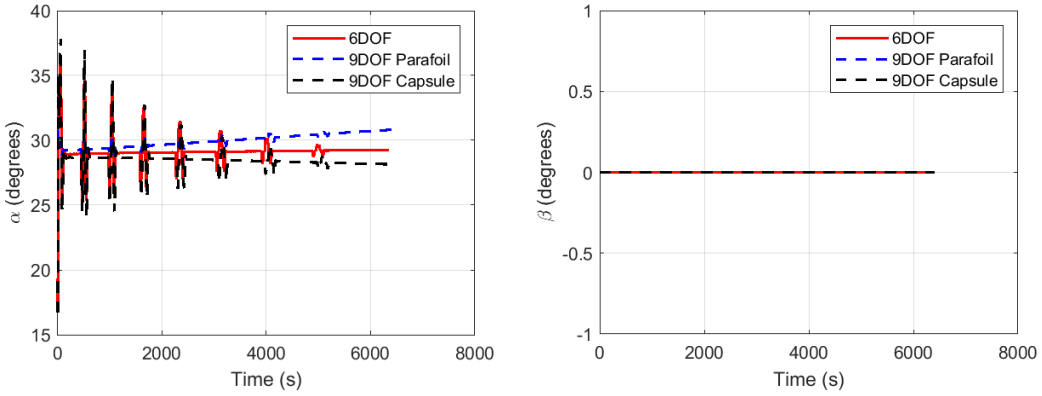

Figure D.3: Behaviour of the parafoil system under 0 deg longitudinal winds with gust component (alpha plane on the left, beta plane on the right).

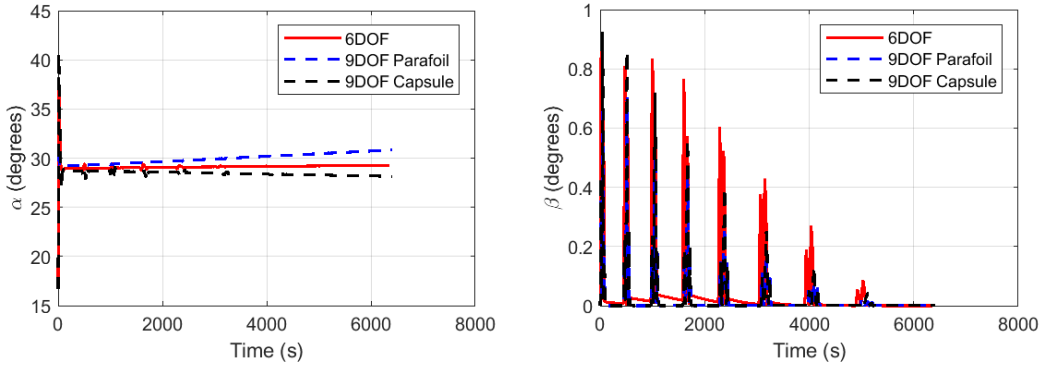

Figure D.4: Behaviour of the parafoil system under 90 deg lateral winds with gust component (alpha plane on the left, beta plane on the right).